STRUCTURE AND TUNABLE PROPERTIES OF HYBRID ZEOLITIC IMIDAZOLATE FRAMEWORKS

A Dissertation
Presented to
The Academic Faculty

by

Krishna Chandran Jayachandrababu

In Partial Fulfillment
of the Requirements for the Degree
Doctor of Philosophy in Chemical Engineering in the
School of Chemical & Biomolecular Engineering

Georgia Institute of Technology
May 2017

STRUCTURE AND TUNABLE PROPERTIES OF HYBRID ZEOLITIC IMIDAZOLATE FRAMEWORKS

Approved by:

Dr. Sankar Nair, Advisor
School of Chemical & Biomolecular Engineering
Georgia Institute of Technology

Dr. David S. Sholl, Co-Advisor
School of Chemical & Biomolecular Engineering
Georgia Institute of Technology

Dr. Krista S. Walton
School of Chemical & Biomolecular Engineering
Georgia Institute of Technology

Dr. Ryan P. Lively
School of Chemical & Biomolecular Engineering
Georgia Institute of Technology

Dr. Johannes Leisen
School of Chemistry & Biochemistry
Georgia Institute of Technology

Date Approved: March 15th 2017

Any sufficiently advanced technology is indistinguishable from magic.

- Arthur C. Clarke

Dedicated to my grandfather, Late Adv. T.R. Raman Pillai, for believing in me more than I did. I miss you every single day.

ACKNOWLEDGEMENTS

When I first came to Georgia Tech to pursue my doctoral degree, I was full of optimism and confidence. In January of 2013, I received an email from Dr. Sankar Nair and Dr. David Sholl asking me to join them in a meeting to discuss an open research position. It must have been a fairly routine candidate interview for them, but to me it was an assist from the Universe. Dr. Nair and Dr. Sholl guided me patiently and at every turn made it possible for me to become a better person and scholar. I would like to express my sincerest gratitude to both of them for giving me the opportunity to achieve my dream of getting a Ph.D.

I owe a large part of my success as a researcher to Dr. Johannes "Hanno" Leisen. Hanno and I met soon after I embarked on this project and without his help, I would never have learned all that I know about advanced NMR spectroscopy. Having no prior experience, it was 'learning by immersion' and Hanno was my lifeguard. His knowledge and patience help me to navigate through challenging problems that I describe in this thesis. I will remember Hanno fondly for the rest of my life for his guidance (and also because we share a birthday!)

I would also like to thank my doctoral committee members Dr. Krista Walton and Dr. Ryan Lively for their helpful comments and suggestions that helped me complete this work. I consider myself truly fortunate to have both of them along with my advisors and Hanno on my committee to guide my research. I thank Dr. Ryan Nieuwendaal at NIST for hosting me for two weeks and letting me learn more about the fine points of NMR spectroscopy through our regular conversations. I also wish to thank Dr. Dennis Hess for

imparting his wisdom on leadership and professional ethics, both within his classroom as well as during our friendly water-cooler conversations.

In 2009, I decided to forgo an opportunity to take up a job in the IT sector, and proceeded to pursue my advanced degree in chemical engineering at the University of Southern California. I was able to gain valuable research experience working in Dr. Sri Narayan's lab which led to a successful Ph.D. admit at Georgia Tech. For that, I am truly thankful to the USC Trojan family (and to the city of Los Angeles for being a home-away-from-home).

Going further back, the direction of my life is due in no small measure to my teacher and mentor, Mr. K.E.G. Varghese at Girideepam school. His words helped me to find my passion and the confidence to follow my dreams. His words of encouragement helped me to get to the place where I am today. I am forever grateful for his blessings.

I want to thank all my friends for making my life more colorful. There are too many to name here, but you know who you are – my buddies at Girideepam, BITS-Pilani, USC and GT. All said and done, it's those road trips, skype calls, coffee breaks, late night food runs, and movie nights that I will cherish the most. Thank you for being there for me, always.

My grandparents have been my biggest source of inspiration. Whenever I face an adversity, I found an answer by thinking back to how they confronted worse odds and came out on top time and time again. My grandfather was the greatest man I ever knew, and I couldn't have asked for a better role model. My grandmother is the strongest and most

honorable woman I have ever met and I hope when I am faced with difficulties in my life, I have her courage and wisdom to take them on.

I could write a whole another thesis on the sacrifices that my family had to make to get me to where I am. Each day I am reminded of how the unconditional love and support they continue to give me has made my life so fulfilling. My father has always been the person I look up to, and he taught me the value of learning over earning. He is the security blanket that enabled me to continue my studies without any worries. And then there is my mother. She is the force that holds my universe together. She is the most caring and loving person I have ever seen. I hope I have made both of you proud with everything that I continue to do. I couldn't have asked for better parents and I love you both very, very much.

TABLE OF CONTENTS

LIST OF TABLES

LIST OF FIGURES

SUMMARY

Metal Organic Frameworks (MOFs) are a class of nanoporous materials that have shown tremendous promise for applications in chemical separations. In recent years, thousands of structures of MOFs have been synthesized and studied for facilitating several different separation processes that are vital to the chemical engineering industry. Specifically, these materials can be used in relatively energy efficient separations such as adsorption, membrane separation, and pervaporation to replace conventional thermally-based techniques like distillation. However, much work remains to be done in understanding and exploiting their structure-property relationships.

In this thesis, we examine unique structural and functional aspects of MOFs versus other nanoporous materials. The pore size and available adsorption sites in MOFs can be tuned via the incorporation of two or more organic linkers in the MOF framework, resulting in a 'mixed-linker' material. In previous generations of nanoporous materials such as zeolites, this fine-tuning of properties was achieved by cation exchange and compositional variations. Currently, very little is known about the structure-property relationships of mixed-linker MOFs due to the novelty of MOFs as a class of materials as well as the large number of possible combinations of linkers. We have chosen an important family of MOFs known as Zeolitic Imidazolate Frameworks (ZIFs) to highlight different facets of mixed-linker synthesis. Importantly, this work develops different methodologies to study the structure of mixed-linker materials at multiple length-scales, which allows a reliable connection to their molecular adsorption and transport properties.

In Chapter 2, the tunability of properties such as adsorption and diffusion of guest molecules in mixed-linker ZIFs is demonstrated. ZIF-8 and ZIF-90 are chosen as the parent structures, based on which a series of ZIF-8-90 mixed-linker materials are synthesized. These materials have pore sizes ranging between 4-5 Å, which make them interesting from the perspective of separating small molecules such as water and C1-C4 alcohols that have kinetic diameters comparable to the pore sizes. Adsorption of water and alcohols is used to show that such materials exhibit continuously tunable hydrophobicity and organophilicity by varying the relative composition of the two linkers. Diffusion measurements show that diffusivities and ideal diffusion selectivities can be tuned over several orders of magnitude by engineering the pore composition of these materials. Preliminary evidence for structural distribution/mixing of linkers in these materials is also provided in this chapter.

With a view to establish evidence for microscopic (unit cell level) distribution or mixing of the linkers in the crystal structure of ZIF-8-90 materials, Chapter 3 deals with the microscopic structure elucidation of mixed-linker ZIF8-90 materials. For this purpose, a two dimensional NMR approach was taken. ^{1}H CRAMPS spectroscopy was used to correlate the inter-nuclear distances of different linkers to their spatial distribution. This method has the advantage that it does not require isotopic labeling of nuclei. By experimentally measuring the rate of nuclear spin transfer between nuclei and comparing it to computationally generated models, 'best-fit' structures for several compositions of ZIF-8-90 hybrids were provided. The model also provides a probability distribution of possible pore aperture configurations that can be used to accurately model mixed-linker structures for adsorption/diffusion studies.

In Chapter 4, we study in detail the synthesis routes that are used to produce mixed-linker/hybrid ZIF materials. Synthesis routes can affect the structure and hence properties of mixed-linker MOFs. Two different synthesis approaches (*de novo* synthesis and solvent assisted linker exchange (SALE),) are compared from a structural and mechanistic perspective. Macroscopic differences in performance resulting from the microscopic inhomogeneity in linker distribution is elucidated. Native fluorescence confocal microscopy is used to image the core-shell type structure of SALE hybrids. The reaction mechanism of ZIF-8 to ZIF-90 SALE is studied using different particle sizes, reaction temperatures and durations. This is the first comprehensive study of SALE and *de novo* routes as alternate synthesis routes that result in materials with same compositions but drastically different microstructures and properties.

An application of SALE-based techniques is presented next. In particular, Chapter 5 explores the reversal of acid-gas induced damage in ZIF materials. Specifically, a solution-based treatment called Solvent Assisted Crystal Redemption (SACRED) is proposed that can reverse the damage caused by humid SO_2 gas in ZIF-8 and ZIF-14. The results from this method challenges the existing understanding of the stability of ZIF materials. FTIR spectroscopy, X-ray diffraction, and adsorption experiments are used to show that the post-recovery ZIF-8 is chemically and functionally identical to the pristine material. ^2H solution NMR spectroscopy is used to provide mechanistic insights into the recovery mechanism. This method is a potential way to extend the useful lifetime of materials in processes involving ZIF-based adsorbents or membranes.

CHAPTER 1. INTRODUCTION

1.1 Energy Efficient Separations

Energy-intensive separation processes have dominated the chemical processing landscape since its inception. The recent necessity for energy-efficient separation processes has been driven not only by economic factors, but also by environmental concerns. High energy processes leave larger carbon footprints on the environment and also lead to harmful effluents being released into the biosphere. In the last few decades, dedicated research efforts have been undertaken to mitigate these effects.

In the United States alone, approximately 30% of all energy consumed in the year 2016 was attributed to the industrial sector.[1] Within this fraction, the largest contribution comes from chemical separations. It has been estimated that chemical separations account for around 10-15% of the total energy consumed within the country.[2] Technological advances that can reduce the energy requirement for separations can therefore potentially save billions of dollars. Thermally-based separations currently dominate energy use due to high energy requirements to raise the temperature (e.g. distillation, evaporation) or lower the temperature (e.g. cryogenic distillation). Several alternative processes that do not involve thermally-based systems have been identified as potential replacements for current technologies.[3] Researchers have also identified several key processes that require increased attention due to their value and overall benefits.[2, 4] In this thesis, the research focus is on a novel family of materials that can potentially benefit molecular separation based on a few of these energy-efficient routes.

Figure 1.1 shows the relative energy requirements for performing different types of chemical separations. As compared to thermally driven processes like distillation, membrane-based or adsorptive processes can have significantly lower energy usage. However, these technologies have not matured enough to replace processes like distillation, which still contributes to almost half of the entire energy needs in this sector.[2] Typically, adsorption-based processes utilizes a material that has a higher affinity for one of the components in the feed stream. After the concentration of this component is saturated in the adsorbed phase, it is desorbed and recovered. In membrane-based processes, the components are separated based on their size which affects their transport properties (e.g. diffusivity, flux) through the membrane. Pervaporation, a membrane-based technology in which the permeate side is maintained as a low-pressure vapor phase, is also a relatively modern technique with moderate energy requirements that has great potential to supplement conventional techniques. These processes can be used to separate mixtures with large number of components (e.g. bio-based feedstock) in which each individual component has high value but is low in volume. The main challenges associated with these processes are to design materials that can improve the stability, selectivity, and yield of the process while remaining economically feasible.

There is a plethora of industrial processes (e.g. biorefineries, fracking, specialty chemical production) where these separation techniques can be used to reduce the energy requirements. But currently there is no 'one-size-fits-all' material that can do all the different separations that are encountered within these industries. Even established porous materials like zeolites may not be sufficient for this purpose because the size difference between some components in the feedstock is minuscule and sharp separation cannot be

attained. These concerns have led to the investigations of new types of materials that can offer better control over pore sizes and transport properties.

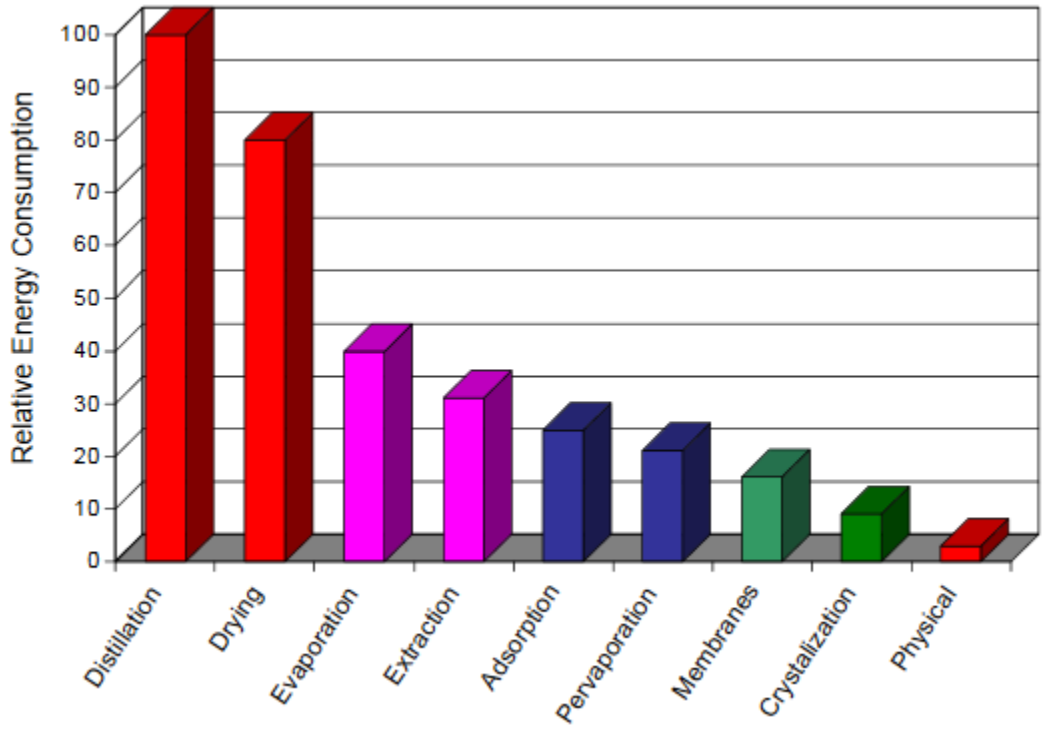

Figure 1.1 Relative energy consumption for various separation processes, averaged from multiple examples. Figure reproduced from 'Oak Ridge National Laboratory Report – Materials Research for Separations Technologies: Energy and Emission Reduction Opportunities'[3]

1.2 Metal Organic Frameworks

Porous materials with high surface area have been generating research interest for applications in adsorption and membrane based processes due to their high storage capacity and molecular sieving properties. Naturally occurring porous materials like carbon and zeolites have been used in such processes for the better part of last century. Recently, a new class of materials known as metal organic frameworks (MOFs) have been developed that can be added to this list. MOFs consist of metal atoms or clusters that are linked to

each other via organic linker molecules. Due to the large variety of building blocks available, thousands of MOFs have been synthesized.[5-6] Based on the chemistry of the linker molecules and the metal constituents, each MOF has unique adsorption affinities and pore sizes. The building blocks and lattice structures of several MOF species are shown in Figure 1.2. The internal surface area of some of these synthesized MOFs are as high as 7000 m^2/g and the theoretical limit may be twice as high.[7] MOFs have been studied as membranes supported on porous substrates, membranes embedded in polymer matrices, adsorbates packed into columns or in powder form to evaluate their performance in a variety of separations.[8-11]

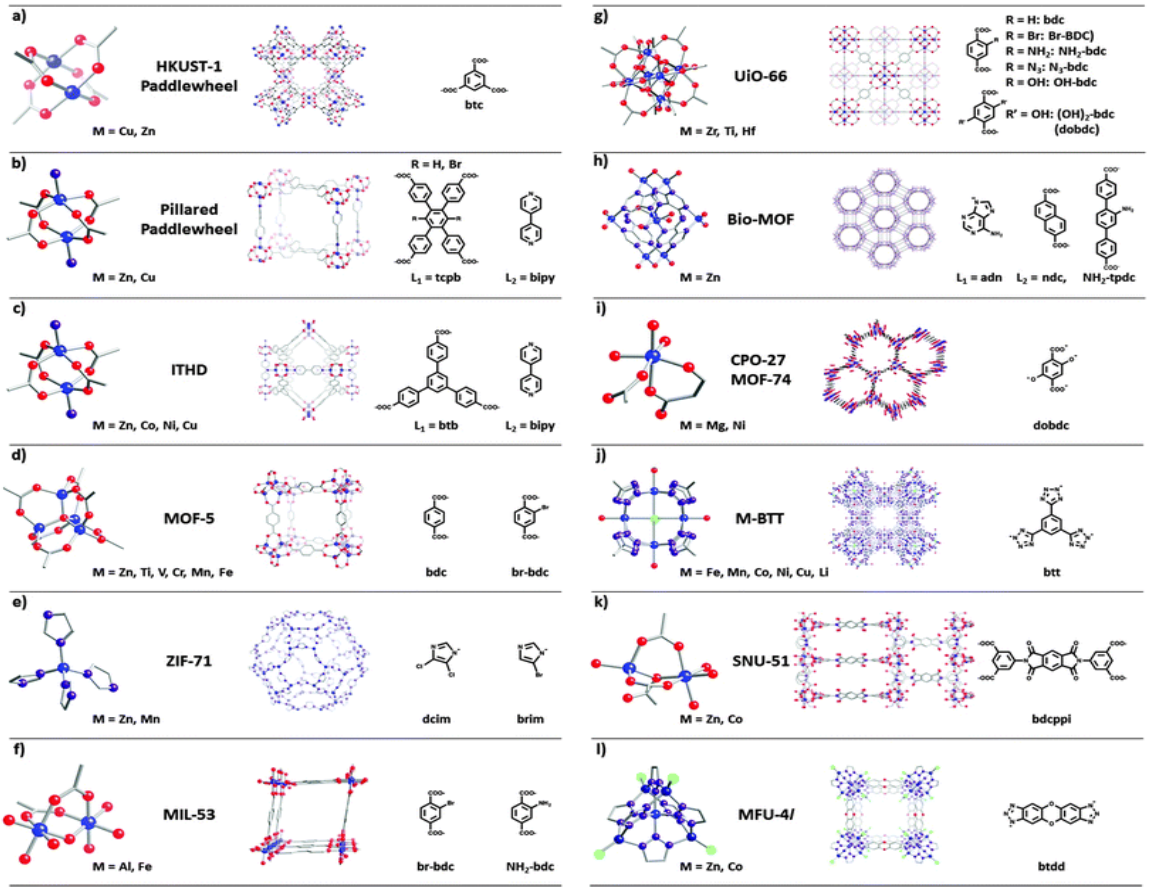

Figure 1.2. Building blocks and lattice structures of selected MOFs. Figure reproduced from Farha et al.[12]

1.3 MOFs for separations – Challenges and Opportunities

Despite the large number of MOF structures that have been reported, industrial processes that implement MOF-based technologies have been very limited. Even though MOFs often have more facile synthesis routes as compared to other porous materials like zeolites, this does not translate to commercial success. Certain factors that contribute to the lukewarm reception towards MOFs in the industry have included their stability issues, difficulty in scale-up synthesis, cost of raw materials, usage of hazardous solvents for synthesis etc. Other factors like difficulty in making membranes out of MOFs have also slowed down their progress.

The large variety of building blocks available for synthesizing MOFs have also contributed in part to some of these issues. The chemical diversity of these entities make it difficult to design a straightforward route that can be used to make membranes. For example, some MOFs are amenable to secondary growth or seeding methods where they are grown on top of membrane supports. Certain other MOFs may be more conducive to a direct growth method because of their poor adhesion to the support material. In cases where direct growth is not possible, post-synthetic modification may be required to obtain the final membrane.[13] Polymers are often used alongside MOFs to make mixed-matrix membranes (MMMs) that combine the relative ease of making polymer membranes with the superior separation properties of MOFs.[14]

The bridging linker molecule in some MOFs can be prohibitively expensive, which prevents large scale manufacture of those MOFs or their incorporation into membranes. In those cases, it is necessary to optimize the MOF loading on the membranes and maximize

the available surface area. MOF membranes can be formed within hollow fibers made of organic (polymer) or inorganic (ceramic) materials.[15-16] This reduces the necessity for synthesizing large quantities of MOFs with expensive building blocks.

Not all MOF structures predicted theoretically can be synthesized actually. Sometimes syntheses are inhibited by thermodynamic or kinetic factors; sometimes they are not feasible due to the insolubility of the linkers in commonly used solvents. In those cases, alternate routes for synthesis are used – like post-synthetic functionalization, solvent assisted linker exchange or non-bridging linker incorporation.[12] Some of these modifications can result in unexpected side-effects like reduced surface area or porosity that must be countered to maintain good separation properties.

Before MOFs can be used in large-scale separations, their synthesis methods and their structure-property relationships must be carefully studied to ensure that they can be successfully applied in industrial settings. In this thesis, we examine a particular family of MOFs known as zeolitic imidazolate frameworks that have shown good promise as materials for small molecule separations. These materials were selected because they offer a large family of similar structures that can be mixed and matched to generate materials with specific pore characteristics. Our findings can be directly applied to tackle many of the challenges mentioned above. We show that mixed-linker synthesis of ZIF-8 and ZIF-90 produce a family of materials with continuously tunable pore sizes and adsorption affinity towards molecules such as water and alcohols. These mixed-linker ZIF-8-90 materials combine the desirable properties of both parent structures into the same framework. We also demonstrated that by using different synthesis routes, chemically similar but structurally very different mixed-linker ZIFs can be made. These structural

differences directly contribute to differences in properties such as adsorption affinity in these materials. This work explains the necessity of exercising care when adopting alternative routes (e.g. linker exchange, seeded growth) for synthesizing MOFs as they can produce vastly different materials. We developed an NMR-based technique that can be used to distinguish the microstructure of these materials made via different synthesis routes. This method uses established NMR techniques and computational modeling to parametrize linker mixing and can be extended to other mixed-linker MOFs. This method benefits computational modeling of mixed-linker materials for accurately predicting adsorption and diffusion properties. Finally, we addressed the stability issues of ZIFs in acidic environments by developing a solution-based technique to recover the porosity and crystallinity of ZIF crystals degraded by acid gases. This extends the lifetime of ZIF materials used in industrial processes and reduce the wastage of ZIFs made from expensive precursors. This method has the potential to reduce the cost of materials in processes involving ZIFs.

1.4 Zeolitic Imidazolate Frameworks

Among materials classified under MOFs, zeolitic imidazolate frameworks (ZIFs) have shown promise as candidates for adsorption and membrane based separations. These imidazole-based MOFs have high stability and permanent porosity that make them potential alternatives to replace existing candidates.[17-18] They also exhibit structural flexibility caused by linker rotation that make them more suited for property tuning as compared to rigid MOFs. By changing the functional groups on the imidazole ring, different ZIF structures can be realized.[19] These materials exist in various zeolite

topologies. A typical ZIF lattice in sodalite (SOD) topology with Zn nodes and 2-methylimidazole as linker is illustrated in Figure 1.3.

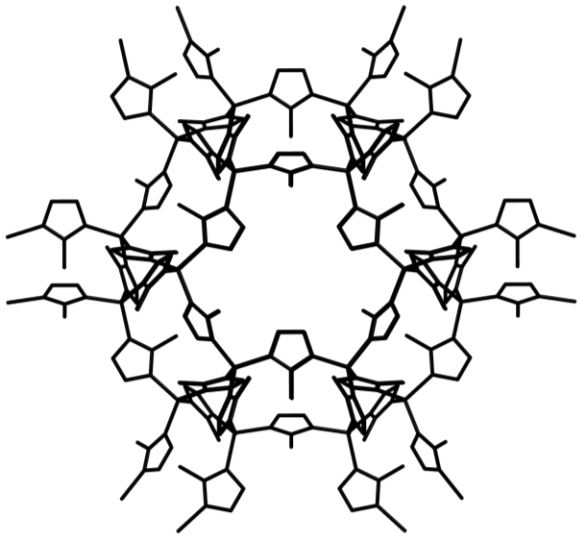

Figure 1.3. Lattice structure of ZIF-8 (Zn atoms connected to 2-methylimidazole linkers in a SOD topology).

Several studies have been reported where exceptional performance of ZIF materials in separations are demonstrated. ZIF-8 based membranes have been used in gas separations like ethylene/ethane, hydrogen/propane, propylene/propane, krypton/xenon etc.[20-26] It has also been utilized in separations involving liquids like water and alcohols.[27-28] Other ZIF materials like ZIF-7, ZIF-71, ZIF-90 etc. have also been used in membrane-based separations with good results.[9, 15, 29-30] Recently, our group reported ZIF-8 based hollow fiber polymer membranes that were prepared via interfacial microfluidic processing.[16, 31] These membranes show exceptional performance in light gas separations. This method for membrane synthesis also reduces material cost while maximizing accessible membrane surface area.

In addition to membrane-based processes, ZIFs have also been studied for use in adsorption-based separations. Based on the linker functional group, ZIFs can be highly hydrophobic (e.g. ZIF-8, ZIF-71) or hydrophilic (e.g. ZIF-90, ZIF-68). They also show affinity towards small molecules like alcohols. Framework flexibility of ZIFs also makes it possible for them to adsorb or transport molecules that are significantly larger than their nominal pore-sizes.[32-34] Alcohol and water adsorption in ZIFs have been studied by multiple research groups.[11, 35-37]

Despite the large number of available linker selections, not all ZIFs have been well-studied from a separations standpoint. ZIF-8 is the most widely studied ZIF, especially as a material for making membranes. There is a dramatic drop-off to the next tier of popular ZIFs that include ZIF-7, ZIF-90, and ZIF-71. Therefore, there is a huge reservoir of untapped potential that this family of materials offer. Mixing linkers within the same framework (as detailed below) opens up a new hierarchy of structures that dramatically expand on this potential. However, not enough information is available on the structural characterization and property tuning of these materials. We demonstrate how pore characteristics can be continuously fine-tuned using composition control and how structural details can be obtained from macroscopic and microscopic experiments.

1.5 Mixed-Linker ZIFs

One of the main advantages that MOFs present when compared to other porous materials like zeolites is the ability to synthesize them with multiple linkers within the crystal matrix. By doing mixed-linker synthesis with controlled linker ratios, it is possible to fine-tune their properties like pore-size and adsorption affinity. Mixed-linker MOFs are

also referred to as multi-variate (MTV) MOFs.[38-39] Mixed-linker MOF synthesis can be done via 'one-pot synthesis' routes where both linkers and the metal source are present from the beginning, or post-synthetic modification route where an additional linker or functionality is added into the framework of an already existing MOF lattice.[40-41] Mixed-linker zeolitic imidazolate frameworks such as ZIF-8-90, ZIF-7-8, ZIF-8-ambz, and ZIF-7-90 have been reported in literature.[40, 42-44] Due to the range of linker ratios possible and different configurations of linker distribution in space, an infinite number of possible structures exist for each of these mixed-linker ZIFs. One such possible structure for a mixed-linker ZIF-8-90 material with equal ratio of 2-methylimidazole and imidazole-2-carboxaldehyde is shown in Figure 1.4. Previous work in our group has shown that these materials have continuously tunable pore-sizes.[40] However, there is no information available on how this translates to an actual separation process. There is also limited knowledge on how the microstructure of these materials are different from a physical mixture of the parent structures. These challenges are tackled within this thesis and the methodologies adopted for accomplishing these goals are explained below.

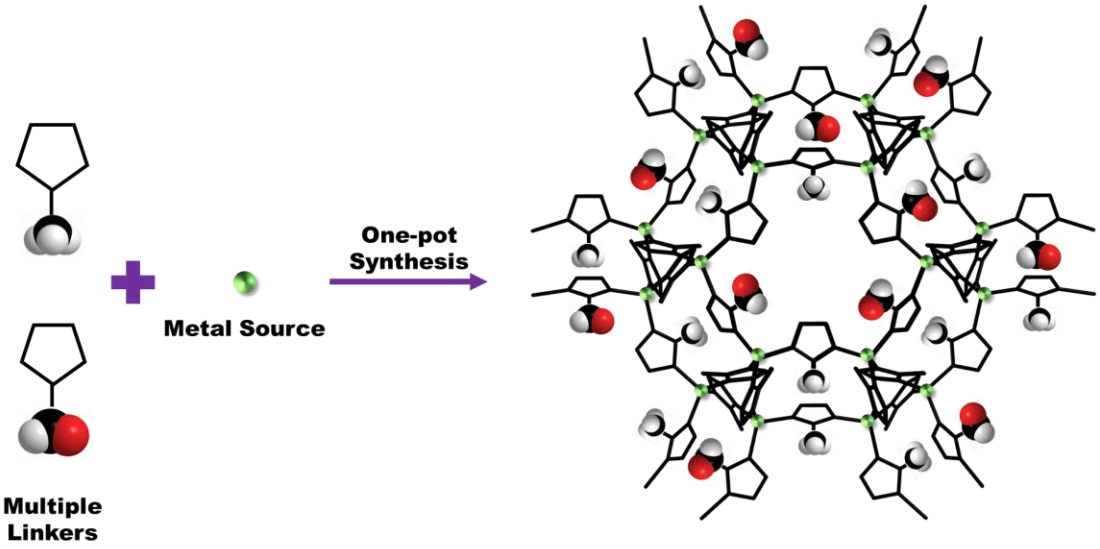

Figure 1.4. Mixed-linker ZIF-8-90 lattice with equal linker ratio. Green spheres are Zn atoms, red spheres are oxygen atoms, white spheres are hydrogen atoms and black spheres are carbon atoms. Atoms not belonging to functional groups are not highlighted for clarity.

1.6 Adsorption and Diffusion Characterization

Characterization of adsorption and diffusion in zeolitic imidazolate frameworks can be performed using established techniques. Adsorption isotherms of guest molecules in ZIFs are measured using gravimetric techniques where the change in mass of the adsorbent is monitored as a function of the partial pressure of the adsorbate. Kinetic uptake data from these curves can also be used to calculate transport diffusivity of these adsorbates.[45] These transport diffusivities can be converted to Maxwell-Stefan (M-S) diffusivities using thermodynamic correction factors obtained from the isotherms.[46]

NMR-based techniques have been used to measure self-diffusivities of guest molecules in polymers and porous materials.[47-49] These measurements are done by monitoring the NMR signal attenuation caused by the diffusion of NMR active nuclei like ^{1}H, ^{13}C, ^{15}N, ^{129}Xe etc. that are subjected to a spatial magnetic field gradient.[50-53] These

measurements are made at equilibrium conditions and can vary significantly from the transport diffusivity measurements made using gravimetric uptake curves that are made at non-equilibrium conditions. But the use of thermodynamic correction factors make it possible to compare self-diffusivities and M-S diffusivities for the same adsorbent-adsorbate pairs. An example of such a measurement made in ZIF-8 crystals is shown in Figure 1.5.

We used these techniques to measure adsorption isotherms and diffusion coefficients of several guest molecules in mixed-linker ZIF materials to demonstrate how their properties like pore-size and adsorption affinity can be fine-tuned by controlling the constituent linker compositions. These experiments also provide preliminary evidence of how the microscopic structure of mixed-linker ZIFs differ from a physical mixture of the parent materials.

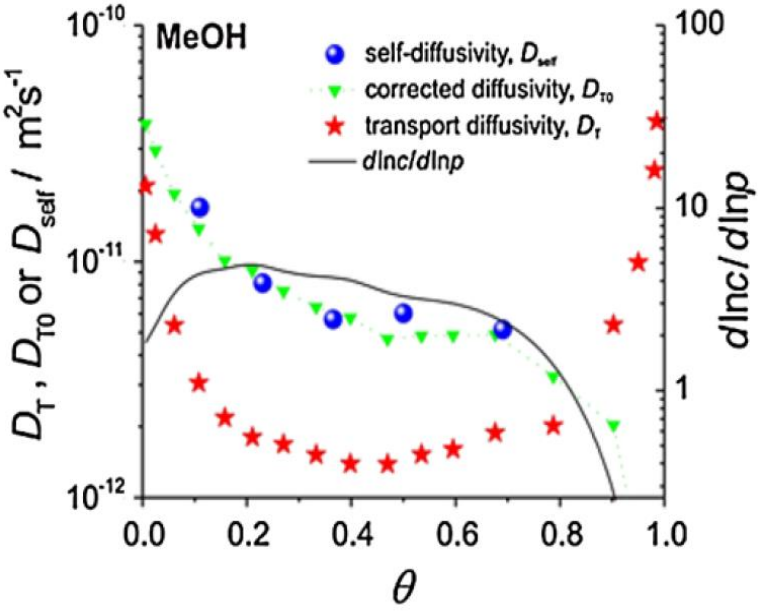

Figure 1.5. Comparison of methanol self-, transport, and corrected M-S diffusivities in ZIF-8 at 298 K. Figure reproduced from Karger et al.[54]

1.7 Structure of Mixed-Linker ZIFs

The microstructure of mixed-linker MOFs is governed not only by the synthesis conditions and linker ratios, but also the relative size of the linkers, solubility in synthesis media, coordination modulating agents, topology of parent MOFs and several other factors. Therefore it is difficult to predict *a priori* the structure of a given mixed-linker system. Based on the final product, different characterization techniques are employed to elucidate their structures. In some cases like IRMOF/MOF-5 hybrids, the individual linker domains can be differentiated using optical microscopy due to their difference in color.[55] But in the case of ZIF-8-90 hybrids, even X-ray crystallography cannot distinguish hybrids of different linker ratios due to the similar electronic structure of constituting linkers.

NMR-based crystallography has become prominent in the last decade due to its ability to distinguish different nuclear environments at very small length-scales. These methods utilize the dipolar coupling between nuclei that are separated by small distances and measure the rate of nuclear spin transfer to ascertain these distances. These methods were used in measuring the domain sizes of polymer blends or photovoltaic hetero-junctions.[56-59] Recently, these methods have been implemented to ascertain the crystallinity of organic compounds in powder form.[60-61]

Linker distribution in mixed-linker MOFs have been studied by different research groups using NMR techniques in recent years.[62-64] Some of these techniques like REDOR requires isotopic enrichment of linkers for obtaining good signal-to-noise ratios. But other techniques like CRAMPS can be successfully employed in samples with naturally abundant nuclei like ^{1}H. Experimental NMR data is correlated to actual structures using

computational modeling. In Figure 1.6, the experimentally obtained spin diffusion curves of a mixed-linker DUT-5 MOF and corresponding curves generated using computationally generated structures are shown as an example.[63] However, in this case, only highly anisotropic structures could be distinguished. We present a spin-transfer based method that can probe the anisotropy in linker mixing at a unit cell level. We also provide a method to quantify the short range order of mixed-linker MOFs which is useful for accurately generating these structures for predicting adsorption and diffusion behavior. Using this method, we also demonstrated the microscopic difference in the structure of mixed-linker ZIFs with identical linker ratios that were made using different synthesis routes.

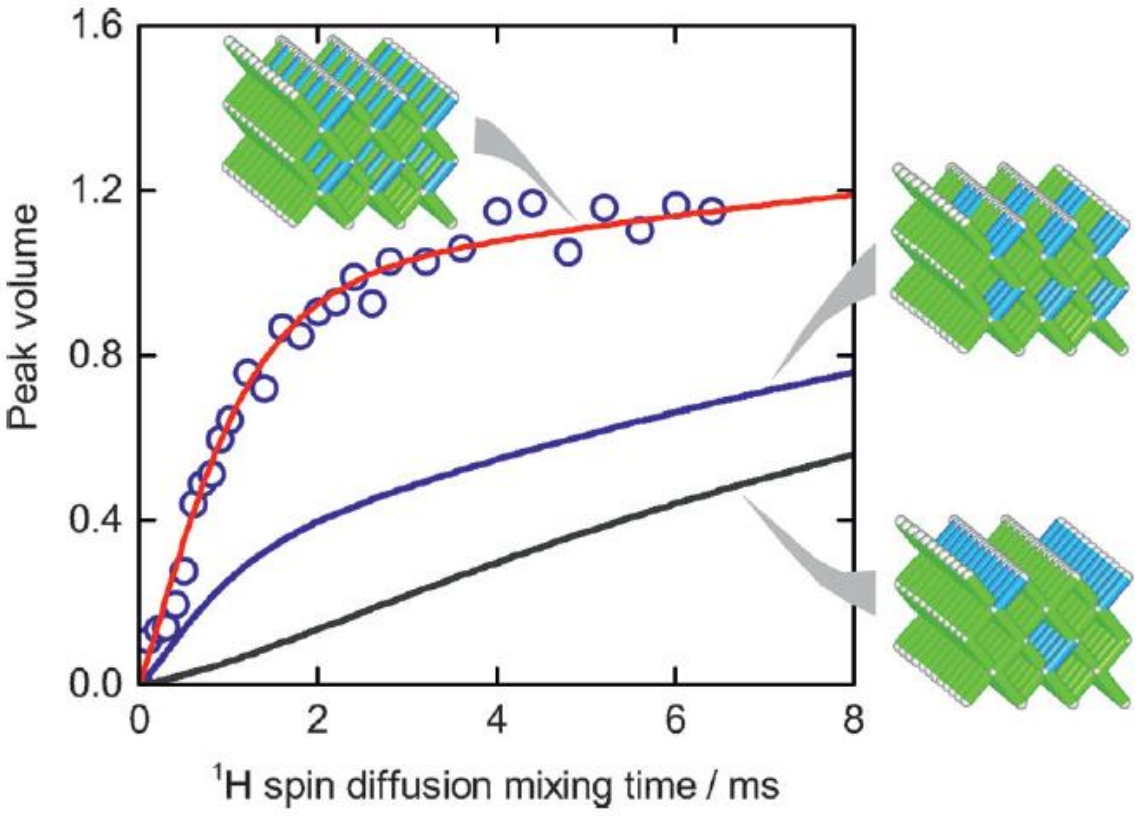

Figure 1.6. Measured and calculated ^{1}H spin diffusion curves of mixed-linker DUT-5 MOFs. The structures shown were used to computationally generate spin diffusion curves. The best-fit curve is highlighted in red. Figure reproduced from Mali et al.[63]

1.8 Solvent Assisted Linker Exchange (SALE)

SALE has been proposed as a method for attaining otherwise difficult-to-obtain structures.[65-70] This method uses a fully synthesized MOF crystal as starting material and replaces the existing linkers with new ones to obtain a new material. The mechanism of SALE depends on the starting MOF, the desired linker, solvent, and reaction conditions. SALE can be used to partially or completely replace linkers in a MOF. Here we explore the partial replacement of ZIF-8 linkers using ZIF-90 to obtain mixed-linker ZIF-8-90 materials. Until now, no direct comparison of a family of MOFs made via *de novo* routes and SALE have been studied anywhere. We showed that not only are the two structurally different, but their properties also vary significantly. Our studies also revealed an unexpected application for SALE-based techniques in 'healing' a ZIF crystal after it had undergone degradation due to acid-gas attack.

1.9 Recovery of ZIF crystallinity and porosity after degradation

MOFs are susceptible to degradation under conditions that are usually encountered in industrial processes. Based on the chemistry of the metal site and the linker molecule, they might be degraded by chemicals (e.g. water, acids) or high temperature.[71-73] ZIFs in particular are vulnerable to acid attack. Acid protons break the Zn→N coordination bond by protonating imidazole linkers that are weak bases. This causes loss of crystallinity, surface area, and pore volume of the material and affects the performance in a separation process. There have been many investigations probing the degradation mechanism of ZIFs and as the damage is a chemical change and not a physical change, it has been classified as irreversible. But if the damage to ZIFs cannot be mitigated or reversed, then their usage in

industrial processes will not be feasible. Conventional methods for improving MOF stability include linker functionalization or structural modifications.[74-75] But these methods may not be viable always as additional group and entities within the framework can contribute to undesirable side-effects including reduced pore volume, surface area or adsorption affinity. The ideal solution to such a problem would involve a simple treatment that will reverse the damage and does not involve expensive chemicals or equipment. We developed a SALE-based technique which is capable of recovering the porosity and crystallinity of ZIF materials that have undergone significant degradation from acid-gas attack.

1.10 Impact of this thesis

The topics discussed in this thesis significantly advance the understanding of mixed-linker ZIF materials in all the aspects mentioned in the previous sections. Key findings and advances presented in this thesis are highlighted below.

(1) We demonstrate that mixed-linker synthesis of ZIFs can be used to achieve good control over the pore size and adsorption affinity of these materials. In particular, this strategy for continuous tuning opens up the opportunity to perform separations that may not have been possible with traditional materials that have discrete pore sizes. We also showed that desirable properties of two ZIFs (e.g. hydrophobicity of ZIF-8 and larger pore size of ZIF-90) can be incorporated into a single material using this method. This approach can be used in both membrane-based and adsorption-based separation processes.

(2) We provide a novel NMR-based method for the structural characterization of mixed-linker ZIFs. This technique uses already established NMR pulse sequences and does not

require isotopic labeling. It uses a kinetic rate based model and the Warren-Cowley parameter to fully describe the unit-cell-level structure of these materials. This technique can be generalized for other mixed-linker MOFs that contain different functional groups on different linkers. It makes it possible to generate more accurate structures for studying adsorption and diffusion through mixed-linker MOFs computationally. It can also be used to check for inhomogeneity or defects in an ordered MOF structure.

(3) We show that mixed-linker materials with identical bulk-composition but different synthesis route (*de novo* vs solvent assisted linker exchange) can have considerably different structures and properties. Using NMR spectroscopy, fluorescent confocal microscopy, water adsorption and nitrogen physisorption, we demonstrated that ZIF-8-90 SALE hybrids can have core-shell type structures that exhibit properties that are closer to a linear combination of their parent materials than that of a true mixed-linker material. SALE has been suggested by other researchers as a route to achieve otherwise difficult-to-synthesize structures. Our proposed methods offer a quick method to check for anomalies in these hybrid structures.

(4) We have developed a simple solution-based treatment for reversing the effects of an acid-gas attack on ZIF materials. These effects were previously thought to be irreversible in nature. We showed that even after prolonged exposure to acid gases and almost completely losing crystallinity and porosity, this method can restore ZIF-8 to near-pristine conditions. We also showed that a similar treatment can restore ZIF-14 with reasonable success. Due to the simplicity of this process, it has the potential to be implemented in membranes, packed columns, and powder form of ZIFs in batch or continuous treatments. This approach should also assuage the concerns about using MOFs in industrial processes

where they are subjected to harsh conditions and also mitigate the materials cost for replacing degraded MOFs in membranes/columns/beds.

CHAPTER 2. MIXED-LINKER ZEOLITIC IMIDAZOLATE FRAMEWORKS (ZIFS) FOR SMALL MOLECULE SEPARATION

2.1 Introduction[1]

Metal Organic Frameworks can be used for separations by exploiting differences in molecular adsorption strength, diffusivity, or both.[76] The vast range of MOF structures and the relative simplicity of their synthesis (in relation to other nanoporous materials like zeolites) create the possibility of rational design, synthesis, and modification of MOF structures[77-78] for specific adsorptive[79-81] or diffusion-based[24-25, 82-83] separations. A subclass of MOFs, known as zeolitic imidazolate frameworks (ZIFs), form structural topologies equivalent to those found in zeolites and other inorganic nanoporous oxide materials. More than 100 ZIF structures have been synthesized, including crystal topologies not realized in zeolites.[17, 19, 84-86] Several ZIFs are known to have good thermal and chemical stability, high microporosity, and high internal surface area.[87] ZIFs have created substantial interest for potential use in diffusive and adsorptive separations. For example, ZIF-8 is useful for membrane-based separation of hydrogen from hydrocarbons and propylene from propane to potentially replace or debottleneck energy-intensive cryogenic distillation processes.[16, 88-89]

[1] Work in this chapter has been published previously in K. Eum, K.C. Jayachandrababu, F. Rashidi, K. Zhang, J. Leisen, S. Graham, R.P. Lively, R.R. Chance, D.S. Sholl, C.W. Jones, S. Nair, "Highly Tunable Molecular Sieving and Adsorption Properties of Mixed-Linker Zeolitic Imidazolate Frameworks", Journal of the American Chemical Society, 137, p.4191-4197.

A considerable body of work has appeared on the quantification of molecular diffusion properties of ZIFs (most notably ZIF-8) and their use in membranes for diffusion-dominated separations.[32, 34, 90-91] It has been shown that molecules with significantly higher kinetic diameters than the nominal pore limiting diameter of ZIF-8 (3.4 Å) can diffuse through its micropores.[32] Molecular modeling and experimental measurements have shown that ZIF-8 has high diffusion selectivity for methanol over ethanol, whereas ZIF-90 has moderate selectivity for the same molecules.[35] Recent work has demonstrated the high hydrophobicity of ZIF-8 *via* adsorption studies of water and a number of liquid organic adsorbates.[34] ZIF-8 has also been identified as a candidate for adsorptive recovery of ethanol, propanol and butanol from water due to its hydrophobicity.[11, 92]

However, it is now clear that single-linker ZIF materials can only allow 'discrete' changes in pore size and adsorption characteristics by variation of the imidazolate linker. Diffusion-based molecular separations are extremely sensitive to small (< 0.1 Å) changes in the effective pore size. Only limited diffusive separations are possible with single-linker ZIFs, and *de novo* design and synthesis of ZIFs for each new separation target is difficult. Similarly, adsorptive separations are sensitive to small changes in the hydrophilicity or organophilicity of the ZIF which are difficult to design *de novo*. In previous work done in our group, a synthetic approach was developed for a series of mixed-linker ZIF-8-90 and ZIF-7-8 materials by inclusion of 2-carboxyimidazole (ZIF-90 linker) and benzimidazole (ZIF-7 linker) along with 2-methylimidazole (ZIF-8 linker) during synthesis.[87, 93] Preliminary characterization revealed these materials had a continuously tunable effective pore size (as measured by nitrogen physisorption) that is between the pore sizes of the single-linker 'parent' materials (ZIF-7, ZIF-8, and ZIF-90). Mixed-linker ZIF-8-90

materials were denoted as ZIF-8_x-90_{100-x} ($0 \leq x \leq 100$), where x is the percentage of ZIF-8 linkers in the framework. Here we demonstrate extensively that ZIF-8-90 materials have the remarkable property of continuously tunable diffusion and adsorption properties of small molecules like alcohols and water over several orders of magnitude. This result is facilitated by the controlled synthesis and characterization of a set of ZIF 8-90 mixed linker crystals spanning the entire range of 2-MeIM/OHC-IM linker ratios. The mixed-linker composition of the individual crystals was established using micro-Raman spectroscopy and water adsorption isotherms. Comprehensive diffusion and adsorption measurements using PFG-NMR and gravimetric techniques allow a detailed demonstration and evaluation of the tunable separation properties of mixed-linker ZIFs.

2.2 Experimental Methods

2.2.1 Materials

2-Methylimidazole (99%, 2-MeIM), $Zn(NO_3)_2 \cdot 6H_2O$ (99%) and sodium formate (99%, $NaCO_2H$) were obtained from Sigma-Aldrich. Carboxyaldehyde-2-imidazole (99%, OHC-IM), dimethylformamide (DMF), and methanol (MeOH) were obtained from Alfa Aesar. Deionized water (DI-H_2O) was produced with a Thermo Scientific 7128.

2.2.2 Synthesis of ZIF materials

Different synthesis procedures were used to produce ZIF crystals of different size ranges suitable for hydrocarbon diffusion measurements. Each of these synthesis procedures is described in detail below.

(*1*) ZIF-8-90 mixed-linker crystals of ~100 μm size were synthesized by modifying the procedure reported by Cravillon *et al*.[94] A solution of 0.544 g (8 mmol) ofNaCOOH, *x* mmol of 2-MeIm (ZIF-8 linker), and (8-*x*) mmol of OHC-Im (ZIF-90 linker) was dissolved in 40 ml of MeOH. The value *x* was 0-8. A mixture consisting of 0.595 g (2 mmol) of $Zn(NO_3)_2 \cdot 6H_2O$ dissolved in 40 ml MeOH was poured into 2-MeIM/OHC-IM solution. The resulting solution was heated at 90°C for 24 hr in a sealed glass jar. The large crystals formed on the walls were collected and washed several times with DI- H_2O and MeOH, and then dried in an oven at 80°C.

(*2*) ZIF 8-90 crystals in the 10 μm range were synthesized as reported by Thompson *et al*.[87] A solution of *x* mmol of 2-MeIM, (20-*x*) mmol of OHC-IM and 20mmol of $NaCO_2H$ in 50 ml of MeOH was prepared. The value *x* was 0- 20. The solution was stirred and heated at 50 °C until it became clear, and then cooled to room temperature. A solution of 5 mmol of $Zn(NO_3) \cdot 6H_20$ in 50 ml of DI- H_2O was prepared, poured into the first solution, and the resulting mixture was allowed to stir at room temperature for 1 hr. ZIF crystals were collected by centrifugation at 7500 rpm for 7 min, washed in MeOH three times, and dried in an oven at 80 °C.

(*3*) ZIF-8 crystals of 338 nm average size were synthesized as reported by Lai *et al*.[25] 22.7 g (276.5 mmol) of 2-MeIM (ZIF-8 linker) was added to 70mL DI-water and stirred with a magnetic bar until the solution became clear at room temperature. A mixture consisting of 1.17 g (3.7 mmol) of $Zn(NO_3)_2 \cdot 6H_2O$ dissolved in 18 mL DI- H_2O was poured into the 2-MeIM/DI-water solution and stirred at room temperature for 12 hr. The resulting milky solution was centrifuged at 9000 rpm for 15 min followed by washing with MeOH and DI-H_2O three times to collect the ZIF crystals, which were then dried in an oven at 80°C.

(*4*) ZIF-90 crystals of 55.7 μm average size were synthesized by modifying the procedure of Gee *et al*.[35] 3.84 g (40 mmol) of OHC-IM and 2.97 g (10 mmol) of $Zn(NO_3)_2 \cdot 6H_2O$ were added to 100mL DMF. The solution was heated to 120 °C while stirring for 10 min in a glass jar. The light-orange colored solution was poured into a wide-necked bottle and capped for 24 hr at room temperature. The large crystals on the walls were collected, washed extensively with DI-H_2O and MeOH, and dried in an oven at 80 °C.

2.2.3 Characterization

Characterization. XRD patterns were measured on a PANalytical X'Pert Pro diffractometer at room temperature using Cu Kα radiation of $\lambda = 0.154$ nm and 5-40° 2θ. Crystal size distribution (CSD) analyses were conducted with a Protein Solutions DynaPro DLS instrument, a Hitachi SU 8010 SEM, and a Nikon Eclipse 50i optical microscope. The CSD of 338 nm ZIF-8 was obtained by DLS. The ZIF-8 powder was dispersed by sonication in a filtered MeOH solution for 5 min. The colloidal suspension was inserted into a cuvette via a 5 μm syringe filter for DLS measurements. CSDs of 1-10 μm ZIF-8-90 materials were measured from multiple SEM images to obtain sample sizes of more than 200 crystals in each case. CSD of ZIF crystals greater than 30 μm in size were obtained by optical microscopy. The samples were dispersed on a slide glass and the CSD was measured from about 200 crystals in each case. Since large ZIF crystals are highly faceted, the equivalent spherical crystal radius was taken to be that of the smallest circle that encompasses the entire crystal. Solution ^{1}H-NMR measurements were performed with a Bruker 400 MHZ spectrometer after digesting the ZIF crystals in d4-acetic acid (CD_3CO_2D). To determine the fraction of each imidazole linker in the ZIF materials, the integrated peak area of the methyl protons of 2-MeIM (chemical shift 2.65 pm) was

normalized to that of the aldehyde proton of OHC-Im (9.84 pm). The chemical shifts of both imidazole linkers was referenced to the chemical shift (2.30 pm) of d4-acetic acid. Powder FT-Raman spectroscopy was performed with a Bruker Vertex 80v FTIR/RAM II FT-Raman Analyzer in open atmosphere and a He/Ne red laser (1054 nm). Raman microscopy of individual ZIF crystals was carried out using a Horiba Jobin-Yvon HR-800 dispersive spectrometer with an 1800 l/mm grating and a green laser (532nm). A spot size of 2.5 μm was used. Numerical integration of FT-Raman and micro-Raman peak areas was carried out with the instrument software. The 2-MeIM and OHC-IM peaks were background-subtracted using a polynomial, and then fitted with mixed Gaussian–Lorentzian functions to obtain the integrated peak areas.

Adsorption and Diffusion Measurements. For Pulsed field gradient (PFG)-NMR measurements, samples were prepared in standard 5 mm o.d. NMR tubes. Sample loadings were calculated from adsorption isotherms given by Zhang et al.[11] Loadings were limited at 10-15% below saturation loading for all adsorbates. This range was chosen to avoid bulk condensation of liquid adsorbates in the NMR tube. The sample tubes were capped, thoroughly sealed using Parafilm and allowed to equilibrate for 48 hours before experiments were performed. The diffusivity experiments were performed using a Bruker Avance III NMR spectrometer equipped with a Diff-50 diffusion accessory operating at an ^{1}H frequency of 400 MHz. The stimulated spin echo pulse sequence was used to collect the NMR data and processed using Bruker's TopSpin™ software package. It was verified that the experimental conditions were chosen appropriately for measurements of intracrystalline diffusion (i.e., the average displacement of molecules during the diffusion time δ is significantly smaller than the crystal size). Adsorption isotherms for water and

alcohols were collected using a VTI SA Vapor Sorption Analyzer (TA Instruments). Approximately 10-20 mg samples were used for each experiment. The samples were degassed *in situ* at 105°C for up to 8 hours in an ultrapure N_2 stream. The relative vapor pressure of each adsorbate was varied between the limits of 0.04 and 0.9 in discrete steps. Equilibrium was assumed to be achieved if less than 0.003% weight change was observed in a 5-minute interval.

2.3 Results and Discussion

Crystal Composition - In general, one expects thermodynamic and kinetic differences in the incorporation of the two different linkers in the ZIF crystal structure. As a result, the percentage (x) of ZIF-8 linkers in the crystallized material is not identical to that originally present in the synthesis solution. It is therefore necessary to establish the 'composition curve' that relates the two quantities and allows selection of the appropriate synthesis solution for a particular hybrid ZIF-8-90 material. Solution-phase ^{1}H-NMR spectroscopy is a reliable tool for this purpose, and the composition curves thus determined are shown in Figure 2.1. Due to the different synthesis conditions (and hence different crystallization characteristics) used in the synthesis of 'smaller' (< 10 μm) and 'larger' (> 50 μm) ZIF-8-90 crystals, the composition curves are different for the two cases. Overall, it is seen that 2-MeIM is incorporated into the frameworks at lower fractions than present in the initial reactant solution. The data in Figure 2.1 is in good agreement with our initial data for small crystals of ZIF-8-90 materials.[87] Based upon the foregoing results, it is clear that ZIF-8-90 hybrids of any composition and a large range of average crystal sizes can be synthesized by the combination of techniques used in this thesis.

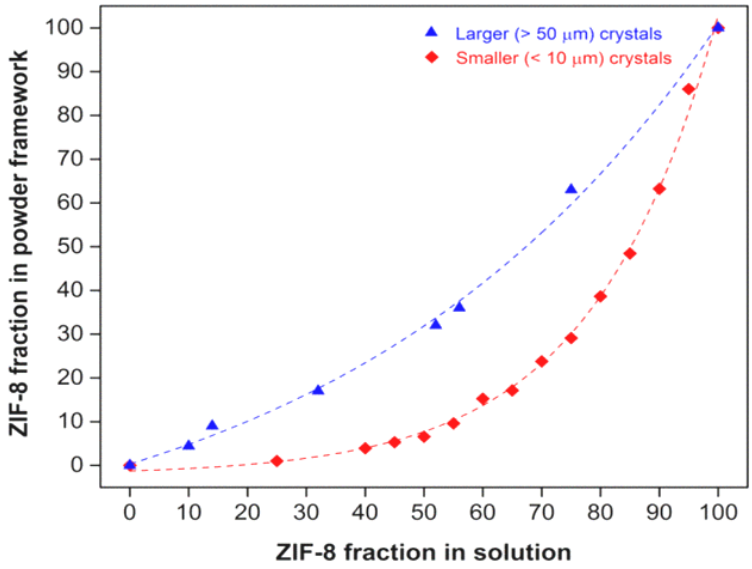

Figure 2.1. Composition analysis curves of ZIF-8_x-90_{100-x} hybrid frameworks obtained by solution ^{1}H-NMR. Composition curves for smaller (<10 μm) and larger (> 50 μm) crystals are shown. The composition of the hybrid materials can be continuously tuned by adjusting the composition of the synthesis solution. The dashed lines are only a guide to the eye.

The XRD patterns of all ZIF-8-90 materials (Figure 2.2) are essentially identical because all the materials have the same framework topology and only small differences in electron density and lattice constant. In these circumstances, the slight changes in peak positions or intensities make it difficult to obtain any reliable evidence of compositional variations by XRD techniques. Previously[87], we provided indirect evidence (via N_2 physisorption measurements) that the crystallized ZIF-8-90 materials were true hybrids and not physical mixtures of ZIF-8 and ZIF-90 crystals. However, conclusive evidence of hybrid crystal formation, as well as the distribution of the ZIF-8 linker fraction (x) across individual crystals, can only be obtained from a microanalytical technique. Here we use a comparative approach based upon micro-Raman and powder FT-Raman spectroscopy.

Figure 2.3a shows powder FT-Raman spectra from several ZIF-8-90 materials. We use the peaks at 680 cm^{-1} (ring puckering of 2-MeIM) and 1680 cm^{-1} (C=O stretching vibration of OHC-Im) as signatures[11-13] of the ZIF-8 and ZIF-90 linkers, respectively. The ZIF-8 spectrum in this range is dominated by two intense peaks at 1146 cm^{-1} and 1180 cm^{-1} corresponding to the υ_{C5-N} vibrations of the 2-MeIM ring, while the same vibrations in the ZIF-90 spectrum (OHC-IM linker) appear at 1036 cm^{-1} and 1200 cm^{-1}. In the hybrid ZIF-8-90 frameworks, all four υ_{C5-N} peaks are observed due to the presence of both linkers. As the 2-MeIM content increases, the intensity of the OHC-IM peaks decreases and they are eliminated in pure ZIF-8. The other peaks originating from 2-MeIM and OHC-IM also display similar behavior as a function of framework composition, namely the 2-MeIM peaks at 1370 cm^{-1} (δ_{CH3}), 1458 cm^{-1} (δ_{C-H}), and 1499 cm^{-1} (υ_{C2-N1}) and the OHC-IM peaks at 1330 cm^{-1} (δ_{H-CO}), 1360 cm^{-1} (δ_{C-H}), and 1418 cm^{-1} (υ_{C2-N1}). These changes are consistent in both the FT-Raman and micro-Raman spectra.

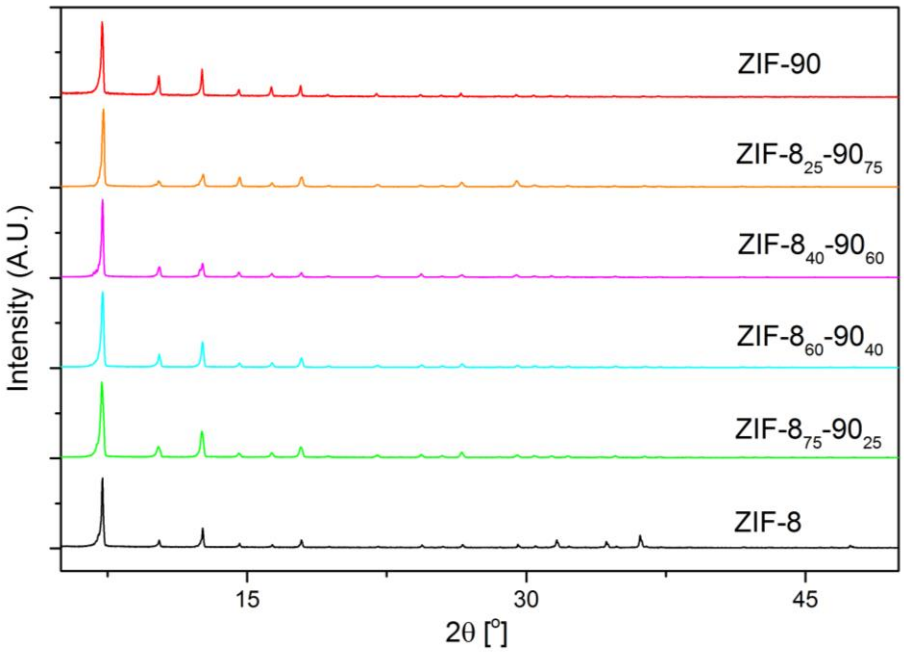

Figure 2.2. XRD patterns of ZIF-8, ZIF-90, and mixed-linker ZIF-8-90 materials with different linker ratios.

The integrated areas (I_{ZIF8} and I_{ZIF90}) of the signature peaks at 680 cm^{-1} (2-MeIM) and 1680 cm^{-1} (OHC-Im) were obtained in each FT-Raman spectrum, and the normalized quantity $X = 100 \times I_{ZIF8}/(I_{ZIF8}+I_{ZIF90})$ was used as a measure of the percentage of ZIF-8 linkers in the framework. A similar procedure is carried out using micro-Raman spectra collected from at least six randomly selected individual crystals in each sample, and at three different locations on each selected crystal. Figure 2.3b shows example micro-Raman spectra from one crystal in each ZIF-8-90 sample. The quantity X allows the cancellation of sample size effects, but is not the exact equivalent of the ZIF-8 linker fraction (x) because of the different polarizabilities of the two characteristic linker vibrations. However, if the crystals are true hybrids, the 'bulk' macroscopic value of X obtained from a powder FT-Raman measurement must be similar to that obtained microscopically by micro-Raman

measurements from individual crystals and locations in the sample. Moreover, a small standard deviation of *X* (as obtained from averaging the micro-Raman measurements over multiple crystals) would denote a highly uniform value of the ZIF-8 linker percentage *x* across crystals in a given powder sample. Figure 2.3c plots the values of *X* obtained from FT-Raman and micro-Raman measurements versus the values of *x* obtained previously from ^{1}H-NMR measurements. The FT-Raman and micro-Raman techniques are in close agreement, providing clear evidence that the crystals are true mixed-linker hybrids. The generally small standard deviations (represented as horizontal error bars in Figure 2.3c) of *X* also indicate good compositional uniformity of the ZIF-8-90 crystals. It is important to note that the above discussion does not provide insight on the *molecular-level* distribution of the two different linkers within the ZIF crystals. As recently shown, such understanding could be obtained in a specific MOF system through a combination of NMR spectroscopy and structure modeling.[62] This approach is described in detail in Chapter 3. This chapter is focused on demonstrating the role of linker substitution in obtaining large changes in adsorption and diffusion behavior.

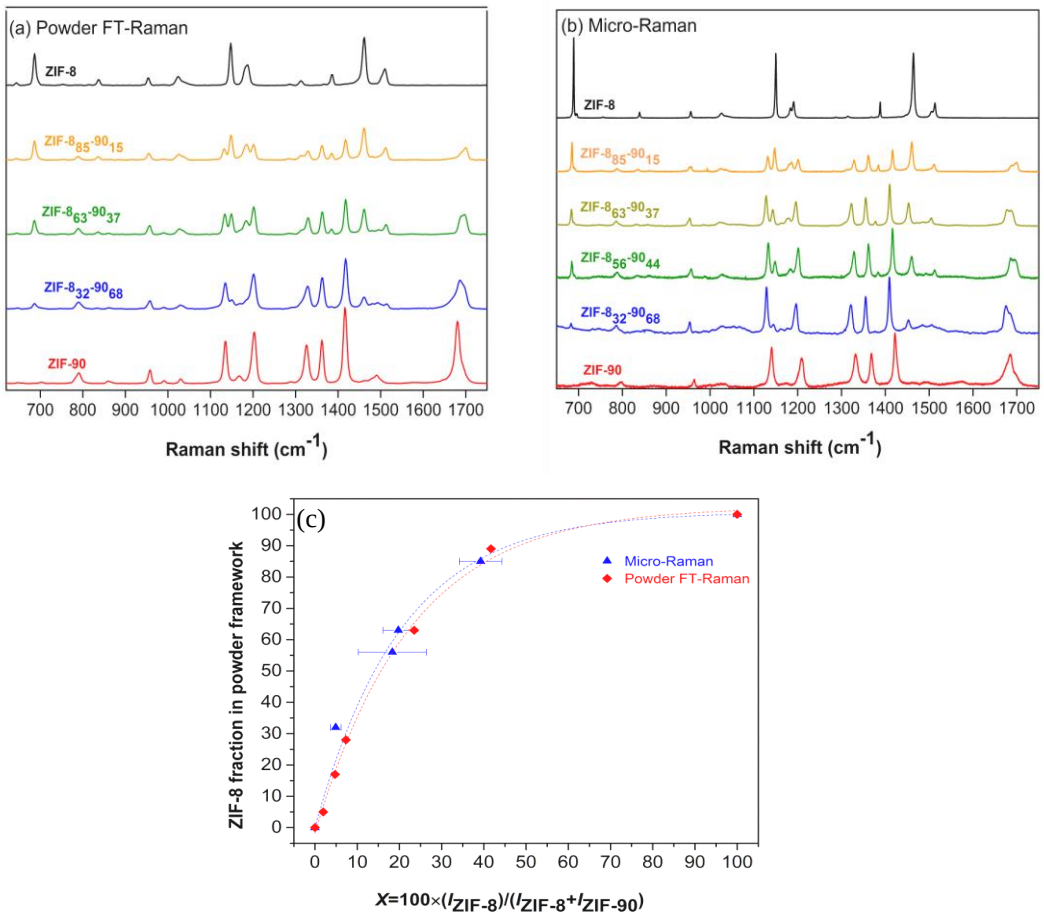

Figure 2.3. (a) Powder FT-Raman spectra of ZIF-8-90 hybrid framework materials, (b) micro-Raman spectra from individual ZIF-8-90 crystals, and (c) composition analysis of ZIF-8-90 hybrid crystals from FT-Raman and micro-Raman data. The quantity X = $100\times I_{ZIF-8}/(I_{ZIF-8}+I_{ZIF-90})$ is obtained from the Raman measurements whereas the quantity y is the corresponding ZIF-8 linker fraction obtained from ^{1}H-NMR. The error bars shown for the micro-Raman curve represent the standard deviation in X across at least six different crystals of the sample and three different locations in each crystal.

Adsorption - Drastic changes are seen in the adsorption of water and alcohols upon tuning the ZIF-8-90 composition. Figure 2.4a shows water vapor adsorption isotherms in ZIF-8-90 materials at 308 K. It is clear that the hydrophobicity of ZIF materials can be tuned by controlling the composition of different linkers in the hybrid framework. As the fraction of hydrophilic carbonyl groups in the structure increases from pure ZIF-8 to pure

ZIF-90, water uptake starts to occur at lower relative pressures. The water adsorption isotherm for a physical 50-50 wt% mixture of ZIF-8 and ZIF-90 crystals is entirely different from that of a ZIF-8_{50}-90_{50} hybrid material. This is further corroboration that the 2-MeIm and OHC-Im linkers are forming true hybrid ZIFs. Figure 2.4b shows n-butanol adsorption isotherms at 308 K. It is clear that the organophilicity of ZIFs can be tuned significantly, especially in the initial plateau region at low relative pressures, by adjusting the linker fraction (x). This region of low activity is significant for the concentration of n-butanol (and other organics) from dilute aqueous solutions, a problem often encountered in biofuel and biobased chemical production.[95-97] For example, n-butanol uptake into pure ZIF-8 only occurs at $P/P_0 > 0.06$. By progressively replacing methyl groups with carbonyl groups, the hybrid ZIF-8-90 framework attracts a much larger number of n-butanol molecules at low pressures. The characteristic S-shape isotherms (Figure 2.4a) are not uncommon for ZIF materials with inherent structural flexibility that can undergo structural transformation induced by temperature, pressure, or guest molecules. The 'gate-opening' effect, *i.e*. the reorientation of the imidazole linkers, was proposed to explain the inflections in experimental N_2 physisorption isotherms at 77 K.[98] The inflection points are at relative pressures of about 5×10^{-3} for ZIF-8 and about 10^{-4} for ZIF-90. However, the alcohol adsorption mechanism is different from that of cryogenic N_2 adsorption and is not related to the gate-opening effect. In ZIF-8, the gate-opening effect can only be obtained at high hydrostatic pressures or ultra-low-pressure N_2 adsorption at 77 K.[34] More importantly, gate-opening is characterized by a hysteresis loop that marks the transformation between a less porous and a more porous phase induced by guest molecules.[99] Figure 2.5 shows representative adsorption and desorption branches at 323 K for water and ethanol in ZIF-

8, ZIF-90, and ZIF-8_{50}-9_{50}. There is no desorption hysteresis, which indicates the S-shape isotherms are not due to the gate-opening effect but rather a cluster-formation and cage-filling mechanism. In a previous study of ethanol sorption in ZIF-8, no desorption hysteresis was observed.[92] The S-shape ethanol sorption isotherm in ZIF-71, a hydrophobic ZIF with RHO topology, has also been identified as a cluster formation and cage-filling mechanism *via* molecular simulations.[100] A more recent simulation study revealed that the cluster formation and cage-filling mechanism also holds for the adsorption of normal alcohols (methanol, ethanol, propanol and butanol) in SOD-type ZIF materials such as ZIF-8.[36] At low loadings, the alcohol molecules form clusters at preferential adsorption sites around the organic linkers. With increasing vapor pressure, cage-filling occurs with a large saturation uptake of alcohol molecules. Framework flexibility has a negligible effect on equilibrium alcohol adsorption in ZIF-8 and ZIF-90.[35] These studies further corroborate our finding that the tunability of water and n-butanol adsorption in hybrid ZIF-8-90 frameworks is a direct result of the tunable linker fractions, and not an indirect result of changes in framework flexibility or gate-opening.

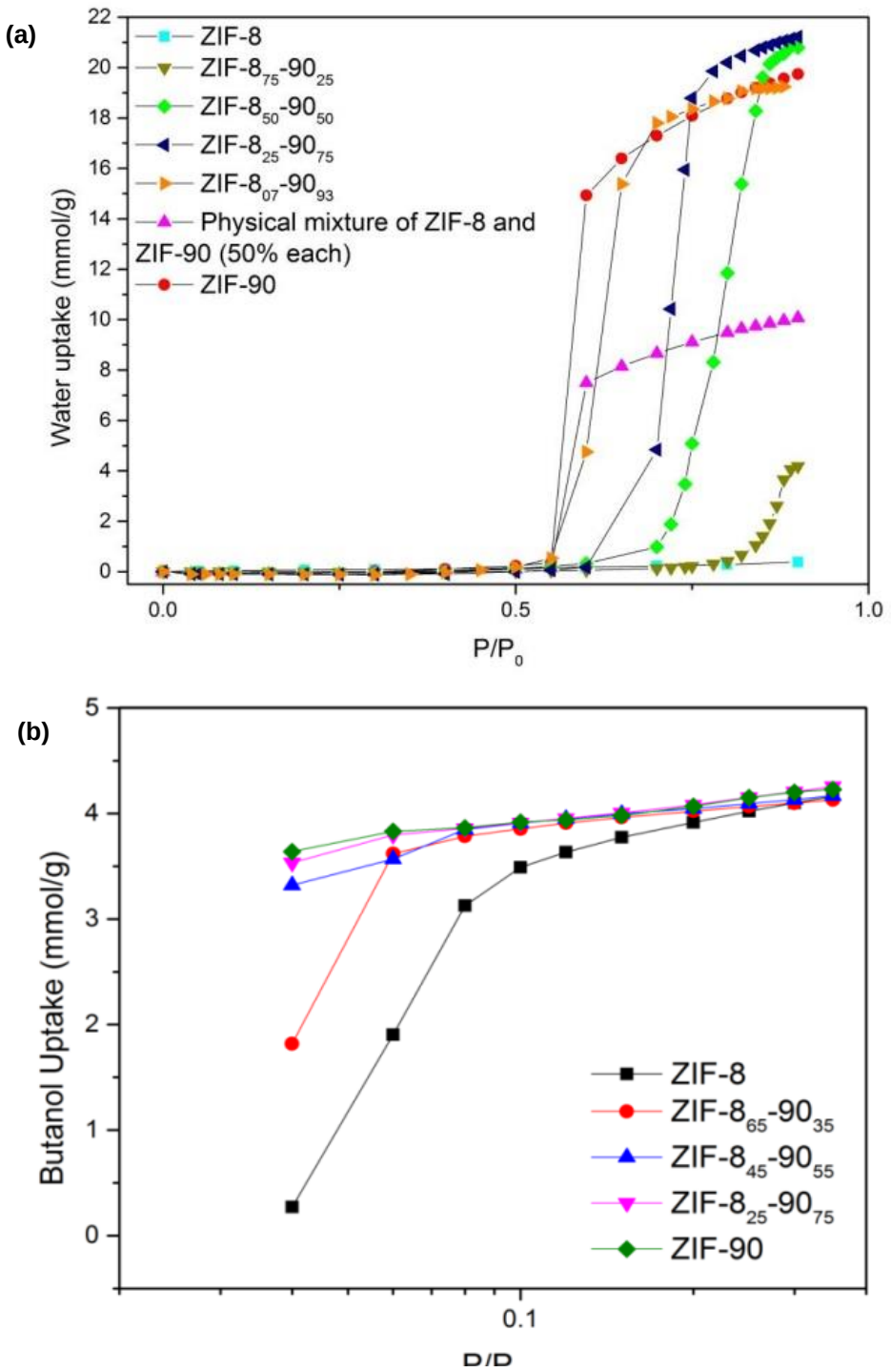

Figure 2.4. (a) Water adsorption isotherms in ZIF-8-90 hybrid crystals at 308 K, and the adsorption isotherm of a 50-50 (by mass) physical mixture of ZIF-8 and ZIF-90 crystals, (b) n-butanol adsorption isotherms in ZIF-8-90 hybrid crystals at 308 K.

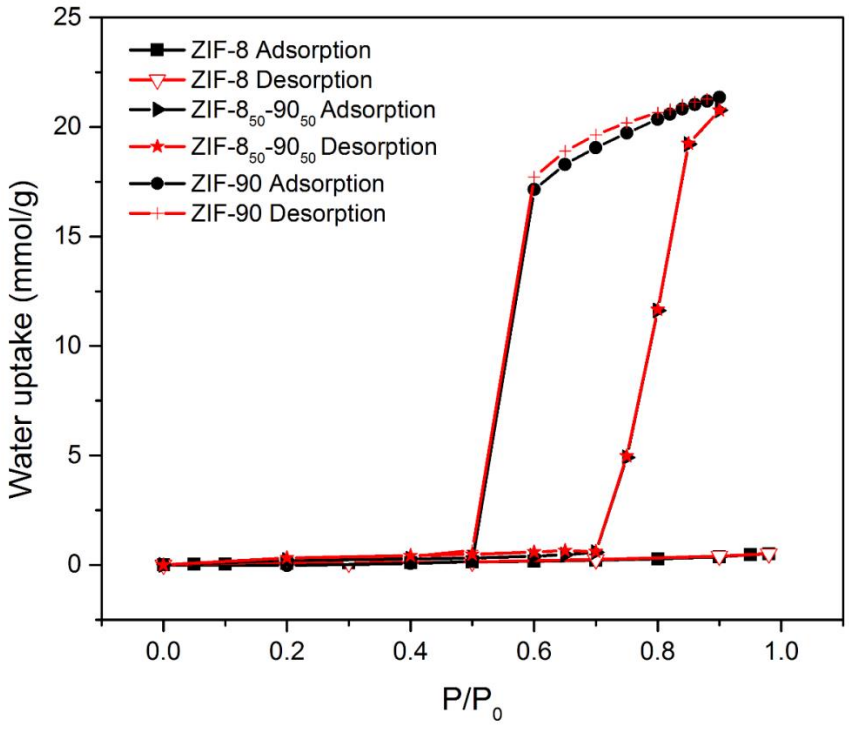

Figure 2.5. Adsorption and desorption branches of the isotherms for water at 308 K in ZIF-8, ZIF-90 and ZIF 8_{50}-90_{50} hybrid materials.

Diffusion - The self-diffusivities of the three smaller molecules (water, methanol and ethanol) were measured by PFG-NMR.[101] Due to their high diffusivities, gravimetric uptake measurements of diffusion were not feasible in these cases even with the largest crystals available. The PFG-NMR signal attenuation data were fitted to a double-exponential curve to obtain the self-diffusivity coefficient. The dominant fast diffusion component in the decay curve reflects the diffusion of the water/alcohol while the minor component has been attributed to a background signal from remaining solvent.[102-103] The diffusivity of water in ZIF-8 was not measured due to its high hydrophobicity. The two bulkiest molecules (butanol and isobutanol) exhibited very poor signal-to-noise ratios in PFG-NMR data. This is due to the restricted rotational motion of the molecules, which manifests itself in a short transverse relaxation constant T_2. Hence, their M-S diffusivity

was measured gravimetrically and the uptake data was analyzed using methods similar to those used for the hydrocarbon isomers.

Figure 2.6 shows that there is no appreciable change in water self-diffusivity for water as the linker composition is varied. This is due to the much smaller kinetic diameter of water (2.6 Å) in relation to the effective pore sizes of all the ZIF-8-90 materials. The diffusivity of methanol shows a small but systematic increase with decreasing ZIF-8 linker fraction. Ethanol shows an order-of-magnitude tunability of self-diffusivity and M-S diffusivity, whereas butanol and isobutanol show over two orders-of-magnitude tunability of the M-S diffusivity as a function of the linker composition. As the size of the diffusing molecule increases, the effective pore size has a more pronounced effect on the diffusivity at a given linker composition, as well as the sensitivity of the diffusivity to changes in the linker composition. This behavior strongly corroborates the molecular sieving nature of the observed diffusion characteristics in the mixed-linker ZIF-8-90 series. The self-diffusivities of methanol and ethanol in pure ZIF-8 and ZIF-90 are in good agreement with those measured previously by PFG-NMR.[35] The ethanol diffusivity in ZIF-8, previously measured using infrared microscopy (IRM)[102], also compares well with Figure 2.5. The diffusivity trend for isobutanol shows another interesting feature, which is the relatively smaller diffusivity change occurring in the x=20-80 range. This is explained based on upon the fact that the effective pore sizes of the hybrid materials do not vary linearly as a function of composition. In previous work[17], we measured the effective pore sizes of ZIF-8-90 materials by N_2 physisorption at 77 K and showed that it increased from 4.0 Å to 4.3 Å as x decreased from 100 to 76. Between x=76 to x=25, the increase in pore size is slower (from 4.3 Å to 4.5 Å). Thereafter, a large increase from 4.5 Å to 5.0 Å occurs over a small

composition range of x=25 to x=0. With a kinetic diameter of 5.4 Å, isobutanol is by far the largest molecule among the set considered here. Due to its large size, its diffusion behavior follows the above trends in the effective pore size most closely. In other words, we observe the most significant changes in isobutanol diffusivity in the ZIF-8-rich and ZIF-90-rich regions (x > 80 or x < 20) and only moderate changes in the middle region.

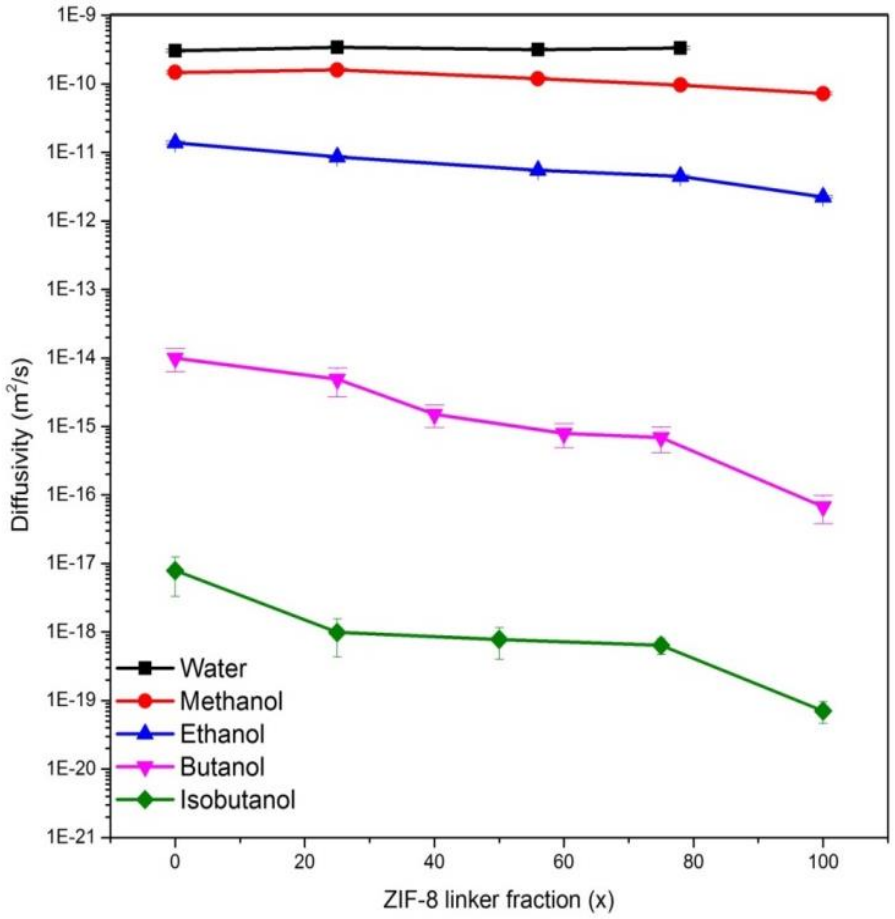

Figure 2.6. Self-diffusivities and M-S diffusivities of molecules in ZIF-8-90 hybrid materials. Water, methanol, and ethanol self-diffusivities were measured by PFG-NMR at 313 K. Butanol and isobutanol M-S diffusivities were measured by gravimetric uptake at 308 K.[104]

Figure 2.7 shows the ideal diffusion selectivity versus linker fraction in mixed-linker ZIF-8-90 materials. It is evident that by adjusting the fraction of each linker, the

diffusion selectivity for water over n-butanol and water oven isobutanol can be tuned over two orders of magnitude. For the case of butanol over isobutanol, the range of selectivity is restricted, but the selectivity is still high (> 100) in all cases. This makes ZIF-8-90 mixed-linker materials potential candidates for kinetic separation of small molecules using membrane-based technology.

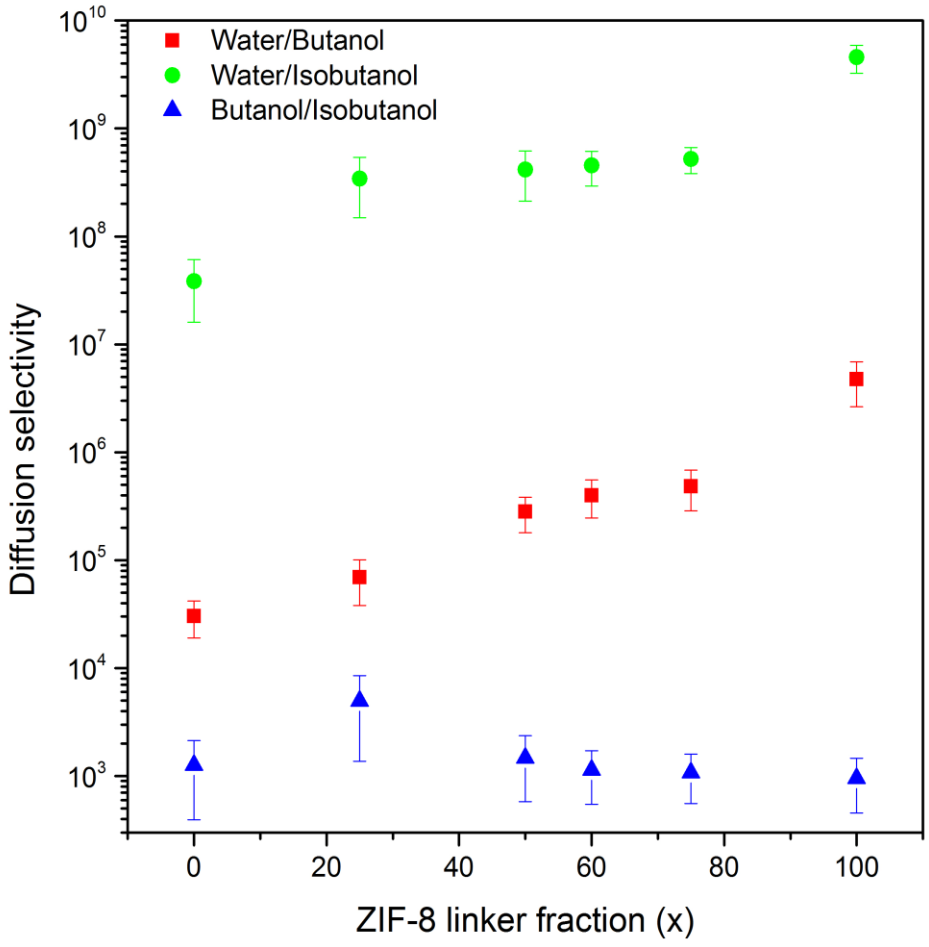

Figure 2.7. Ideal diffusion selectivities for three binary mixtures in mixed-linker ZIF-8-90 materials.

2.4 Conclusions

This chapter has demonstrated the continuous tuning of molecular sieving and adsorption behavior in mixed-linker ZIF-8-90 frameworks, which is due to the tunability of effective pore size as well as the ratio of polar and non-polar functional groups in the framework. These results are facilitated by the synthesis of a range of ZIF-8-90 mixed linker materials. Micro-Raman composition analysis of individual ZIF-8-90 crystals conclusively shows the hybrid nature and high uniformity of the mixed-linker materials. Tunable molecular sieving is observed in strongly polar alcohols, and tunable adsorption behavior is primarily observed for polar molecules like water and alcohols. Diffusion measurements of water and alcohols also reveal the strong dependence of tunable diffusivity on the molecular sizes and ZIF-8-90 pore sizes. The adsorption affinities of water and alcohols at low pressures are also strongly tunable by the variation of linker composition. This detailed demonstration of tunable adsorption and diffusion properties in ZIF-8-90 materials opens up the wider applicability of mixed-linker ZIF materials as a platform for a variety of membrane-based and adsorption-based molecular separations.

This work also indicates that rational synthesis of mixed-linker MOF materials tailored for specific separations will require a deeper understanding of their microstructures. Specifically, the knowledge on spatial distribution of linkers is key to making highly accurate predictions on their molecular adsorption and transport properties. So far, this information on mixed-linker ZIFs has remained elusive due to the inability of conventional diffraction techniques to distinguish between ZIF-8 and ZIF-90 unit cells. In the next chapter, we will present advanced NMR-based techniques to extract this information. This novel approach combines the use of established NMR pulse sequences

with computational modeling of structures and NMR spectra to provide an in-depth understanding of mixed-linker ZIF structure at previously unattained length-scales.

CHAPTER 3. STRUCTURE ELUCIDATION OF MIXED-LINKER ZEOLITIC IMIDAZOLATE FRAMEWORKS

3.1 Introduction[2]

In recent years, the continuous tuning of hydrocarbon and alcohol diffusivities over several orders of magnitude by varying the relative composition of ZIF-7, ZIF-8 and ZIF-90 linkers in mixed-linker ZIF-8-90 and ZIF-7-90 materials have been demonstrated.[44, 104] In the previous chapter, we studied ZIF-8-90 mixed-linker materials in detail and based on evidence from water adsorption and micro-Raman measurements, it was shown that these mixed-linker ZIF materials incorporate both types of linkers in the same crystal and are not physical mixtures of single-linker ZIFs. However, no direct information about the unit-cell-level distribution/mixing of linkers could be gained from these measurements. The distribution of linkers lining the windows determines the pore sizes and shapes, and thereby the diffusion rate of molecules through the pores. In related work, several studies have demonstrated the use of computational techniques to screen ZIFs as potential candidates for specific separation processes.[105-109] However, it is not currently possible to simulate or predict the properties of experimental mixed-linker ZIFs, since the molecular-level linker mixing characteristics of these materials are unknown. Understanding the spatial distribution of the linkers in mixed-linker frameworks is expected to be important in understanding how adsorption and diffusion properties can be controlled, and furthermore

[2] Work in this chapter has been published previously in Krishna C. Jayachandrababu, Ross J. Verploegh, Johannes Leisen, Ryan C. Nieuwendaal, David. S. Sholl, Sankar Nair, "Structure Elucidation of Mixed-Linker Zeolitic Imidazolate Frameworks by Solid-State ^{1}H CRAMPS NMR Spectroscopy and Computational Modeling", Journal of the American Chemical Society, 137, p.7325-7336.

in selecting or designing appropriate linker combinations and compositions for a targeted separation process.

Due to the large degree of compositional disorder in mixed-linker ZIFs, crystallographic techniques cannot be used as a primary method for elucidating their structure. However, solid-state NMR spectroscopy can distinguish between the nuclear environments of different functional groups, for example in the study of domain sizes in block copolymers.[56-57, 110-111] Recently several groups have demonstrated the use of NMR spectroscopy to study structural properties of MOFs. Rossini et al. used DNP-enhanced NMR spectroscopy to obtain rapid, high S/N ratio measurements of the presence and qualitative location (e.g., surface versus bulk) of functional groups in several compositional variants of the MOF (In)-MIL-68.[112] Baias et al. used ^{1}H NMR spectroscopy in conjunction with X-ray crystallography to determine the local structure of a substituted imidazole based MOF (SIM-1).[64] With this technique, it was possible to deduce the relative orientation of functional groups that were present on the same linker molecule and their distribution within the framework. It was shown by Kong et al. that REDOR NMR can be used to estimate the linker distribution in multivariate (MTV) MOFs.[62] This technique requires isotopic labeling with ^{13}C and ^{15}N nuclei, since ^{13}C is only 1.1 % naturally abundant (and hence insensitive), and ^{14}N is a spin-1 nucleus (which is less amenable to REDOR). Kranjc et al. reported ^{1}H NMR spin diffusion experiments that showed that the large difference in the (known) ordered distributions of linkers in two aluminum-based MOFs (DUT-5) could be distinguished when using 20 kHz magic angle spinning (MAS) and RFDR ^{1}H-^{1}H recoupling.[63] Here, we demonstrate the use of ^{1}H CRAMPS spin diffusion experiments with 5 kHz MAS and no recoupling in conjunction with computational modeling of mixed-

linker ZIFs for estimating the linker distributions in multiple mixed-linker ZIF materials that are all mixed on size scales of ≈1 nm, which is a significant departure from previous work. We focus particularly on ZIF-8-90 hybrids as a typical example for such a challenging system and note that routine Fickian-based spin diffusion analysis protocols cannot be used for distinguishing structures on these short length scales. This methodology does not require isotopic enrichment for the NMR measurements, and allows a more generalized way of determining the structures of mixed-linker MOFs when one assumes a relatively simple, phenomenological spin exchange model. When two different types of linkers (with NMR-distinguishable protons) are distributed ('mixed') in the framework, the distribution of nearest neighbor inter-nuclear distances between the two functional groups will depend upon the degree of mixing. For example, in a clustered linker distribution (where each type of linker forms isolated phases) the distance distribution between linkers of two different types will be very different from more random or highly ordered linker distributions. By measuring spin exchange rates using NMR, and matching them to dipolar couplings calculated from the proton positions from computationally generated models, one can ascertain the level of linker mixing in the materials of interest.

We have used the short-range order (SRO) as defined by the Warren-Cowley parameter α to quantify the degree of linker mixing.[113] This parameter is defined as:

$$\alpha = 1 - \frac{P_j^{A(B)}}{x_B} \qquad (1)$$

where $P_j^{A(B)}$ is the conditional probability of finding the linker of type B at the j^{th} neighbor site given a linker of type A, and x_B is the fractional composition of linker type B in the

material. For hybrid ZIF-8-90 systems, we have selected the nearest neighbor (j=1) to define α. Nearest neighbors (NNs) are not assigned based on the value of the distance but are based upon the sharing of a common Zn^{2+} center; therefore, each organic linker has 6 NNs. The contribution of second order NNs, (*i.e.*, those connected through two Zn metal centers) are assumed to be negligible (see below). Figure 3.1a shows the NN convention and Figure 3.1b shows a schematic of a ZIF-8_{50}-90_{50} hybrid 2×2×2 unit cell in which the linkers are randomly distributed. The experimentally measured spin diffusion curves of different mixed-linker ZIFs can be compared to the computationally generated spin diffusion curves of structures with different SROs to identify the value of α that best describes the synthesized material. Note that for the calculation of spin exchange rates, multiple quantum effects, magic angle spinning effects, molecular dynamics, and long range couplings are ignored. The physical significance of this short-range order is demonstrated by showing how the window-type distribution varies as a function of α. Since the diffusion of guest molecules through the cages of a ZIF material is governed by the type of linkers that line the window, this distribution is critical in determining how material transport is a function of the relative composition of constituent linkers.

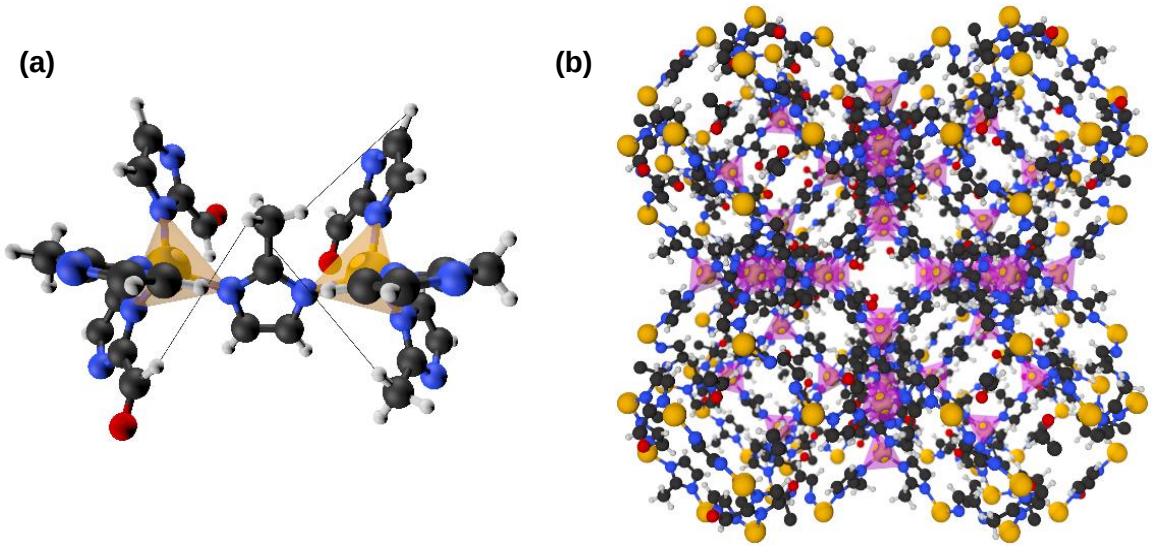

Figure 3.1. Schematic demonstrating nearest neighbor convention based on bond connectivity where the central mIm linker has 3 OHC-Im and 3 mIm NNs. **(b)** Schematic of a ZIF-8_{50}-90_{50} hybrid 2×2×2 supercell where the OHC-Im linkers are randomly distributed. Atom representations are as follows: O=red, N=blue, H=off-white, C=black, and Zn=gold. Yellow **(a)** and purple **(b)** tetrahedrons are included to illustrate the 4-coordinated Zn atoms.

3.2 Experimental Methods

3.2.1 Synthesis of ZIF materials.

ZIF-8: 0.324 g 2-methylimidazole and 0.538 g sodium formate were dissolved in 40 mL methanol. This solution was mixed with another solution of 0.588 g zinc nitrate hexahydrate in 40 mL methanol. The resulting mixture was stirred for 1 minute and then sealed in a jar and heated to 90^{o} C for 24 hours. The crystals formed were collected and washed with fresh methanol. The washing process was followed by centrifugation at 7500 rpm for 5 minutes. The washing-centrifugation process was repeated twice more. The crystals were air dried at 60^{o} C and then degassed in vacuum at 160^{o} C for 24 hours.

ZIF-90: 5.952 g zinc nitrate hexahydrate and 7.684 g imidazole-2-carboxaldehyde were dissolved in 200 mL N,N-dimethylformamide. The resulting solution was then heated to 120^{o} C for held at that temperature for 10 minutes. The solution was then cooled down to room temperature and then left undisturbed for 2 days. The resulting crystals were then collected and washed in methanol. The washing process was followed by centrifugation at 7500 rpm for 5 minutes. The washing-centrifugation process was repeated twice more. The crystals were air dried at 60^{o} C and then degassed in vacuum at 160^{o} C for 24 hours.

ZIF-8-90: Table 3.1 describes the synthesis compositions. The linkers and sodium formate were mixed in 100 mL methanol and dissolved completely by heating to 60^{o} C. The solution was allowed to cool down to room temperature. Zinc nitrate was dissolved in 100 mL deionized water. The two solutions were mixed and stirred for 24 hours. The crystals were recovered by centrifugation at 7500 rpm. The crystals were then washed with

fresh methanol and centrifuged thrice followed by air drying at 60^{o} C. The crystals were degassed in vacuum at 160^{o} C for 24 hours.

Table 3.1. Material quantities for synthesizing ZIF-8-90 mixed-linker materials.

Material	**$Zn(NO_3)_2.6H_2O$**	**Imidazole-2-carboxaldehyde**	**2-methylimidazole**	**Sodium formate**
$ZIF\text{-}8_{25}\text{-}90_{75}$	2.974 g	0.962 g	2.464 g	2.72 g
$ZIF\text{-}8_{50}\text{-}90_{50}$	2.974 g	0.480 g	2.874 g	2.72 g
$ZIF\text{-}8_{61}\text{-}90_{39}$	2.974 g	0.384 g	2.956 g	2.72 g
$ZIF\text{-}8_{78}\text{-}90_{22}$	2.974 g	0.173 g	3.136 g	2.72 g
$ZIF\text{-}8_{89}\text{-}90_{11}$	2.974 g	0.076 g	3.218 g	2.72 g

NMR methods: NMR measurements were performed on a Bruker Avance III 400 MHz spectrometer using a standard broadband H/X MAS probe. The samples (~5 mg) were loaded into 4 mm ZrO_2 rotors, and the magic angle spinning was intentionally set to a relatively low rate (5 KHz) so as to avoid the quenching of spin diffusion; experiments performed at faster rates exhibited long onset times. No recoupling was applied during the mixing time. 2D CRAMPS experiments were conducted using the phase modulated Lee-Goldburg decoupling during the evolution and detection times (Bruker Pulse sequence: wpmlg2d).[114-116] While slightly different resolutions may be achieved using an alternative homonuclear decoupling CRAMPS technique (e.g., BR-24 or DUMBO), the results would not be affected since no pulses occur during the mixing time. The possibility of spatially heterogeneous spin temperatures, or spatial polarization gradients, should not affect the results of these 2D experiments, but could affect a 1D variation of this experiment.[117] Mixing times ranging from 0.05-50 ms were used to study the temporal evolution of spin diffusion. Other typical experimental parameters were 399.92 MHz Larmor frequency, 2.5

μs π/2 pulse width, 56.57 kHz frequency offset, 12.5 μs Lee-Goldburg 2π pulse, receiver gain of 8, 4 scans, 512x128 2D points with sine apodization.

3.3 Simulation Methods

3.3.1 ZIF-8$_x$-90$_{100-x}$ Structure Generation

The starting ZIF-8 unit cell (structure code VELVOY[17]), and the ZIF-90 unit cell (structure code WOJGEI[118]) were taken from the Cambridge structural database (CSD).[119] As a standard self-consistency check, the geometries of these two bulk ZIF structures were energy minimized using plane wave density functional theory (DFT) calculations as implemented in the Vienna Ab initio package (VASP)[120-121] version 5.2.12. The generalized gradient approximation (GGA) Perdew-Burke-Ernzerhof (PBE)[122] functional was applied along with D2 dispersion corrections by Grimme.[123] Calculations were performed at the Γ-point with a 700 eV energy cutoff. Atomic forces were converged to < 0.03 eV/Å during both unit cell and atomic position relaxations. The unit cells for the two ZIFs were subsequently expanded into 5×5×5 supercells.

A linker NN library was generated through the mIm connectivity determined using a fast percolation algorithm.[124] Using this library of linker NNs a simple Reverse Monte Carlo (RMC) procedure was implemented to generate a new linker NN library with a characteristic SRO and specified composition. A candidate linker swap that generated a NN library with a SRO closer to the target SRO, α_t, was accepted with unit probability and unfavorable moves were accepted with probability $\exp(-\beta|\alpha-\alpha_t|)$ following from the Metropolis criterion. Values of β ranged from 1 to 1000 for different target SRO values and a total of 1×10^6 MC steps were used. A fraction of mIm linkers were then chosen to

be swapped with OHC-Im linkers using the final linker NN library. This procedure was implemented by aligning the imidazole ring plane normal vectors as well as the vectors defined by the primary carbon and the nitrogen-nitrogen centers-of-mass of an OHC-Im fragment and chosen mIm linker. Organic linker fragments were taken from the DFT energy optimized bulk structures. Several representative hybrid ZIF-8_x-90_{100-x} XRD patterns calculated using Mercury CSD 3.5.1[125-128] are available in the Appendix A.

3.3.2 *Semi-Empirical Fitting of ^{1}H CRAMPS NMR Intensity Curves*

Simulated NMR intensity fit curves were generated using a kinetic model of spin exchange/diffusion using modeled proton positions as described by Perrin and Dwyer as well as Elena and Emsley.[60-61, 63, 129] This analysis assumes that relaxation of the z-(longitudinal) magnetization (parallel to the applied static magnetic field) back to its equilibrium value during spin diffusion experiments can be modeled through a system of coupled differential equations. All details of the model along with relevant equations and parameters are given in the Appendix A. This set of kinetic equations models the spin exchange behavior using the r^{-6} dependence of the exchange rate due to the dipolar coupling and assumes spin lattice relaxation occurs on time scales greater than even the longest mixing time.[130-132] To assess agreement between simulated and experimental ^{1}H NMR spectral intensities at various values of *r*, we utilized the mean absolute error (MAE):

$$MAE = \frac{1}{n}\sum_{k=1}^{n}\left|I_{sim} - I_{\exp}\right| \qquad (2)$$

where *n* is the number of data points and the subscripts 'sim' and 'exp' refer to simulated and experimental values respectively. We generated mixed-linker ZIF structures spanning the range of SRO values for a fixed composition. From this set, we determined the structure with the minimum MAE and reported a confidence interval on the corresponding SRO. The SRO confidence interval is defined from the SROs that correspond to structures that yield MAE values within ±5% of the minimum MAE structure.

3.4 Results and Discussion

3.4.1 Pure ZIF-8 and ZIF-90 NMR Analysis

The ^{1}H chemical shift signatures of the methyl group (2.6 ppm), aldehyde group (9.8 ppm) and the protons on the 4- and 5- positions of the imidazole rings (7.3 ppm) in ZIF-8 and ZIF-90 were first identified using solution NMR of samples digested in d_4-acetic acid. Based upon initial survey measurements, the spinning frequency for spin diffusion data collection was fixed at an optimum of 5 kHz. The selection of spinning frequency is important since there is a trade-off between the spectral resolution and strong dipolar coupling. At lower frequencies, the solid-state spectra were not sufficiently resolved whereas at higher frequencies the averaging of dipolar couplings slowed down spin diffusion and yielded a significant deviation from $t^{1/2}$ behavior. Figure 3.2a-b show ^{1}H-NMR spectra for ZIF-8 and ZIF-90 and example contour plots of the two materials from the CRAMPS experiment at 1 ms mixing time. The diagonal peaks (marked by solid circles) are a result of direct observation of methyl and imidazole protons. The cross peak (marked by dashed circle) is caused by magnetization transfer between the nuclei corresponding to the diagonal peaks. The presence of this cross peak shows that there is

intimate contact between the imidazole protons and the methyl protons in ZIF-8 as well as the imidazole protons and aldehyde proton in ZIF-90.

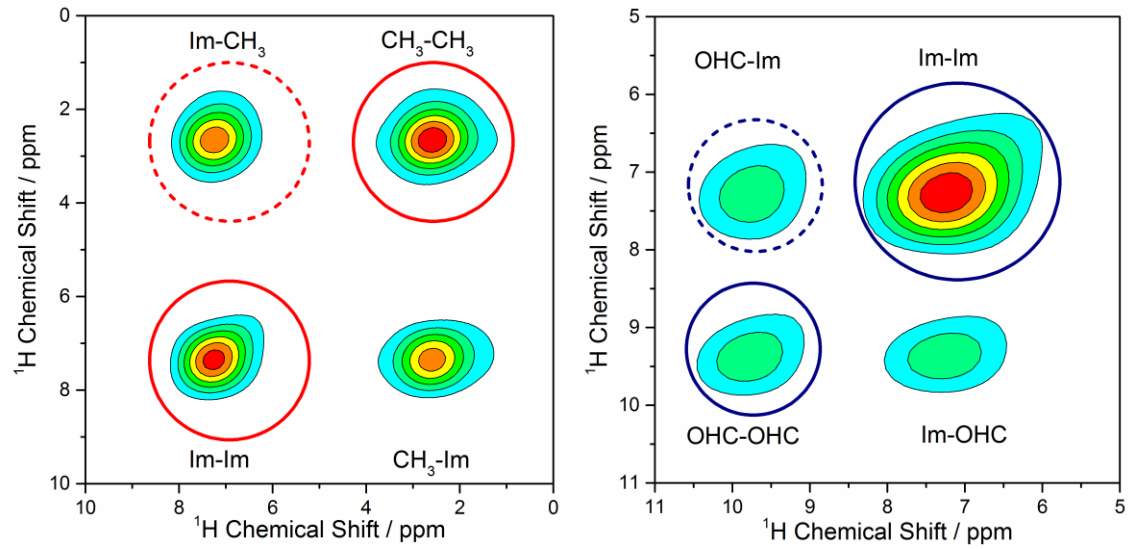

Figure 3.2 ^{1}H-NMR contour plots of **(a)** ZIF-8 and **(b)** ZIF-90, measured at 5 kHz MAS and 1 ms mixing time. Diagonal peaks are marked in solid circles and cross-peaks in dashed circles.

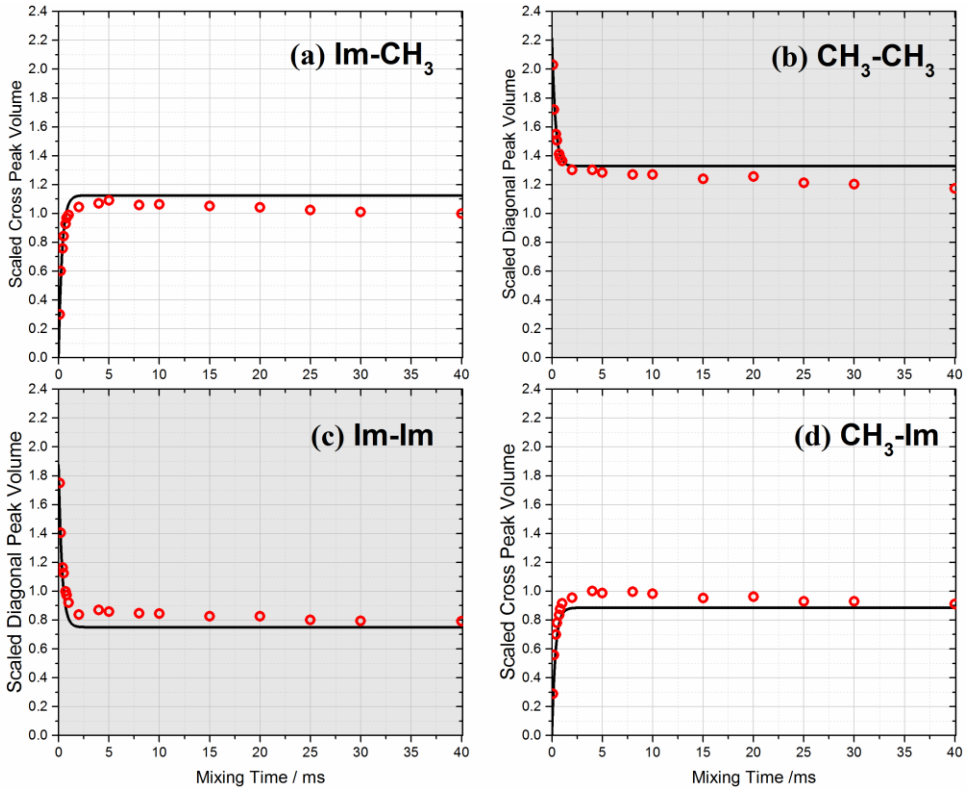

Figure 3.3 Fit of the spin-exchange model (solid curves) to experimental CRAMPS NMR measurements (red circles) for spin exchange between protons in ZIF-8 as a function of the mixing time.

The CRAMPS NMR data from the two pure ZIFs were fitted to the kinetic spin exchange model (Equations A.2-A.8, Appendix A) to determine the single parameter *A* in the spin exchange rate-constant matrix (Equation A.6, Appendix A). Scaled experimental diagonal and cross-peak volumes as a function of mixing time, along with the model fits, are reported for ZIF-8 in Figure 3.3, and the results for ZIF-90 are shown in the Appendix A. The obtained values for ZIF-8 and ZIF-90 are 101.8±5.7 and 120.7±8.1, respectively. The values of initial *z*-magnetization (Equation A.5, Appendix A) for the –Im and $–CH_3$ diagonal peaks were set as the average values from the sum of the diagonal and cross peak volumes (*e.g.*, CH_3-Im + CH_3-CH_3 and Im-Im + Im-CH_3) at mixing times between 2 to 40 ms. While the *A* values for the hybrid (mixed-linker) ZIFs are expected to all be similar based on the end-member ZIFs, for completeness we calculated *A* parameters for each of the mixed-linker ZIFs using a weighted geometric mean based upon the fractions of each type of linker in the mixed-linker material. The three initial *z*-magnetization values for the hybrid materials were set using the same methodology as described above. Only the interatomic distances between the $–CH_3$, -Im, and –OHC hydrogens were changed in the various atomic models based on their different short range order values.

3.4.2 ZIF-8_x-90_{100-x} Hybrid Materials

Figure 3.4a shows the CRAMPS contour plot at 50 ms mixing time from a sample consisting of equal amounts of pure ZIF-8 and pure ZIF-90 crystals mixed physically. As expected, cross-peaks for the methyl-to-imidazole-ring and aldehyde-to-imidazole-ring spin transfers are observed to arise from within the individual ZIF-8 and ZIF-90 phases

since spin transfer occurs over length scales ranging from a few angstroms to tens of nanometers (within the time window of the experiment). However no methyl-to-aldehyde exchange is observed (dashed green circle) which is consistent with the crystal sizes of the ZIF samples being above 100 nm. In contrast, the 2D CRAMPS contour profile for a ZIF-8_{50}-90_{50} sample collected at 1 ms mixing time is shown in Figure 3.4b. Spin transfer between methyl protons and aldehyde protons is clearly observed from the cross-peak at the expected position (dashed red circle).

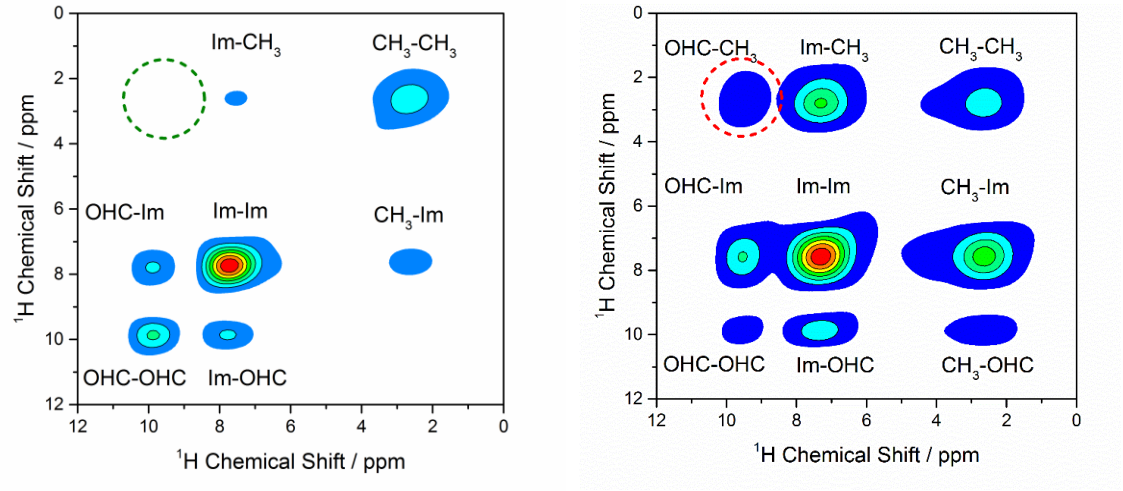

Figure 3.4 ^{1}H-NMR spectra of **(a)** physical mixture of ZIF-8 and ZIF-90 and **(b)** mixed-linker ZIF-8_{50}-90_{50}, measured at 5 kHz MAS and 50 ms mixing time. Green dotted circle in **(a)** denotes the absence of transfer between methyl and aldehyde protons in physical ZIF mixture. Red dotted circle in **(b)** shows the transfer in hybrid material.

Intensity profiles at several mixing times were used to study the spin diffusion and quantify the length scale of these transfer processes. ZIF-8 and ZIF-90 were used for calibration since the distances between the functional group and imidazole ring protons on each linker are known from their crystal structures.[54] Spin diffusion is the spontaneous exchange of spin polarization between nuclear spins, and the rate of this exchange is a function of the domain sizes that comprise the participating nuclei.[130] The intensity, which

is defined as the ratio of the cross-peak area to the cross-peak and source-peak sum, is plotted versus the square root of the mixing time and shown in Figure 3.5a for both ZIF-8 and ZIF-90. Each spin diffusion profile shows an approximately linear increase from 0 – 2 $ms^{1/2}$ followed by a plateau at longer mixing times. The saturation levels of these curves are defined by the relative ratio of protons in the source and the sink, which in this case are the methyl and aldehyde protons, respectively.[56]

For an estimation of the spatial distribution of linkers, one can adopt a Fickian-based spin diffusion approach. A useful feature of this approach is that the domain size(s) of hybrids can be determined simply by the extrapolation of the early time, linear portion of the slope to the x-asymptote when plotted as a function of the square root of time.[133] In this case, the two unknowns are the dimensionality of the domains (spheres, rods, fractals, lamella, etc.) and the spin diffusion coefficient. An alternative technique such as transmission electron microscopy or small angle x-ray diffraction is required to determine the dimensionality of the domains. The spin diffusion coefficient can be estimated via empirical relations or using standards of known length scales of mixing.[56] We estimated the spin diffusion coefficients in the ZIF-8 and ZIF-90 neat materials by inspecting the proton positions in the crystal structures and performing finite element calculations of the spatial polarization changes using a lamellar model of packing of protons for various spin diffusion coefficient values. The best fit values were 0.25 nm^2/ms and 0.2 nm^2/ms for ZIF-8 and ZIF-90, respectively, which is on the lower end of reported ^1H spin diffusion coefficients (0.05 to 0.8 nm^2/ms) and is likely due to proton diluteness compared to typical polymers.[57, 134]

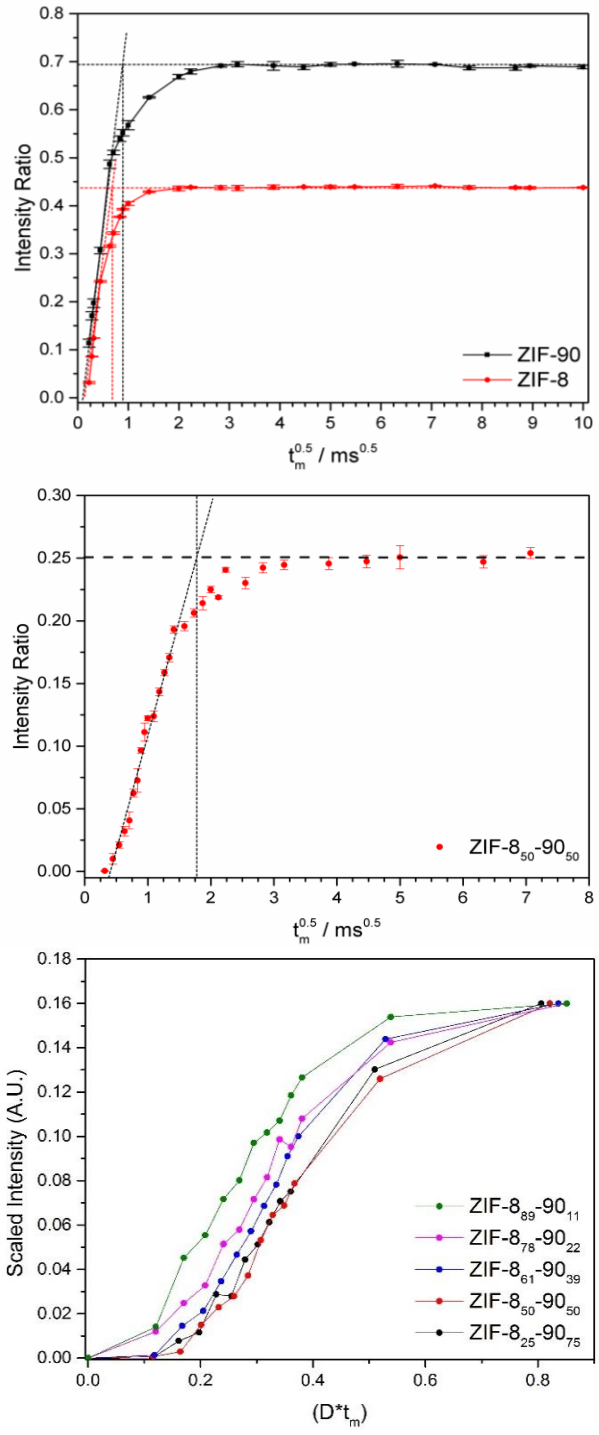

Figure 3.5. Spin diffusion profiles of (a) ZIF-8 and ZIF-90, (b) ZIF-8_{50}-90_{50}, and (c) ZIF-8-90 at various compositions scaled by the anticipated spin diffusion coefficient.

An alternative way for determining the spin diffusion coefficient *D* was introduced by White et al.[57] as represented by:

$$D = \frac{\pi x^2}{4\varepsilon\tau_{eq}} \tag{3}$$

where *x* is the distance of the defined irreducible unit or domain as measured from the crystal structure, ε is the dimensionality of spin transfer, and τ_{eq} is the observed magnetization equilibration time. For intramolecular spin diffusion the characteristic dimension <*x*> of the domain was estimated using:

$$< x >= (L \times d)^{0.5} \tag{4}$$

where *L* is the length and *d* is the diameter of the domain. For ZIF-8 and ZIF-90, *x* was estimated at 0.35 nm and 0.34 nm respectively from the crystallographic structures. τ_{eq} was evaluated by extrapolating the linear region of the spin diffusion curve to the saturation level as shown in Figure 3.5a, and was found to be 0.43 ms for ZIF-8 and 0.74 ms for ZIF-90. The values of $D_{ZIF\text{-}8}$ and $D_{ZIF\text{-}90}$ obtained using these parameters and equation 3 are 0.2 nm^2/ms and 0.1 nm^2/ms, respectively.

Figure 3.5b shows the spin diffusion plot for a ZIF-8_{50}-90_{50} mixed-linker material. The expected saturation level (at long mixing times) of the spin diffusion curve for this composition is also shown. This can be calculated purely from the bulk composition by taking the ratio of numbers of source and sink protons. For example, in ZIF-8_{50}-90_{50} there are 3 methyl protons for every aldehyde proton and hence the expected saturation ratio was

calculated as 1/(1+3) = 0.25. τ_{eq} was estimated at 3.1 ms by extrapolating the slope to the asymptote. The corresponding value of x calculated using Equation (3) is ≈1 nm; note that the dimensionality (ε) is not known *a priori*. We also compared the spin diffusion data for the multiple compositions of ZIF-8_x-90_{100-x}. Since the spin diffusivity is likely to change (subtly) amongst the samples because of changes in the proton density and (potentially) molecular dynamics, we scaled the spin diffusion data for the multiple compositions by the anticipated spin diffusion coefficient. The spin diffusion coefficients were calculated by either interpolating between the ZIF-8 and ZIF-90 using either a geometric average or by using the second moment of the single pulse excitation spectra (Figures A.6 and A.7, Appendix A) for use in known equations of the spin diffusion coefficient. Both methods yielded similar results. The data is shown in Figure 3.5c, where we have scaled the asymptotes to coincide and have zoomed into the early time points. As shown in the figure, all of the compositions have nearly the same total equilibration time, $(Dt)^{0.5} \approx 0.9$, which suggests that the total repeat units of the domains in ZIF-8_x-90_{100-x} materials are nearly identical at a length scale comparable to their XRD-derived cavity diameters as measured with Zeo++[135] for ZIF-8 (1.14 nm)[17] and ZIF-90 (1.136 nm)[118], and also to the size of their unit cells (1.699 nm and 1.727 nm respectively). Previously, there had been no direct evidence of linker mixing in ZIFs at sub-unit-cell length scales. While previous findings that employed techniques including micro-Raman spectroscopy, photothermal induced resonance (PTIR), and aerosol time-of-flight mass spectrometry (ATOF-MS) for observing spatial uniformity in mixed-linker MOFs have been limited to length scales greater than 100 nm[18], the above NMR spin diffusion measurements conclusively establish that there is

sub-unit-cell linker mixing in these mixed-linker ZIFs. However, in order to delineate further between these structures, we turned to a kinetic exchange model.

The spin equilibration times (scaled by the estimated spin diffusion coefficients) are approximately the same amongst the compositions, which denotes the same total repeat distance in each of the samples. The 50:50 composition exhibits the slowest initial slope, denotes the largest possible domain, and decreases in composition of either of the components only serve to decrease the average cluster size and increase the slope, an observation consistent with previously determined Fickian models. However, we also observe a drastic deviation from the classic Fickian $t^{1/2}$ dependence upon decreasing the ZIF-8 fraction. Chen et al.[136] has shown that local (< 1 nm) spin diffusion coefficients can be slower than those at longer length scales due to non-diffusive, exponential behavior due to discrete exchange events. Here, it seems the time window over which this occurs varies with sample and is likely due to the composition-dependent change in the uniformity of local dipolar fields under MAS. Upon inspection of the single pulse excitation ^{1}H MAS NMR spectra (Appendix A), the ZIF-8-rich materials exhibit only weak MAS sideband intensity, which would suggest a strong network of dipolar coupled protons, little appreciable dipolar field averaging, and more uniform dipolar fields. The ZIF-90-rich hybrids, on the other hand, exhibit NMR spectra with strong sideband intensities with no appreciable underlying broadened features, suggesting significant averaging of weak couplings in the presence of strong couplings and less uniform dipolar fields.

Next we explore the possibility of determining more quantitatively the short-range linker mixing patterns. Several groups have used ^{1}H spin diffusion NMR as a method for predicting proton positions using rates of exchange between neighboring protons using

kinetic equations. We created models of mixed-linker ZIFs that had the same relative linker compositions but different SRO (α) values, *via* methods described in a previous section. The Warren Cowley parameter, used to quantify SRO, is normalized to cover the range from [-1, 1]. A system with an α value of > 0 (< 0) is clustered (ordered). For the periodic systems under consideration, the SRO of clustered structures can asymptotically approach 1 with increasing unit cell size since there will always be an interface between regions containing only linkers of one type. The lower bound (~ -0.29), as determined through our RMC procedure, is observed to be constant for a composition range of 0.21 to 0.79 mole fraction of OHC-Im linkers. This observable lower limit is due to our definition of nearest neighbors as well as the specific topology of our ZIF system. The lower limit on the SRO parameter may not be possible to determine *a priori* for all 3D periodic systems and would need to be determined empirically for specific systems as in the present case. Figure 3.6 shows how the functional group protons (-C**H**$_3$ for ZIF-8 and –C**H**O for ZIF-90) are distributed in space over a 5×5×5 unit-cell volume for ZIF-8_{50}-90_{50} with three different values of α representing clustering, randomization, and significant ordering respectively. While Fickian models of spin diffusion could eliminate such a highly clustered model as shown in Figure 3.6a (SRO = 0.87) as a possibility for the structures here, kinetic models may offer a more precise estimate of varying degrees of randomization and clustering (Figure 3.6b-c). For each overall composition, simulated ^{1}H CRAMPS NMR intensity patterns for the mixed-linker structures with different α values were directly calculated using nearest-neighbor dipolar couplings (see the Appendix A). No fitting parameters are used, since the spin exchange parameter *A* is already known from the calibrations with ZIF-8 and ZIF-90. For example, Figure 3.7 shows the experimentally measured and calculated

peak intensities of ZIF-8_{50}-90_{50} for α= 0.45. The subplots shaded in pink represent NMR spin exchange between methyl protons on the ZIF-8 linker and the aldehyde protons on the ZIF-90 linker, the transfer processes that are of most interest for structure determination; although all the exchange processes are measured and calculated. The agreement between experimental and simulated NMR curves was quantified using MAE (Equation 2), which was used to determine the structure that most closely reproduces the experimental data for each mixed-linker ZIF composition. Specifically, we used the intensity ratio of the cross peak corresponding to the methyl-to-aldehyde (CH_3-CHO) transfer to the sum of the intensities of the methyl diagonal peak (CH_3) and the CH_3-CHO peak (as plotted earlier in Figure 3.5) for assignment of an SRO value. Simulated curves were generated for several structures with identical composition but different short-range-order values.

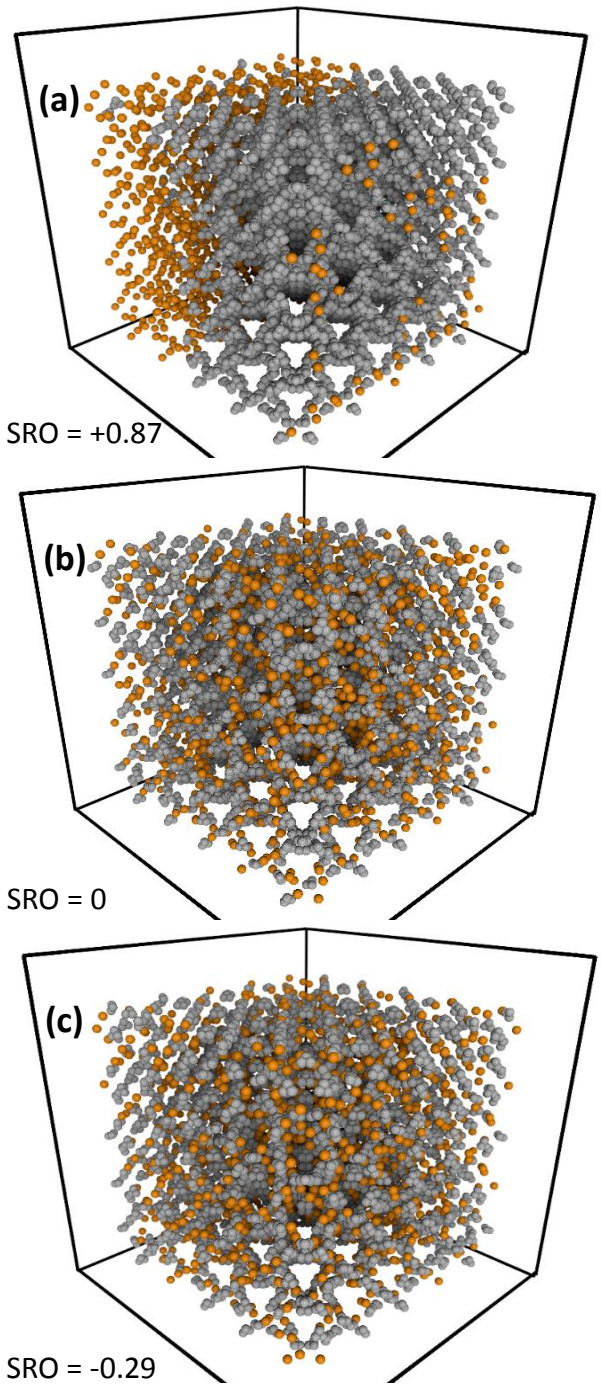

Figure 3.6 ZIF-8_{50}-90_{50} methyl (gray) and aldehyde (orange) hydrogen maps for 5×5×5 supercells of size 8.47 nm: **(a)** SRO of α= 0.87 demonstrating extreme clustering, **(b)** SRO of α= 0.0 demonstrating a random linker arrangement, and **(c)** SRO of α= -0.29 demonstrating partial ordering. Hydrogens not to scale, in order to enhance clarity.

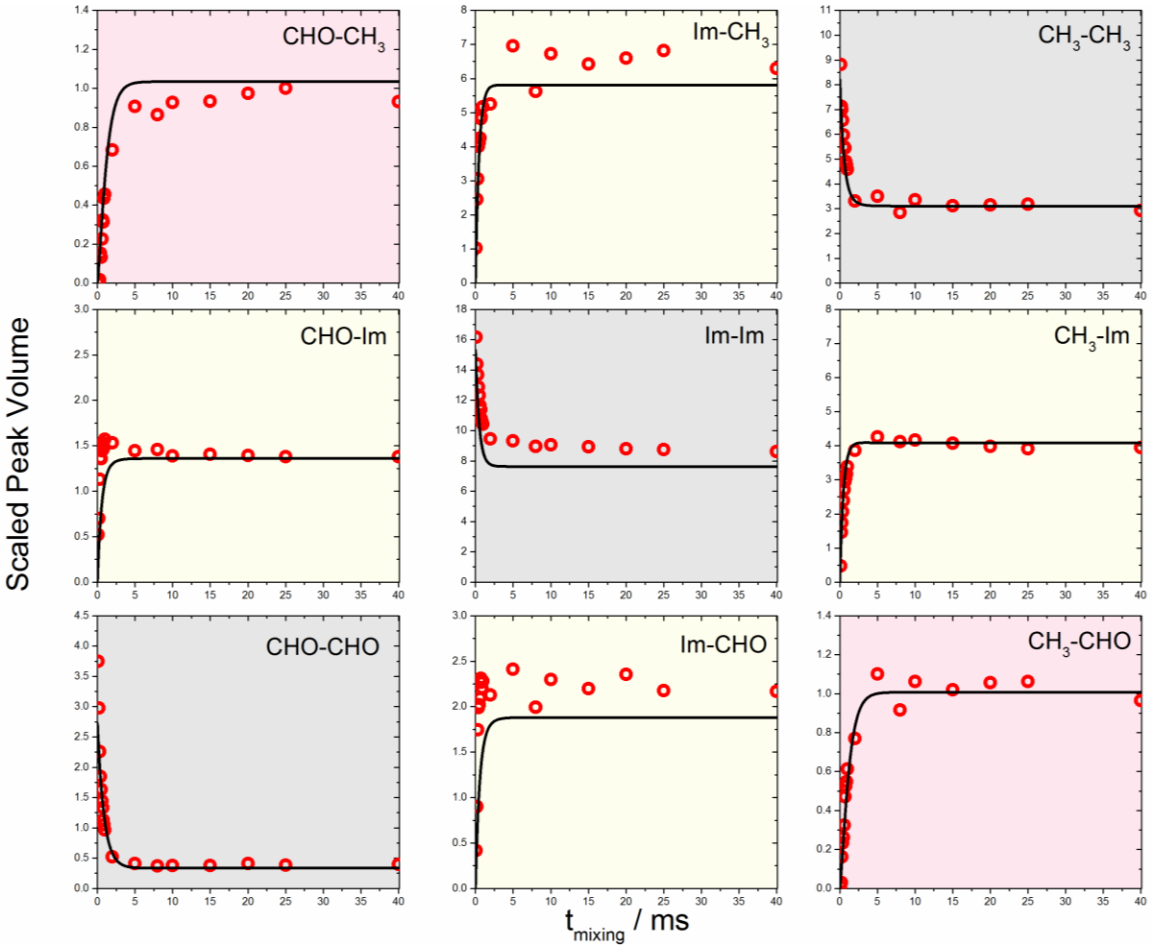

Figure 3.7 Experimental (open red circles) and simulated NMR spin exchange peak intensities for ZIF-8_{50}-90_{50} with α= 0.45.

The comparisons for ZIF-8_{50}-90_{50} are shown in Figure 3.8. The best minimum MAE between experimental and simulated curves for this material is given by the structure with α = 0.45 (Figure A.10, Appendix A). From the definition of α, it follows that the two linkers in ZIF-8_{50}-90_{50} exhibit some tendency for clustering. The value of α = 0.45 indicates that given a methyl linker in ZIF-8_{50}-90_{50}, there is a 28% probability that there is an aldehyde linker present in each of its six nearest neighbor sites. A ±5% deviation was

chosen as the tolerance limit for describing the structure with reasonable accuracy. It was found that structures with $0.40 < \alpha < 0.55$ fell in this range.

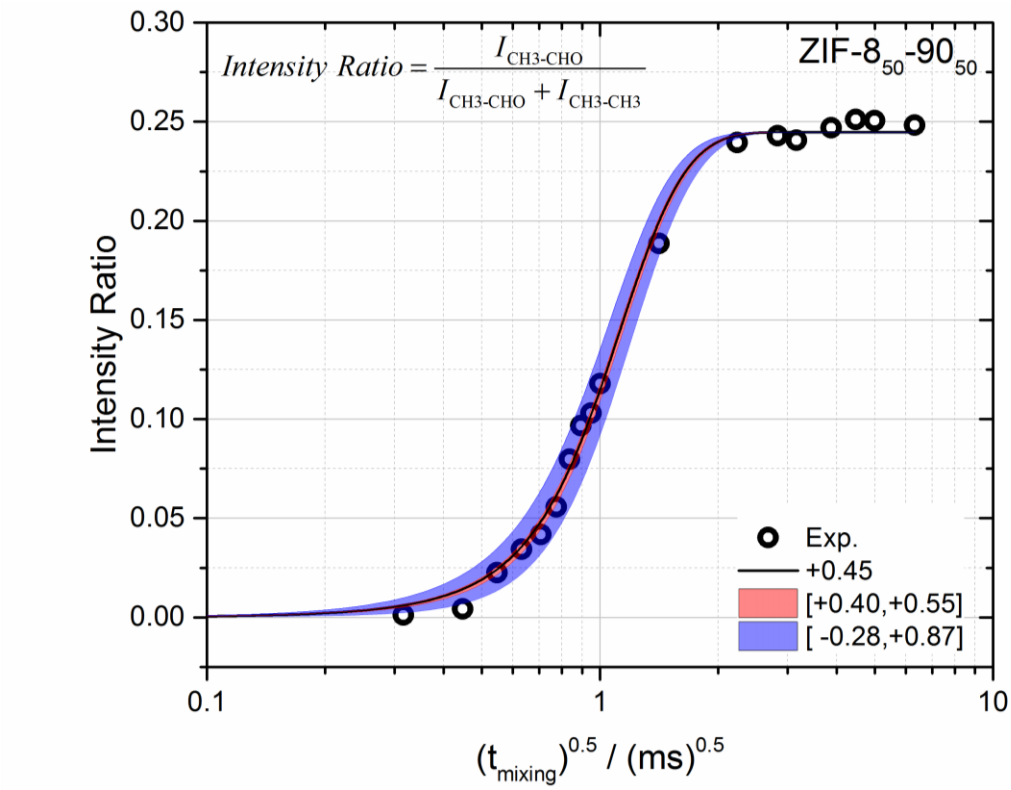

Figure 3.8 Comparison of experimental NMR spin exchange intensity ratios and simulated curves for several structures with different α values for ZIF-8_{50}-90_{50}.

Figure 3.9 shows the best fits of the spin exchange plots for the various compositions of mixed-linker ZIF-8_x-90_{100-x} materials, and Figure A.10 (Appendix A) shows the MAE versus α for each composition. The model yields good fits for ZIF-8_{25}-90_{75}, ZIF-8_{61}-90_{39}, and ZIF-8_{78}-90_{22} yield good fits, but ZIF-8_{89}-90_{11} shows greater deviation. Recall that ZIF-8_{89}-90_{11} yielded a spin diffusion curve with a strong $t^{1/2}$ dependence (Figure 3.5c) and weak spinning sideband intensity at 5 kHz MAS (Appendix A), suggesting the strongest network of dipolar couplings of the ZIF-8_x-90_{100-x} compositions. Since the kinetic exchange model is based solely on direct couplings and

ignores multiple quantum, molecular dynamics, and MAS effects, we therefore posit that the model is most accurate when studying sample sets with less appreciable variation in the local proton density and/or dynamics.

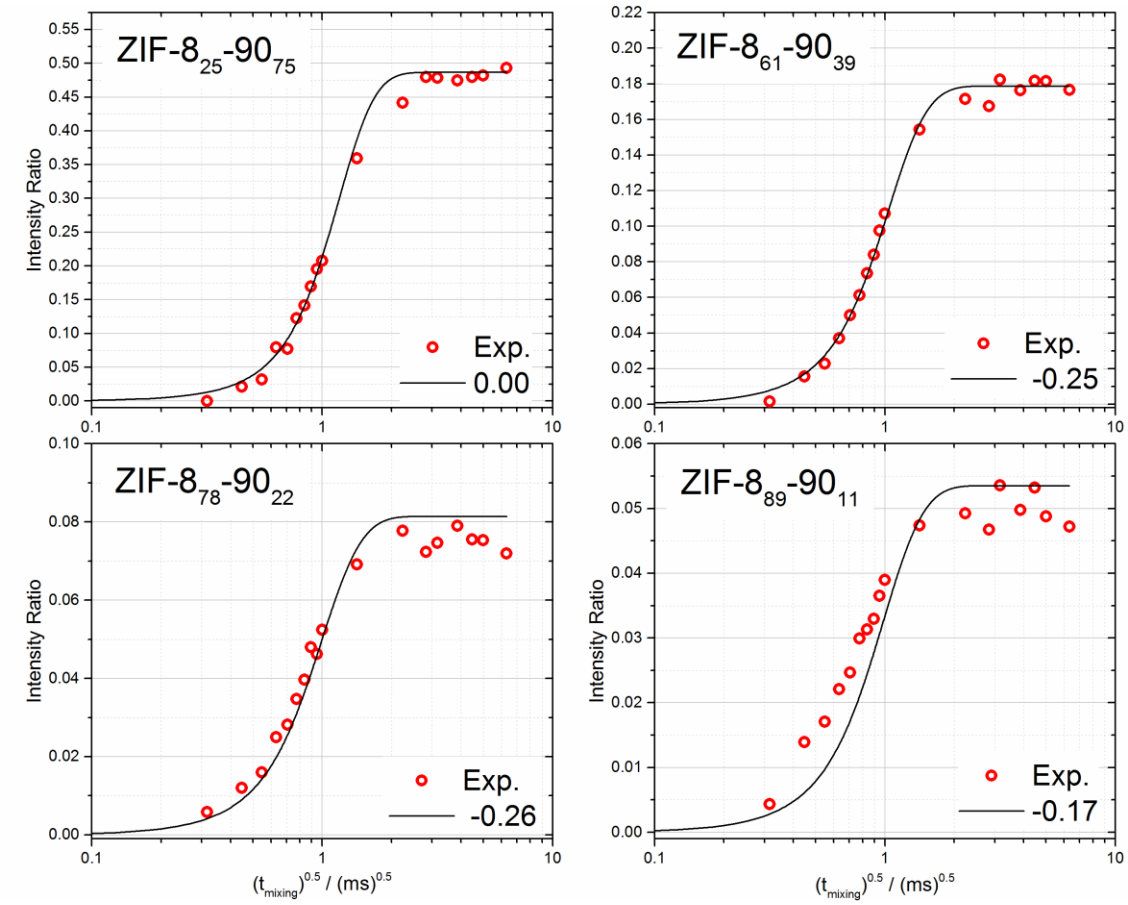

Figure 3.9 Comparison of experimental (red circles) and simulated 2D CRAMPS peak ratios of the 'best-fit' SRO models (solid black lines), for four different ZIF-8-90 mixed-linker materials.

For the compositions that the model is most successful, it was observed that the best-fit α value falls in the range that indicated a close to randomly distributed structure, with the exception of ZIF-8$_{50}$-90$_{50}$. This is represented graphically in Figure 3.10 in relation to the 'nearest neighbor' concept. The anomalous behavior of ZIF-8$_{50}$-90$_{50}$ is not clearly understood at this point. It must be noted that this material certainly shows linker mixing

at a unit-cell level and has long-range compositional homogeneity. The variation in α is directly translated to a slightly higher tendency for pore windows to have exclusively ZIF-8 or ZIF-90 linkers (see below). Even though individual windows have different compositions, there are multiple windows of each type within each unit cell and at length-scales higher than that of each unit cell, the compositional homogeneity is preserved. We can offer the hypothesis that when both linkers are present in roughly equal amounts, there may be an increased thermodynamic or kinetic driving force that tends towards cluster formation during synthesis. On the other hand, when one linker is in the minority, it may prefer to be more randomly distributed within the 'matrix' of the majority linker. Experimentally, it has been observed that the rate of formation of ZIF-8_x-90_{100-x} goes from slow (observable product formation in a duration of many minutes) to fast (nearly instantaneous) as the relative content of the OHC-Im linker is increased from 0 to 100%. The observed deviation from near-random mixing of ZIF-8_{50}-90_{50} could be attributed to competing effects of heats-of-mixing and the reaction kinetics. Although uncommon, such deviations from the expected value of order parameter for binary materials are known. For example, an almost-equiatomic Pd-Pt alloy was shown (*via* X-ray scattering measurements) to exhibit a more ordered behavior than what was expected based on phase transition thermodynamics.[137]

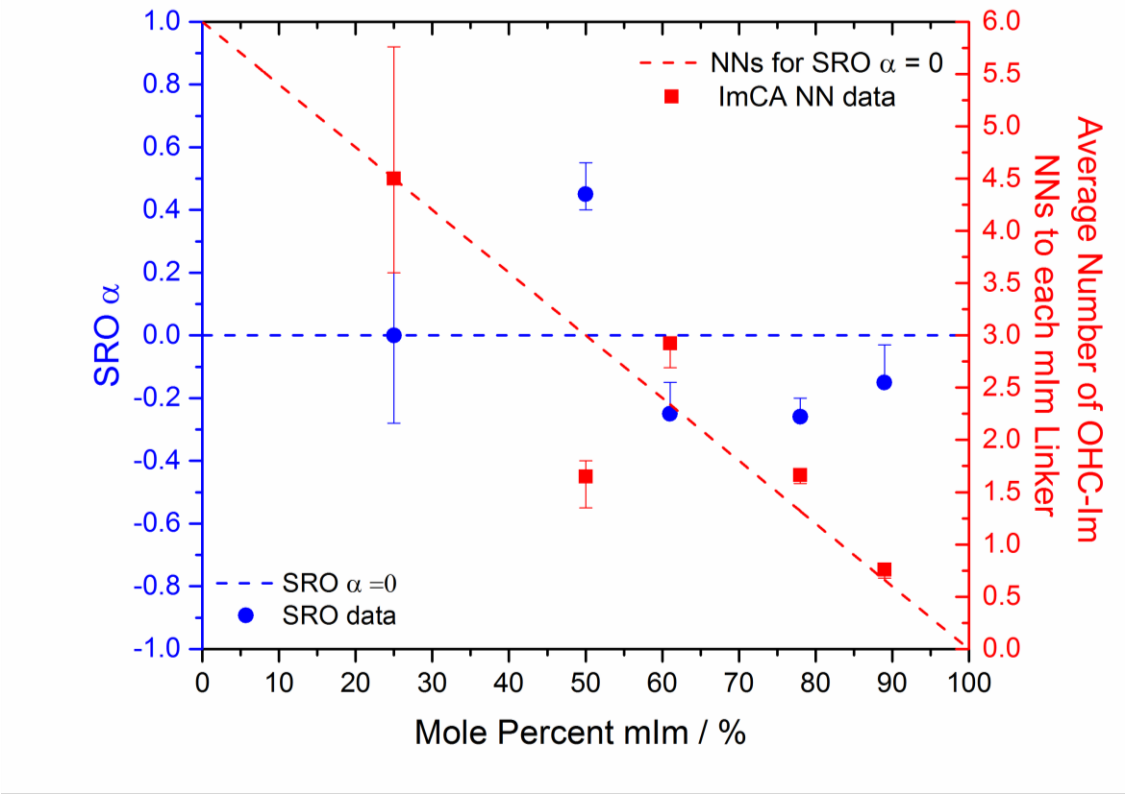

Figure 3.10 Short range order α and average number of OHC-Im linkers per mIm linker as a function of the overall composition of the mixed-linker ZIF-8-90 material.

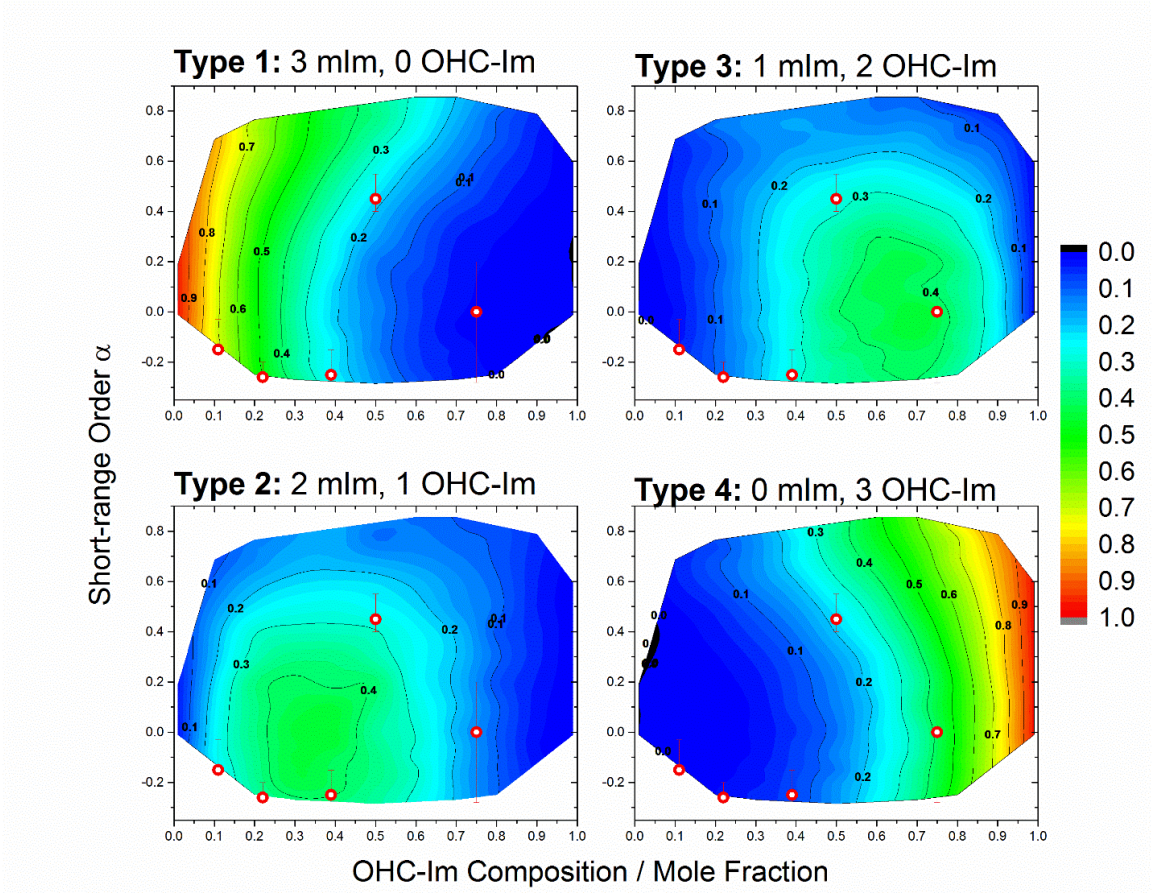

Figure 3.11 Probability distributions of observing the four possible types of pore windows as a function of the short range order parameter (α) and the overall composition of the mixed-linker ZIF-8-90 material. Red circles indicate the window type probabilities for the experimental samples.

It has been clearly shown that hybrid cage-type ZIF-8-90 materials allow for drastic tunability of molecular diffusion[104], implying that diffusion is primarily influenced by the three imidazolate linkers lining the pore windows between cages. These windows can be classified into 4 types: Type 1 (lined by 3 mIm linkers), Type 2 (2 mIm linkers and 1 OHC-Im linker), Type 3 (1 mIm linker and 2 OHC-Im linkers), and Type 4 (3 OHC-Im linkers). The various structure models generated with different compositions and short-range orders can then be differentiated according to the probability distribution of these windows in the structure. A set of 166 unique 5x5x5 supercells were generated to represent the entire

composition and accessible SRO parameter ranges to provide a qualitative understanding of the effect of SRO on window type probability. The probability of window types was determined in a two-step method. A depth-first search (DFS) algorithm was applied that identified cycles of size N (i.e. all 6 member rings) in an undirected graph (i.e. SOD topology with Zn centers as nodes and linkers as edges). Once all the 6 member rings were identified and the mIm/OHC-Im linkers had been assigned according to the RMC procedure described above, an assignment algorithm identifies which three linkers (i.e. those with imidazole ring hydrogens in the plane of the window) belong to each 6 member ring window. The type of these three linkers determines the window type. No energetic parameters were taken into account for this analysis. Figure 3.11 shows four contour plots representing the fractional probabilities of observing each of the four window types for a structure with a given composition and short-range order. For example, structures with positive SROs (*i.e.*, more clustered linkers) demonstrate lower probabilities of observing Type 2 and Type 3 windows. The locations of the five experimentally studied hybrid materials are shown by the red circles in each plot. The ZIF-8_{50}-90_{50} structure has very similar window probability profiles whether the linkers are clustered (+0.45) or alternating (-0.25). While outside the scope of the present study, the above method of differentiating the structural models based on window type distributions could be used to qualitatively predict the influence of SRO on diffusion properties.

3.5 Conclusions

The unit-cell-level mixing of linkers in mixed-linker ZIFs (specifically ZIF-8-90) using a combination of ^{1}H CRAMPS NMR spectroscopy and computational techniques was demonstrated in this chapter. Direct experimental observations of linker mixing were

accomplished by measuring the spin diffusion behavior between functional groups on the linkers. The experimental data was then compared to simulations based on a spin exchange model and proton positions from computationally generated mixed-linker ZIF structure models that use the short-range order (SRO) parameter as a measure of the ordering, clustering, or randomization of the linkers. The present method offers the advantages of not requiring isotope enrichment as well as a potentially reasonable way of predicting how subtle changes in structure can affect the pore/window-type distribution in mixed-linker materials. Our findings undeniably indicate that the linkers in ZIF-8-90 hybrids are mixed on the sub-unit cell length scale, and provide conclusive evidence that the synthesis of these mixed-linker ZIFs results in true hybrid materials as opposed to separated or clustered phases within the same crystal. When using the kinetic spin exchange model, we find that the mixed-linker ZIFs exhibit slightly different levels of linker mixing depending on the bulk composition. Furthermore, structures close to equimolar composition of the two linkers appear to have greater tendency for linker clustering than those with a majority content of one linker. Using the mixed-linker ZIF structures determined by the NMR experiments and modeling, we have also shown how the window-type distribution in experimentally synthesized mixed-linker ZIF-8-90 materials varies as a function of their composition. The above structural information can be further used for predicting, screening, or understanding the tunable adsorption and diffusion behavior of mixed-linker ZIFs. This technique can be potentially applied to any MOF system with linker functional groups containing protons that are distinguishable by NMR and topologies known *a priori* through crystallographic techniques.

In the next chapter, we demonstrate that this method can be combined with other existing characterization techniques as a ‘quick check’ method to ascertain linker segregation/distribution in mixed-linker materials synthesized via alternate routes such as Solvent Assisted Linker Exchange (SALE). The full kinetic rate model treatment is not necessary if the structures resulting from different syntheses have sufficiently distinct linker distribution patterns. In addition to providing highly accurate structures for computational screening and prediction capabilities for mixed-linker structures, we show that this method will also aid in the selection of the appropriate synthesis route to make these materials.

CHAPTER 4. STRUCTURAL AND MECHANISTIC DIFFERENCES IN MIXED-LINKER ZIFS MADE VIA DIFFERENT ROUTES

4.1 Introduction

An attractive feature of MOFs as compared to other nanoporous materials such as zeolites, is their relative ease of synthesis, often through solvothermal routes without any templating or structure-directing agents. MOFs are also amenable to post-synthetic modification and functionalization, making it possible to obtain structures that are difficult to realize *de novo*.[41, 66, 138-139] It is possible to post-synthetically replace linker molecules and incorporate other linkers into MOFs using Solvent Assisted Linker Exchange (SALE) or Solvent Assisted Linker Incorporation (SALI) routes.[65, 68-70, 140-142] SALE has been demonstrated in several MOF systems such as the MIL-series, UiO-series and PPF-series (all with carboxylate-based linkers) as well as the ZIF and CdIF series (imidazole-based linkers).[70]

Although a number of interesting demonstrations of SALE and *de novo* mixed-linker MOF synthesis have been reported, there is no systematic understanding of structural and mechanistic differences between the two techniques that lead to important functional differences between the two types of materials. The differences in linker distribution between SALE and de novo mixed-linker MOFs could create substantial differences in their properties, but these differences are not well characterized. Furthermore, while *de novo* synthesis can be understood by a relatively straightforward mechanism involving

incorporation of different types of linkers during crystallization, the SALE mechanism has not been investigated in detail and there is no overarching mechanism proposed that can explain how different MOF materials respond to SALE. Key aspects of SALE, including the role of solvents and the mechanisms of exchange (single-crystal to single-crystal versus dissolution-and-recrystallization), are not well understood.[70] MOFs with the same/similar linkers but different metal centers can display extremely different responses to SALE. For example, MIL-53 and MIL-68 MOFs (containing aluminum/indium centers) can be easily modified *via* post-synthetic exchange, whereas MIL-101 (chromium centers) is inert to exchange.[66]

In the context of the above issues, there are two main elements of this work. First, we investigate how mixed-linker/hybrid ZIF materials synthesized through both the SALE route and *de novo* routes have considerably different linker distributions and properties even when their bulk compositions are the same. This study focuses on the ZIF-8-90 series of mixed-linker ZIFs, which is particularly interesting because ZIF-8 and ZIF-90 are isoreticular (cubic SOD topology) and the hybrids are known to maintain the same topology throughout the entire mixed-linker composition range.[40] We synthesize a family of ZIF-8-90 hybrids using both the above routes, and characterize their differences at multiple length scales. We use their water and nitrogen adsorption behavior to understand differences in their macroscopic properties. We study their microscopic structural heterogeneity using 2D ^{1}H-NMR measurements, and present a technique to compare the degree of linker mixing between different types of hybrid ZIFs/MOFs (e.g., synthesized by SALE versus *de novo*). Secondly, we conduct a detailed mechanistic study of ZIF-8→ZIF-90 SALE, and obtain insights into the propagation of SALE reactions by controlling the

crystal size and temperature and using solution-NMR to monitor the process as a function of time. We also show that fluorescent confocal microscopy can be very useful to directly monitor the linker exchange process and the distribution of linkers over entire crystals. We then combine the detailed information obtained to propose a mechanism for the SALE process in ZIFs.

4.2 Experimental Methods

Materials. Zinc nitrate hexahydrate (Alfa Aesar), 2-methylimidazole (2-MeIm) and 1-methylimidazole (1-MeIm) (Sigma Aldrich), imidazole-2-carboxaldehyde (OHC-Im), sodium formate (Alfa Aesar) and methanol (EMD) were used as received.

Synthesis of ZIF-8 nanocrystals. ZIF-8 nanocrystals were synthesized *via* the procedure given by Cravillon et al.[143] Specifically, 2.933 g $Zn(NO_3)_2.6H_2O$ was dissolved in 200 mL methanol. Separately, 6.489 g 2-MeIm was dissolved in 200 mL methanol. The first solution was rapidly poured into the second solution while stirring with a magnetic bar. The mixture turned turbid slowly and the stirring was stopped after 1 hour. The nanocrystals were collected by centrifugation at 8500 rpm for 20 minutes, washed with methanol, and finally re-dispersed in methanol to form a suspension. Small portions of this suspension were dried and degassed separately for characterization purposes.

Synthesis of ZIF-8 microcrystals. ZIF-8 microcrystals were synthesized by modifying the procedure given by Zhang et al.[144] Here, 0.734 $Zn(NO_3)_2.6H_2O$ was dissolved in 50 mL methanol, whereas 0.810 g 2-MeIm and 0.810 g 1-MeIm were dissolved in another 50 mL methanol. The first solution was poured into the second solution while stirring with a magnetic bar. Stirring was stopped upon mixing of both

solutions and the stirrer bar was removed. The mixture was sealed with Parafilm and left undisturbed overnight. Crystals were collected, washed with fresh methanol thrice, air-dried at 60° C, and then degassed at 180° C for 24 hours in a vacuum oven.

Synthesis of ZIF-8 macrocrystals (> 100 µm size). Large ZIF-8 macrocrystals were synthesized by using the following procedure. 1.764 g $Zn(NO_3)_2.6H_2O$ was dissolved in 20 mL methanol. 0.973 g 2-MeIm and 0.404 g sodium formate were dissolved in 20 mL methanol. The two solutions were mixed and transferred into a Teflon liner. A glass slide was also inserted into the liner. The liner was then sealed inside a Parr stainless-steel reactor and incubated in an oven at 90° C for 6 hours. The reactor was cooled slowly to room temperature under ambient conditions. Crystals were collected from the sides of the glass slide and washed with methanol thrice.

De novo synthesis of mixed-linker ZIF-8-90 crystals. Mixed-linker ZIF-8_x-90_{100-x} crystals (where *x* and 100-*x* are the percentages of ZIF-8 and ZIF-90 linkers in the crystal) were synthesized by the Non-Solvent Induced Crystallization (NSIC) procedure of Thompson et al.[40, 144] ZIF-8_{55}-90_{45} was synthesized as follows. 2.974 g $ZnNO_3.6H_2O$ was dissolved in 100 mL methanol. 2.882 g 2-MeIm, 0.470 g OHC-Im and 2.72 g sodium formate were dissolved in 100 mL methanol by heating to 60° C. After cooling the linker solution to room temperature, the zinc salt solution was poured into it rapidly with stirring. The stirring was stopped after 1 hour and crystals were recovered by centrifugation and washed thrice with fresh methanol. The crystals were then air dried at 60° C and degassed at 180° C in vacuum. To synthesize ZIF-8_{50}-90_{50}, the same procedure was used with 2-MeIm and OHC-Im masses of 2.874 g and 0.480 g respectively.

De novo synthesis of mixed-linker ZIF-8-90 macrocrystals (> 100 µm size). Large mixed-linker ZIF-8_{75}-90_{25} crystals were synthesized using the following procedure. 0.595 g $Zn(NO_3)_2.6H_2O$ was dissolved in 40 mL methanol. 0.571 g 2-MeIm, 0.099 g OHC-Im and 0.544 g sodium formate were dissolved in 40 mL methanol by heating to 60° C. This solution was allowed to cool down to room temperature. Both solutions were then mixed and sealed in a glass jar. The jar was then heated to 90° C in an oil bath for 24 hours. Crystals were collected from the side of the jar and washed with fresh methanol thrice.

Solvent Assisted Linker Exchange (SALE). To perform SALE on ZIF-8 nanocrystals, 0.961 g OHC-Im was dissolved in 50 mL methanol at 60° C under stirring. After cooling this solution to room temperature, 40 mL of ZIF-8 nanocrystals suspended in methanol was added. The two solutions were mixed thoroughly using low-intensity ultrasonication using a VWR ultrasonication water bath, operating at 120 W and 40 kHz. The resulting mixture was then sealed and kept in an oven at 60 °C or 90 °C for durations of 4-192 hours. To perform SALE on ZIF-8 microcrystals and macrocrystals, 0.480 g of OHC-Im was dissolved in 40 mL methanol by heating to 60 °C under stirring. This solution was transferred to a Teflon liner and 60 mg of ZIF-8 microcrystals were dispersed in it. The mixture was then sealed in a Parr stainless-steel reactor with a Teflon insert, and kept in an oven at 60° C or 90° C for durations of 4-288 hours. The crystals were then recovered by centrifugation, washed in methanol repeatedly to remove unreacted linkers, air-dried at 60° C, and degassed at 180° C under vacuum.

Characterization. X-Ray Diffraction (XRD) measurements were performed on powder samples using an X'Pert Pro PANalytical diffractometer (CuKα source, λ = 0.1.541 nm) over a 2□ range of 3-45°, with powder samples being dispersed on a low-background

sample holder. Scanning Electron Microscopy (SEM) images were collected on a Hitachi SU8010 field emission microscope operating at 3 kV. Water adsorption isotherms were collected on a TA Instruments VTI Vapor Sorption Analyzer. Nitrogen physisorption isotherms were collected at 77 K using a Microtrac Belsorp-Max analyzer. Composition analysis of the hybrid ZIFs were carried out using a Bruker Avance III 400 MHz solution-state Nuclear Magnetic Resonance (NMR) spectrometer after dissolving the ZIF in deuterated (d_4)-acetic acid. ICP-MS analysis of the post-SALE supernatant solution was performed using a PerkinElmer NexION 300Q ICP-MS with a PerkinElmer multi-element calibration standard 3 (without mercury). As described in detail by us recently[145], spin diffusion (2D CRAMPS) data was collected using a Bruker Avance III 400 MHz solid-state NMR spectrometer with a standard broadband H/X MAS probe. About 5 mg of sample was loaded into a ZrO_2 rotor and the Magic Angle Spinning (MAS) speed was set at 5 kHz. No recoupling was applied during the mixing time. Phase Modulated Lee-Goldburg (PMLG) decoupling was used during the evolution and detection times (Bruker pulse sequence: wpmlg2d).[114-115] We used mixing times from 0.1-50 ms, 399.92 MHz Larmor frequency, 2.5 μs π/2 pulse width, 56.57 kHz frequency offset, 12.5 μs Lee-Goldburg 2π pulse, receiver gain of 8, 4 scans, and 512×128 2D points with sine apodization. Confocal microscopy was performed on a combination Zeiss LSM 780/PS.1 super-resolution microscope equipped with a standard photomultiplier tube, 32-channel spectral GaAsP detector, and a cooled GaAsP detector.

4.3 Results and Discussion

We first performed SALE experiments on ZIF-8 nanocrystals (35±5 nm average size) and microcrystals (bimodal size distribution with 1±0.4 μm and 2.5±0.3 μm

populations). Figure 4.1 shows photographs of the different ZIF materials studied. Before SALE was initiated, both types of ZIF-8 crystals were colorless (Figure 4.1a and 1b). Upon addition of the OHC-Im (ZIF-90) linker solution to the nanocrystal ZIF-8 suspension, both types of crystals rapidly change color to a pale brown tint (Figure 4.1d-1g). Upon visual inspection, the color of the crystals after short (~4 h) and long (up to 6 days) SALE durations were virtually indistinguishable. In contrast, crystals of hybrid ZIF-8-90 materials synthesized *via* the NSIC route (Figure 4.1c) possess an off-white shade, which becomes darker with increasing amount of the ZIF-90 linker in the crystal. Neat 2-MeIm crystals are colorless whereas OHC-Im crystals are pale yellowish-brown. The appearance of color in ZIF-8 crystals undergoing SALE with ZIF-90 linkers suggests that the surface 2-MeIm linkers on ZIF-8 crystals have been exchanged with OHC-Im. The dissimilar visual appearance of NSIC and SALE hybrid ZIF-8-90 materials, even after long exchange times, points to significant differences in microscopic linker mixing levels in the two types of materials.

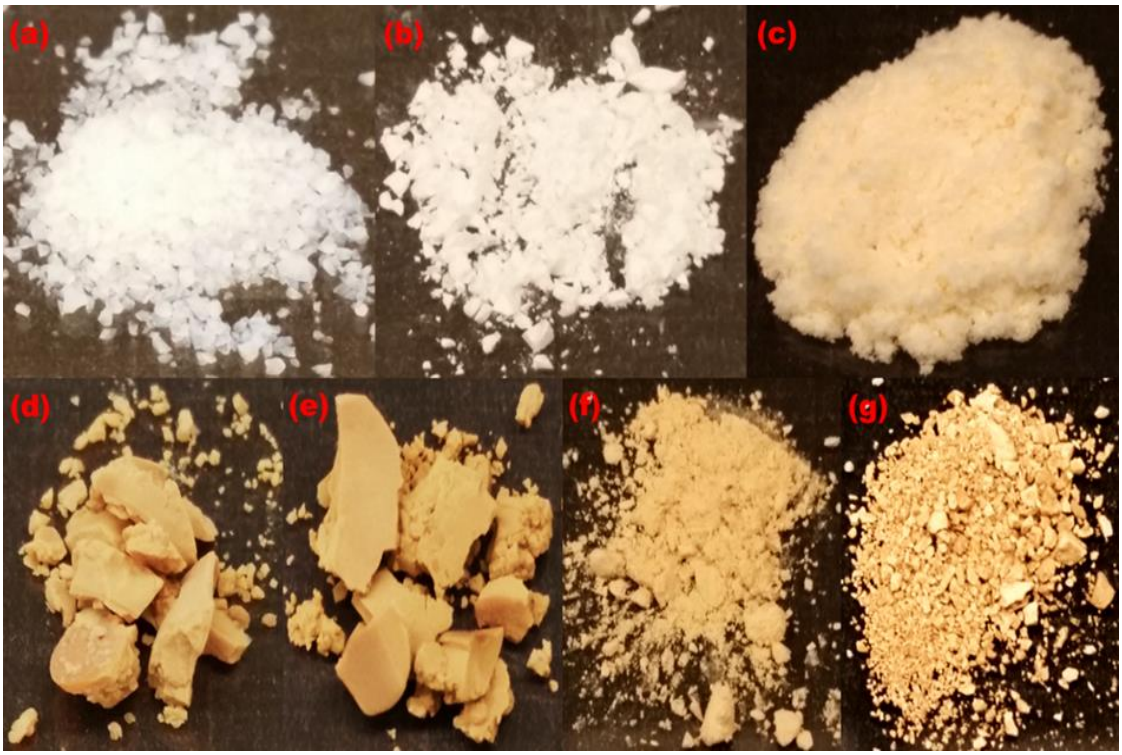

Figure 4.1. (a) ZIF-8 nanocrystals, (b) ZIF-8 microcrystals, (c) ZIF-8_{50}-90_{50} NSIC hybrid, (d) Nano ZIF-8-90 SALE hybrid made at 60° C for 3 days, (e) Nano ZIF-8-90 SALE hybrid made at 90° C for 8 hr, (f) Micro ZIF-8-90 SALE hybrid made at 90° C for 3 days, (g) Micro ZIF-8-90 SALE hybrid made at 60° C for 6 days. Each image occupies roughly 2.5×2.5 cm^2 area.

To study the linker distribution, two SALE-processed samples (one nanocrystalline and one microcrystalline) were prepared with the same overall composition of ZIF-8_{50}-90_{50} (determined by ^{1}H-solution NMR). An NSIC ZIF-8_{50}-90_{50} hybrid was also synthesized for comparison. Figure 4.2 shows XRD patterns of ZIF-8, ZIF-90, the NSIC hybrid, and the SALE hybrids. It is clear that regardless of the linker composition or synthesis route, all members of the ZIF-8-90 family maintain the same SOD topology with near-identical peak positions and intensities. It is not possible to distinguish linker distribution heterogeneity from XRD patterns.

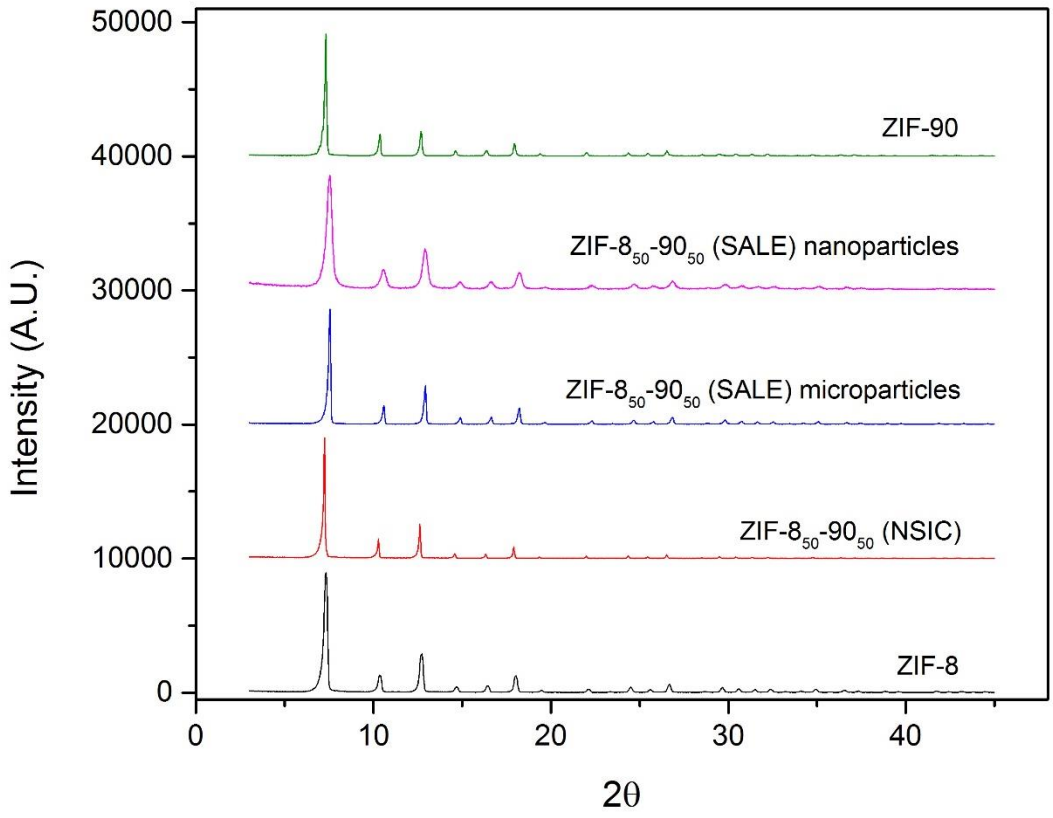

Figure 4.2. Powder XRD patterns of ZIF-8, ZIF-90, NSIC hybrid, and SALE hybrids. The patterns are stacked vertically for convenience of display.

Solid-state NMR spectroscopy has been used recently to study linker mixing patterns in mixed-linker MOF systems.[62-63] For example, we used a combination of ^{1}H-CRAMPS NMR and computational generation of candidate structures to probe the degree of linker mixing in *de novo* ZIF-8-90 NSIC hybrids.[145] This technique is based upon measuring spin exchange between protons on the linker functional groups (-CH_3 and –CHO in ZIF-8 and ZIF-90 respectively). Spin exchange in ZIF crystals is governed by dipolar coupling, whose strength is a strong function of the distance between the nuclei involved. Thus, the rate of spin transfer is dependent upon the degree to which the two linkers are mixed/interspersed in the crystal. Experimentally, we measure the magnetization ratios of the source and sink protons participating in spin transfer (in this case, the 2-MeIm methyl protons and the

OHC-Im aldehyde protons respectively). By monitoring the degree of spin exchange as a function of mixing time, and comparing to kinetic model predictions of spin exchange in computationally generated candidate structures, we showed that the linkers in *de novo* ZIF-8-90 hybrids are mixed at a unit cell-level and can be characterized using the Warren-Cowley short-range order (SRO) parameter.[113, 145]

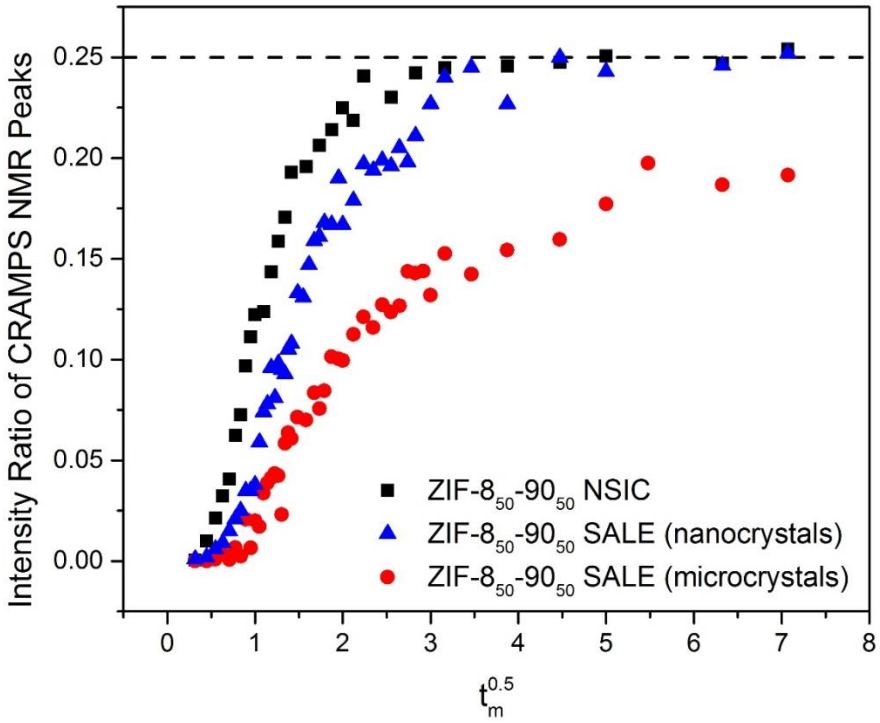

Figure 4.3. ^{1}H CRAMPS NMR peak intensity ratio plotted versus the square root of mixing time (in units of $ms^{0.5}$) for three different types of ZIF-8-90 hybrids of identical overall composition.

Figure 4.3 shows the differences in spin exchange profiles between the SALE and *de novo* (NSIC) hybrids. For qualitative understanding of spin exchange processes in materials, one can use a widely-applied model that approximates the microscopic spin exchange between discrete, homogeneously distributed nuclei as a Fickian 'spin diffusion' process.[56-59] Accordingly, the intensity ratio of the sink and source signals is plotted as a

function of the square root of mixing time (in $ms^{0.5}$) in Figure 4.3. The key aspects to note are the spin diffusion behavior at short mixing times (< 1 $ms^{0.5}$) and at long mixing times (> 4 $ms^{0.5}$). The NSIC hybrid shows a linear increase in spin transfer at short mixing times, consistent with Fickian behavior expected when the linkers are well-mixed. As shown in our previous work[43], the effective Fickian 'spin diffusivity' in ZIF-8 and ZIF-90 is ~2 $nm^2.ms^{-1}$. This leads to a mixing length scale of ~2 nm for the NSIC hybrids based upon the slope of the linear region. Thus it is clear that the linkers are mixed on a unit-cell level. Finer details of the linker distribution were previously characterized in terms of the SRO parameter using a full kinetic model of the spin exchange between the discrete nuclei.[43] On the other hand, the SALE hybrids exhibit a significant lag period before appreciable spin exchange is observed, as well as a slower spin transfer rate than the NSIC hybrids. This suggests that the two spin domains (the methyl group and aldehyde group) in the SALE hybrid are more clustered than in the NSIC materials. The initial lack of spin exchange signal is due to the weak proton-proton dipolar coupling resulting from the much longer distances between 2-MeIm and OHC-Im in the SALE hybrids. In clustered structures, the only spins that can participate in spin exchange at short mixing times are those at the interfaces of the two types of domains, which represent only a small fraction of the total number of linkers in the material.

For the NSIC hybrid, the asymptotic value of the intensity ratio curve at long mixing times can be predicted *a priori* (as marked by the dashed line in Figure 4.3) based on the relative numbers of the two types of protons. The experimental data is seen to reach this asymptotic value (which is 0.25 for a ZIF-8_{50}-90_{50} hybrid). In the nanocrystal SALE hybrid, spin exchange proceeds more slowly than the NSIC hybrid but reaches the

asymptote at a longer mixing time. In the microcrystal SALE hybrid, the spin transfer does not reach the asymptote even at very long mixing times. The nanocrystals have a much larger surface area-to-volume ratio (about 100 times that of the microcrystals), and as a result the interfaces between the two spin domains contribute significantly more to the signal than in the microcrystals. Overall, the spin diffusion measurements allow a way to qualitatively assess whether the linkers in a hybrid MOF/ZIF are microscopically mixed or not, with a resolution approaching unit cell dimensions. In particular, we find that the present SALE materials are not in fact well-mixed hybrid ZIFs but rather display considerable segregation/clustering of the linkers.

Figure 4.4 shows water adsorption and nitrogen physisorption isotherms for pure ZIF-8 and ZIF-90, a physical mixture of ZIF-8 and ZIF-90 crystals, and the ZIF-8-90 hybrids made by both SALE and NSIC. In Figure 4.4a-4b, the physical mixture exhibits adsorption properties that are a simple weighted sum of the properties of ZIF-8 and ZIF-90, as expected. The NSIC hybrid ZIF-8-90 material displays distinct adsorption behavior from the "parent" ZIF-8 and ZIF-90 materials. The water adsorption isotherm shows a pore filling pressure ($P/P_0 \sim 0.7$) distinct from ZIF-90 ($P/P_0 \sim 0.55$) and ZIF-8 (which is highly hydrophobic and does not display a pore-filling pressure under the present conditions). Furthermore, the saturation loading of water in the NSIC hybrid is equivalent to that of ZIF-90 since the entire pore volume is available for adsorption. The nitrogen physisorption isotherm also displays 'gate-opening' inflections distinct from those of the parent materials. This behavior, as also observed in our earlier work, is due to the fact that the pore windows in the NSIC hybrid are lined with both types of linkers[145], thereby conferring a distinct set of adsorption and diffusion characteristics in comparison to the parent

materials.[40, 104] The SALE hybrids display sharply contrasting behavior from the NSIC hybrids. The water adsorption isotherms show pore filling pressures ($P/P_0 \sim 0.55$-0.6) close to ZIF-90 but a much lower saturation loading than ZIF-90. This behavior clearly indicates the presence of distinct ZIF-90-rich domains (which allow pore-filling water uptake) and ZIF-8-rich domains (which remain inaccessible to water). The nitrogen physisorption isotherms of the SALE hybrids resemble that of the physical mixture of ZIF-8 and ZIF-90, further indicating the presence of ZIF-8-rich and ZIF-90-rich domains. The quite different functional properties of the hybrid ZIF materials synthesized by NSIC and SALE routes further support our hypothesis that they have drastically different degrees of linker mixing.

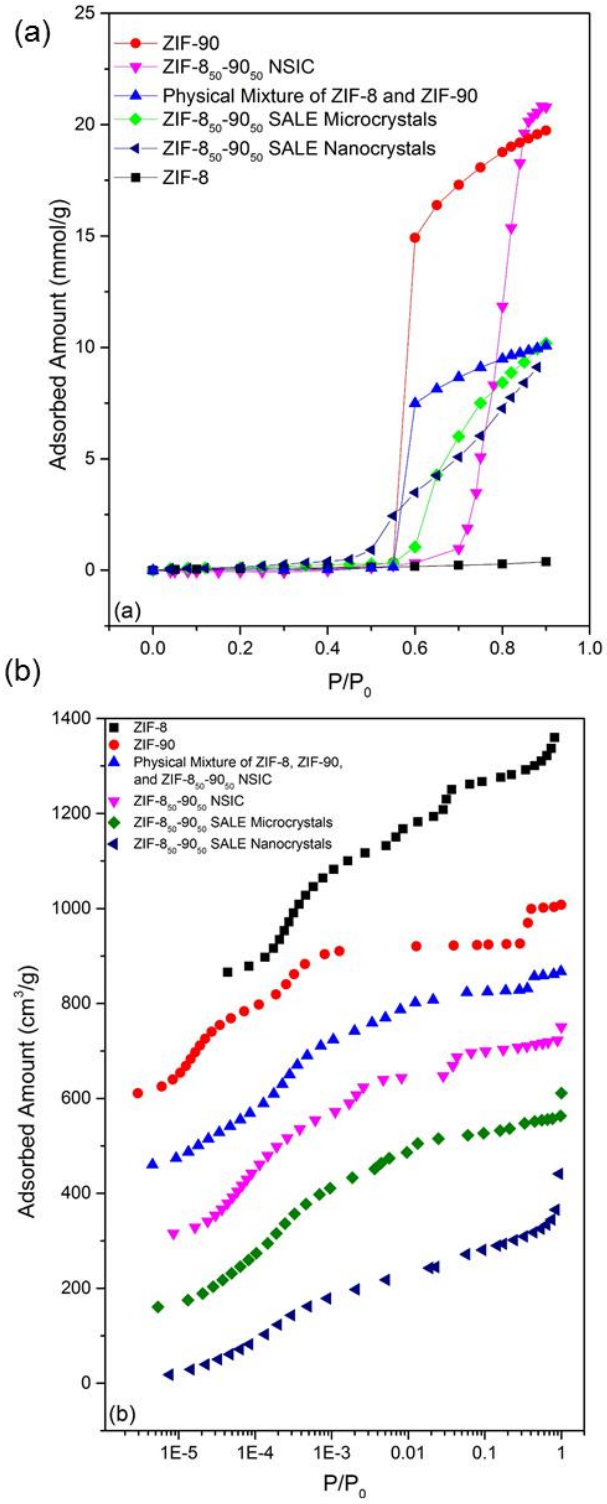

Figure 4.4. (a) Water adsorption isotherms and (b) nitrogen physisorption isotherms of ZIF-8, ZIF-90, physical mixture of ZIF-8/ZIF-90, NSIC hybrids and SALE hybrids. Isotherms in (b) are offset by 150 cm^3/g for convenience of display.

While the foregoing discussion gives substantive information about linker distributions in the hybrid ZIF crystals, so far no technique has been reported for direct visualization of linker distribution. To this end, we hypothesized that the native fluorescence of the imidazolate linkers (attributed to π^*-π^* transitions[146-147]) could be used to obtain such information. In particular, ZIF-8 crystals emit blue light (460 nm) and ZIF-90 crystals emit green light (505 nm) when excited by a 405 nm wavelength laser. The intensity of emission by ZIF-90 is considerably stronger than that of ZIF-8. Combining this fluorescence behavior with confocal microscopy, we can obtain information on linker distribution throughout the bulk of *de novo* and SALE hybrid macrocrystals (> 100 μm size). Thus a 3D mapping of the linker distribution near the surface as well as the interior of the crystals can be obtained using true-color fluorescence imaging, without the necessity of labeling with dye molecules. Figure 4.5a-5b show cross-sections of ZIF-8 and ZIF-90 crystals undergoing fluorescent emission. The insets show the orientations of these crystals relative to the objective lens of the microscope. Figure 4.5c shows emission from two crystals of a ZIF-8_{75}-90_{25} hybrid made via *de novo* synthesis. The composition was deliberately skewed towards a ZIF-8-rich hybrid to compensate for the higher intensity of fluorescence from ZIF-90 linkers. This material emits both blue and green light and the combined effect produces a cyan color. The presence of ZIF-8 and ZIF-90 throughout the entire crystal can be seen by filtering the images to show the blue and green emissions separately (inset of Figure 4.5c). There is uniformly distributed emission at both wavelengths throughout the cross-section. The blue and green emissions are uniformly distributed throughout the crystals, which is characteristic of a hybrid ZIF with the linkers being well-mixed. On the other hand, Figure 4.6a-6d show fluorescence from a ZIF-8_{90}-

90_{10} SALE hybrid crystal at four different focal planes (cross-sections. It is seen that the distribution of ZIF-90 linkers (green color) is limited to the outer edges of the crystals and that the interior of the crystals contain only ZIF-8 linkers (blue color). Thus, the SALE of ZIF-8 macrocrystals to ZIF-8-90 hybrid macrocrystals proceeds from the external surface and creates a core-shell type of compositional distribution. This is in agreement with the "apparent physical mixture" behavior exhibited during water and nitrogen adsorption, the slow spin exchange observed in CRAMPS NMR, as well as the visual appearance of SALE hybrids (brown color). The confocal microscopy results reported here are, to our knowledge, the first direct visual confirmation of linker mixing or clustering in *de novo* and SALE MOF hybrids respectively. This core-shell type distribution is similar to the result obtained for MOF-5/IRMOF-3 core-shell architectures verified using optical microscopy.[55] But unlike the MOF-5/IRMOF-3 crystals grown using a seeding method, no new metal source is added to the solution during SALE and therefore the mechanisms are not comparable. A ZIF-8/ZIF-67 core-shell system has also been reported in literature.[148] These crystals were also synthesized via a seed-mediated technique and hence use additional metal ions to grow the shell layer. No comparison of structure or properties with a well-mixed ZIF-8-67 hybrid was made.

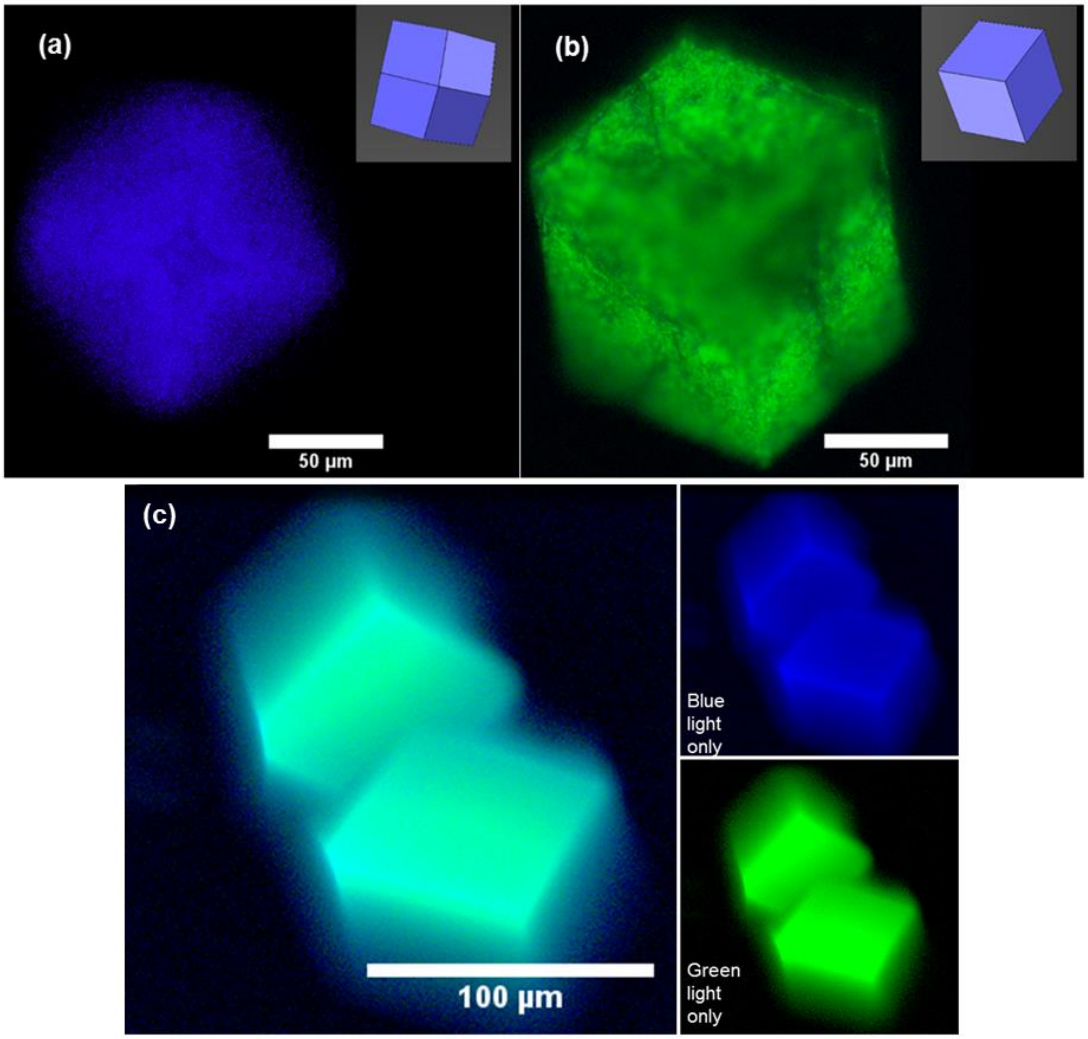

Figure 4.5. Fluorescent confocal images of (a) ZIF-8 crystal and (b) ZIF-90 crystal with relative crystal orientations in the inset and (c) a *de novo* ZIF-8_{75}-90_{25} hybrid (with blue and green emissions shown separately in the inset).

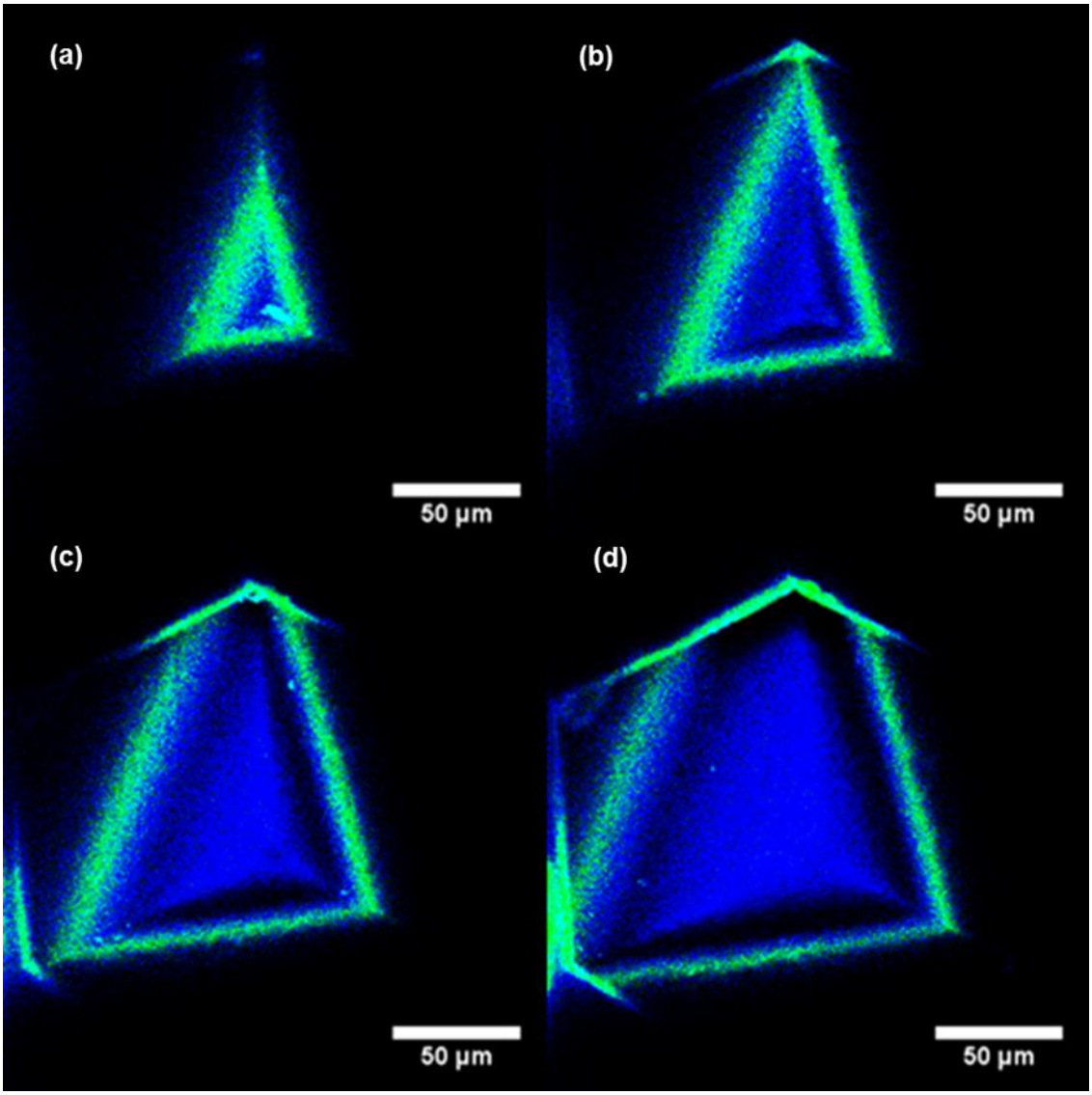

Figure 4.6. (a-d) Fluorescent confocal images of a SALE ZIF-8_{90}-90_{10} hybrid material at multiple focal planes moving progressively deeper into the bulk of the crystal.

We then performed a more detailed mechanistic study of the SALE process. Figure 4.7 shows the linker composition of (originally) ZIF-8 nanocrystals and microcrystals as a function of the SALE processing time at temperatures of 60° C and 90° C. During each experiment, crystal samples were drawn from the SALE reactor at different times ranging from 4 hours to 8 days, washed, dried, and activated. The sample was then dissolved in deuterium-substituted d_4-acetic acid and its composition was analyzed by ^{1}H-solution

NMR. For both microcrystals and nanocrystals, higher temperature promotes the rate of SALE, reflecting the activated nature of the overall process. Figure 4.7 is plotted with the square root of time on the *x*-axis. At 60° C the nanocrystals exhibits a linear increase in OHC-Im (ZIF-90 linker) incorporation versus $t^{1/2}$ for most the SALE processing time, indicating a diffusion-limited process. A similar behavior is seen for the nanocrystals at 90° C, except that the SALE rate is considerably faster (presumably due to the increased diffusivity of the linkers). The ZIF-90 linker fraction in the nanocrystals also saturates at about 90%, *i.e*., pure ZIF-90 nanocrystals are not obtained even though a large excess (2-MeIm:OHC-Im ~ 1:50) of ZIF-90 linkers is available in the reactor. We propose that initial exchange begins at the external surface of the nanocrystals and proceed into the crystal, but quickly becomes diffusion-limited since additional linker exchange would require the diffusion of OHC-Im linkers into the ZIF pores and the counter-diffusion of displaced 2-MeIm linkers out of the pores. The linker fraction of ZIF-90 in the crystals also saturates around 90% for SALE at both 60° C and 90° C suggesting that the exchange process has reached equilibrium. Figure 4.8a-8c show representative SEM images of the ZIF-8 nanocrystals before and after SALE at 60° C and 90° C, wherein it is apparent that no significant changes in crystal morphology or size distribution have occurred. Figure 4.7 also reveals a strong crystal size effect consistent with diffusion-limited processes. SALE on ZIF-8 microcrystals at 60° C proceeds at a slower rate than on nanocrystals at the same temperature and OHC-Im linker concentration in the solution. The microcrystals at 90° C also show a linear behavior similar to the nanocrystals at shorter SALE times (up to $t^{1/2}$ ~ 5). However, they subsequently show a sudden increase in linker exchange. We verified this behavior to be reproducible by performing the experiments thrice for each case to

estimate the error bars in Figure 4.7. This observation indicates that additional phenomena must be considered to provide a complete mechanistic description of SALE in these crystals.

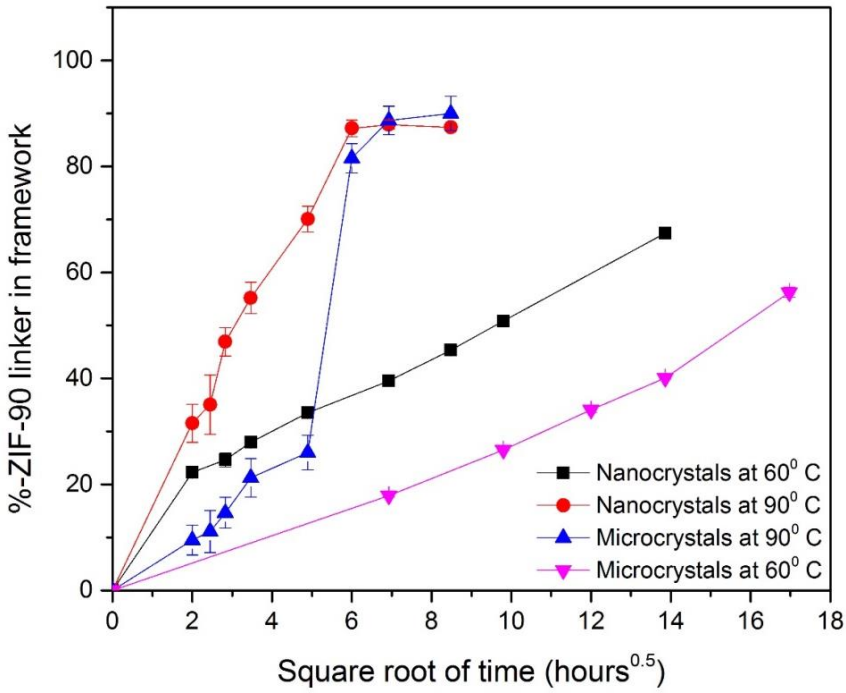

Figure 4.7. Composition of ZIF-8-90 SALE hybrids versus square root of time for two crystal size ranges at two temperatures. The lines joining the data points are only to guide the eye.

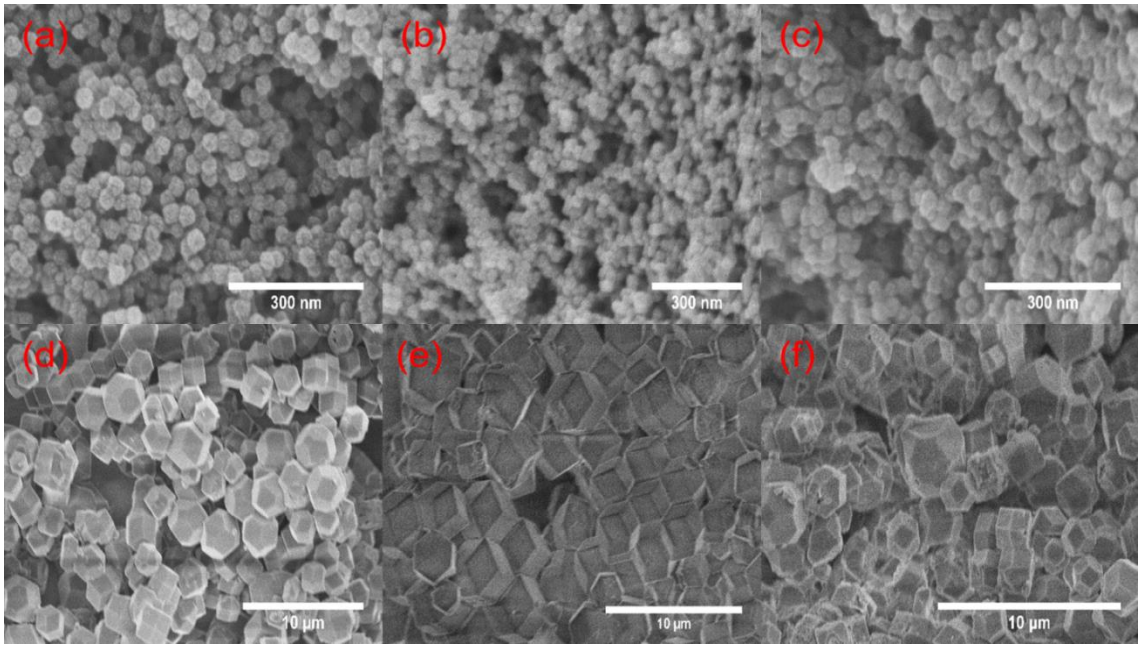

Figure 4.8. **(a)** ZIF-8 nanocrystals before SALE, **(b)** ZIF-8-90 nanocrystals after SALE at 60° C and 3 days, **(c)** ZIF-8-90 nanocrystals after SALE at 90° C and 8 hours, **(d)** ZIF-8 microcrystals before SALE, **(e)** ZIF-8-90 microcrystals after SALE at 60° C and 12 days, **(f)** ZIF-8-90 microcrystals after SALE at 90° C and 4 days.

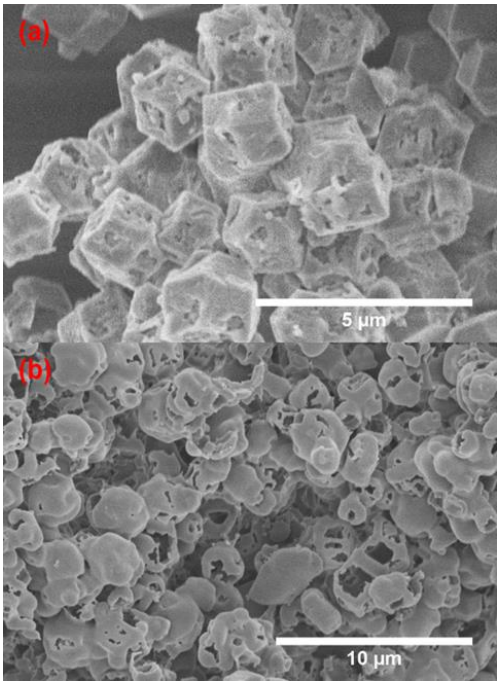

Figure 4.9. SEM images depicting crystal pitting and etching observed during SALE in ZIF-8 microcrystals at **(a)** 90° C for 4 days and **(b)** 120° C for 2 days.

SEM images of the microcrystals (Figure 4.8d-8f**)** do not indicate significant changes in crystal size distribution. However, Figure 4.8f indicates the formation of defects on the crystal surfaces at higher SALE temperatures and times (90° C and 4 days). This is further highlighted in Figure 4.9a, wherein a significant fraction of crystals show surface etching/pitting and some crystals have been 'hollowed out' by partial dissolution. To verify this behavior, we also performed SALE at a higher temperature of 120° C, and observed even greater etching and partial dissolution of the microcrystals (Figure 4.9b). This loss of ZIF-8 linkers from the solid phase partially explains the deviation from diffusion-limited exchange (*i.e.*, a rapid increase in the ZIF-90 linker fraction) observed in Figure 4.7 for the microcrystals undergoing SALE at higher temperatures and times (90° C and 4 days). Additionally, etching or partial dissolution of the microcrystals introduces both Zn^{2+} ions as well as ZIF-8 linkers into the initial SALE solution which only contained ZIF-90 linkers. This solution may be capable of forming additional mixed-linker ZIF-8-90 crystals with ZIF-90 as the majority constituent owing to its excess in the solution. Finally, one must also consider the possibility that pure ZIF-90 crystals may nucleate and grow in the solution by using the Zn^{2+} ions released during etching of the ZIF-8 crystals. Both these possible mechanisms could play a role in the observed deviation from diffusion-limited behavior at harsher SALE conditions.

To investigate these issues, we first performed a control experiment in which the solution was maintained at the same conditions (temperature, time) as in the SALE process but with ZIF-8 crystals absent. In this experiment the solution also contained zinc nitrate (with Zn:OHC-Im molar ratio of 1:4), which is a significantly higher Zn^{2+} concentration than would be obtained if all the ZIF-8 microcrystals dissolved and released Zn^{2+} ions

during SALE (~1:20). No ZIF-90 crystals were formed in this experiment, and so we can rule out the possibility of formation of pure ZIF-90 crystals during SALE. However, in previous work we have crystallized mixed-linker ZIF-8-90 crystals at 90° C by heating a solution containing only 2-MeIm, OHC-Im, and zinc nitrate in methanol.[104] In that synthesis, the Zn^{2+} concentration was 50 mmol. L^{-1} and the Zn:2-MeIm:OHC-Im ratio in the solution was 1:3:1. If all the ZIF-8 crystals in the present SALE experiments were to dissolve, the Zn^{2+} concentration would be 6.2 mmol. L^{-1} and the Zn:2-MeIm:OHC-Im ratio in solution would be roughly 1:2:20. We analyzed three supernatant solutions after SALE reactions at different temperatures and durations (13 days at 60° C, 7 days at 90° C, and 2 days at 120° C) using ICP-MS. The concentrations of Zn^{2+} in these solutions were found to be in the range of only 40-130 ppm. We prepared solutions with similar concentrations of Zn^{2+} and 2-MeIm:OHC-Im ratio of 1:10. These solutions were heated to 60° C, 90° C and 120° C respectively in sealed reactors. No mixed-linker ZIF-8-90 crystals were found under these conditions. Hence, we can exclude the formation of mixed-linker ZIF-8-90 crystals during SALE even when the crystals undergo morphological transformation as a result of linker etching. Figure 4.10 shows the crystal size distributions (obtained from multiple SEM images) before and after SALE at 120°C for 2 days. The distribution is virtually unchanged after SALE, further supporting the absence of new mixed-linker ZIF-8-90 crystals forming from the solution.

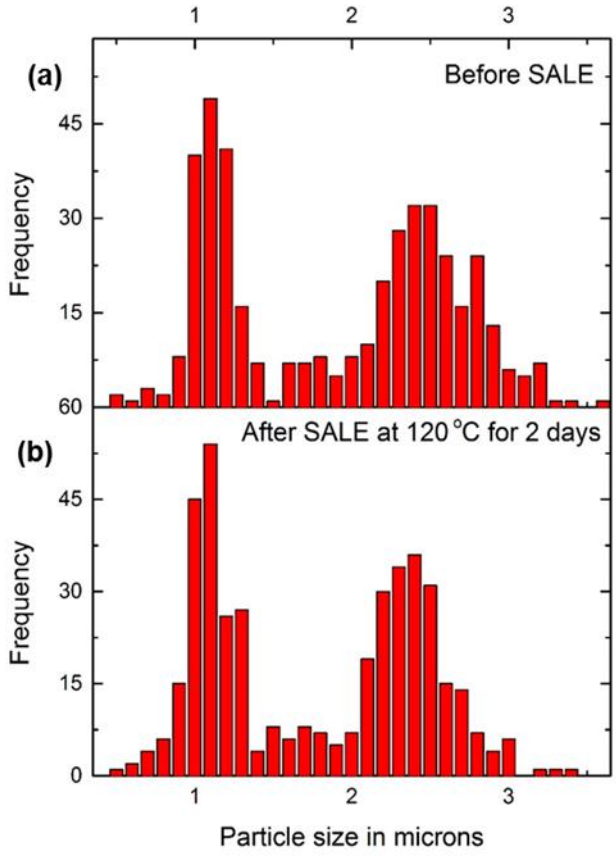

Figure 4.10. Size distribution of ZIF-8 microcrystals: **(a)** before SALE and **(b)** after SALE at 120° C for 2 days.

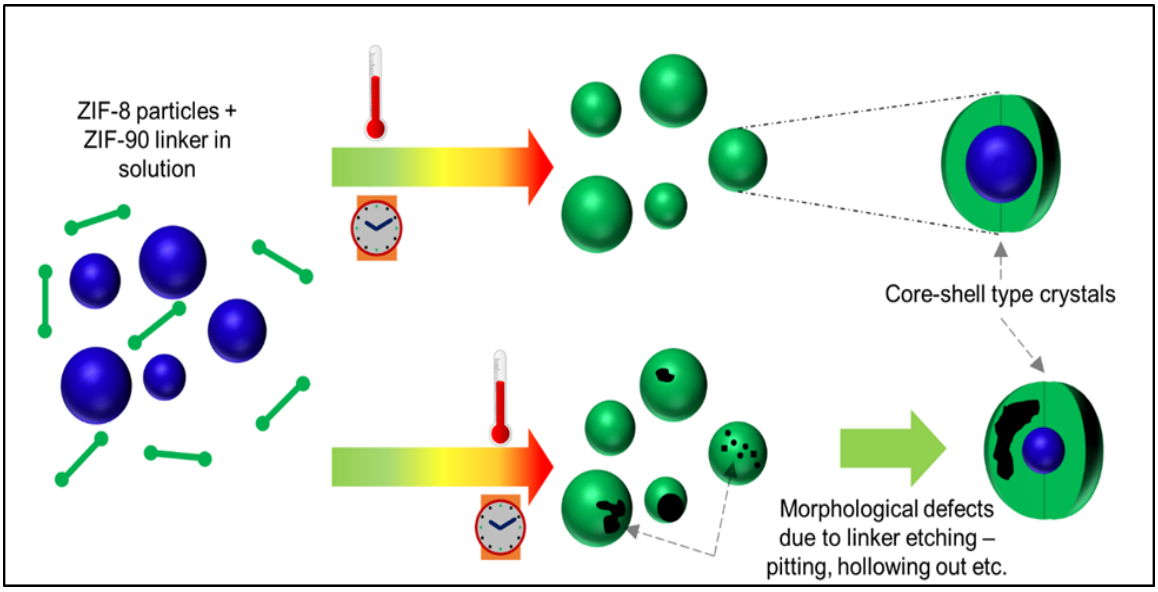

Figure 4.11. Schematic mechanism of ZIF-8 → ZIF-90 solvent assisted linker exchange (SALE).

4.4 Conclusions

We synthesized a family of mixed-linker ZIF-8-90 materials via solvent assisted linker exchange (SALE) and non-solvent induced crystallization methods. Using ^{1}H-CRAMPS NMR, we demonstrated a simple way to distinguish SALE and *de novo* mixed-linker materials at a unit-cell level. The effect of linker mixing on functional properties is elucidated using water adsorption and nitrogen physisorption. We have demonstrated that these two synthesis routes can lead to hybrid ZIFs with the same overall composition but drastically different properties attributed to the difference in linker mixing achieved via these two routes. Figure 4.11 shows a schematic summary of the SALE mechanism in ZIF-8-90 materials, based upon all the findings of this work. This mechanism may also hold a more general validity for other ZIF systems in which diffusion of bulky imidazolate linkers through small or medium-sized pores (4-6 Å) of the ZIF framework can be expected to limit the SALE rate. Regardless of the crystal size regime (nano/micro/macro), the initial

mechanism for linker exchange is seen to be a diffusion-limited process resulting in core-shell crystals. In the case of macrocrystals, these core-shell structures could be directly imaged for the first time with fluorescence confocal microscopy. In the case of nanocrystals, diffusive processes appear to be fast enough to complete the linker exchange and reach equilibrium before other processes such as crystal etching and dissolution can exert significant effects. In the case of micro/macrocrystals, the diffusion-limited exchange is much slower and other processes become significant at extended SALE durations. The crystals undergo etching and partial dissolution, releasing significant amounts of Zn^{2+} ions and ZIF-8 linkers into the solution and leading to morphological defects such as pits and holes in the SALE-treated crystals. However, control experiments show that neither new crystals of pure ZIF-90 nor mixed-linker ZIF-8-90 are formed in the solution, When synthesizing hybrid ZIFs *via* SALE, care must be taken to ensure that the processing conditions do not cause damage to the ZIF material. Both the SALE and *de novo* techniques are very useful for synthesizing MOFs with controlled compositions and functionality. Our findings clearly indicate that the products of SALE and *de novo* processes for hybrid ZIF materials can be significantly different, and hence the characterization of linker-mixing is of utmost importance when dealing with these materials.

Due to the spontaneous nature of linker exchange processes, we hypothesize that these techniques can also be utilized to benefit ZIFs that have undergone degradation due to external factors such as acid-gas attack. We can ask the question whether damaged linkers can be replaced with fresh linkers to restore degraded crystals to their pristine state. In the next chapter, we present a modified SALE process wherein the native linker in the degraded ZIF material and the new linker introduced in the solvent phase are the same. We

study the results of this ‘healing process’ towards structural and functional restoration. We are also able to get a better understanding of the different changes that ZIF materials undergo when they are subjected to acid-gas exposure. This method and subsequent findings represent a significant advance in our understanding of ZIF stability in acid-gas environments.

CHAPTER 5. RECOVERY OF ZIFS DAMAGED BY ACID-GAS ATTACK

5.1 Introduction

The characteristics that make ZIF-8 an attractive subject for research include its facile synthesis, excellent thermal and chemical stability, well defined pore structure, and versatility of applications. ZIF-8 has been demonstrated to have applications in gas separations, liquid separations, catalysis, chemical sensors, drug delivery, chemical extraction etc.[20-22, 31-33, 146, 149-154] Unlike many other MOFs, ZIF-8 has been shown to be stable under a range of experimental conditions.[17, 71] However, ZIF-type MOFs have been known to dissolve in acidic solutions and this property has been used to analyze their composition using ^{1}H-solution NMR.[40] Recent studies have shown that even ppm-level of acid gases like SO_2 can cause significant damage to ZIF-8 crystals when exposed through an aqueous solution or a water vapor mixture.[72, 155] The damage to the ZIF-8 structure manifests as a loss of surface area, porosity and crystallinity. Visible change to the appearance and texture of the crystals have also been reported. The damage is caused by the cleavage of the Zn-imidazole bond due to the protonation of the nitrogen atom on the imidazole linker. Because of the chemical nature of this degradation, it would typically be regarded as a permanent change to the ZIF structure.[72]

So far, efforts for improving MOF stability have all involved introducing structural modifications, linker functionalization or metal substitutions.[74-75, 156-157] While these modifications can be effective, they can lead to loss in surface area and/or pore volume due

to bulkier linkers, change physical and chemical properties and also make the synthesis more cumbersome and expensive. An alternative to these material replacement strategies would be to regenerate a MOF after damage caused by environmental exposure. In this study, we present a simple and effective route (Solvent Assisted Crystal Redemption – SACRED) to reverse the damage caused by an acid gas to ZIF-8 and its analogue ZIF-14. We demonstrate that the crystallinity, surface area, and pore volume can be completely recovered for ZIF-8 (and partially for ZIF-14) using this method, even for samples that have been severely degraded. We show that recovered ZIF-8 is structurally and chemically identical to its pristine counterpart. We also investigate the mechanism for this recovery process using isotopically labelled linkers.

5.2 Experimental Methods

Materials. Zinc nitrate hexahydrate (Alfa Aesar), 2-methylimidazole (2-MeIm)(Sigma Aldrich), 2-ethylimidazole (2-EtIm)(Sigma Aldrich), imidazole-2-carboxaldehyde (OHC-Im)(Alfa Aesar), deuterium-substituted 2-methylimidazole (d_6-2-MeIm), sodium formate (Alfa Aesar), methanol (EMD), N,N-dimethylformamide (BDH), and octanol (Sigma Aldrich) were used as received.

ZIF-8 Synthesis. Synthesis of ZIF-8 was performed by modifying the procedure given by Zhang et al. [32] Typically, 0.297 g $Zn(NO_3).6H_2O$ was dissolved in 20 mL methanol. 0.164 g 2-MeIm and 0.269 g HCOONa were dissolved in 20 mL methanol. Both solutions were mixed together and transferred to a Teflon liner. The liner was then sealed inside a Parr instruments stainless steel reactor and then incubated at 90° C for 24 hours. The reactor was then cooled to room temperature and the crystal were collected and washed

with fresh methanol thrice before air drying the crystals at 60° C. Dried crystals were then degassed at 180° C in vacuum overnight.

ZIF-14 Synthesis. ZIF-14 crystals were synthesized as follows. 1.923 g of 2-EtIm was dissolved in 50 mL deionized water by stirring using a magnetic bar. 1.487 g of $Zn(NO_3).6H_2O$ was dissolved in 50 mL 1-octanol and then poured into the linker solution while being stirred. The mixture was kept stirred for 2.5 hours. The resulting milky solution was centrifuged at 8500 rpm for 15 minutes followed by washing with fresh methanol thrice. The crystals were air dried at 80° C and then degassed in vacuum at 180° C overnight.

ZIF-90 Synthesis. ZIF-90 crystals were synthesized by using the procedure given by Gee et al.[35] 1.485 g of $Zn(NO_3)_2.6H_2O$ and 1.920 g of OHC-Im were dissolved in 100 mL of N,N-dimethylformamide. The solution was continuously stirred while heating up to 393 K. The temperature was held at 393 K for 10 minutes and then cooled down to room temperature. The solution was left undisturbed for 2 days. Crystals were collected from the side of the container and then exchanged with methanol for 24 hours. After solvent exchange, the crystals were dried in air at 60° C and then degassed in vacuum at 180° C overnight.

Characterization. X-Ray Diffraction (XRD) measurements were performed on ZIF samples using an X'Pert Pro PANalytical diffractometer (CuKα source, λ = 0.1.541 nm). Measurements were carried out over a range of 2θ = 3-45°, with the powder samples being dispersed on a low-background sample holder. Scanning Electron Microscopy (SEM) images were collected on a Hitachi SU8010 field emission microscope at 3 kV accelerating

voltage. Nitrogen physisorption isotherms were collected at 77 K using a Micromeritics TriStar analyzer. Deuterated linker replacement analysis of the recovered ZIFs were carried out using a Bruker Avance III 400 MHz solution-state Nuclear Magnetic Resonance (NMR) spectrometer after dissolving the ZIF in acetic acid. Butanol adsorption isotherms were collected using the Surface Measurement Systems (SMS) Dynamic Vapor Sorption (DVS) Resolution instrument under nitrogen flow.

Acid gas exposure. ZIF samples were exposed to humid SO_2 according to the procedure reported in our previous work.[72, 158] Briefly, samples were exposed to varying ppm-level concentrations of SO_2 at 85% relative humidity for different durations at 25° C. SO_2 was generated using an aqueous solution of $NaHSO_3$ and introduced into the sample chamber using a bubbler.

Solvent Assisted Crystal Redemption (SACRED). Approximately 100 mg of degraded ZIF samples were dispersed inside a Teflon liner. For ZIF-8 recovery, 0.821 g (10 mmol) of 2-MeIm was dissolved in 40 mL methanol and then added to the liner. The liner was then sealed inside a Parr instruments reactor and then incubated in an oven at 90° C for 48 hours. ZIF-14 recovery was performed using the same procedure except with 0.961 g of 2-EtIm dissolved in 40 mL methanol. After recovery, the mother liquor was decanted and stored separately for analysis. The crystals were washed with fresh methanol thrice and then air dried at 60° C. The same procedure was repeated with d_6-2-MeIm for isotopic labeling of ZIF-8 linkers.

5.3 Results and Discussion

ZIF-8 crystals were characterized using XRD, SEM, nitrogen physisorption, and FTIR spectroscopy before exposure to SO_2, after exposure to SO_2 and after the SACRED process. Pristine ZIF-8 was divided into batches of ~ 150-200 mg for exposure to SO_2. After exposure, recovery experiments were performed on these samples with varying levels of degradation to ascertain reproducibility as well as to gauge how much damage can be endured before it becomes irreversible. The loss of surface area and pore volume after SO_2 exposure and amounts regained after the SACRED procedures are tabulated below in Table 5.1. It can be seen that even after losing ~100% of surface area and pore volume to acid gas attack, ZIF-8 crystals are amenable to recovery using this method.

Table 5.1. Surface area and pore volumes of ZIF-8 before SO_2 exposure, after SO_2 exposure and after SACRED treatment

Material	Humid SO_2 exposure condition	Batch	Surface area (m^2/g)	Pore volume (cm^3/g)
Pristine ZIF-8 (activated)	-	-	1341±44	0.64±0.01
ZIF-8 exposed to humid SO_2 (activated)	100 ppm-days	1	510±30	0.25±0.01
		2	484±24	0.24±0.01
		3	245±20	0.13±0.01
	200 ppm-days	4	~ 0	~ 0
Exposed ZIF-8 post SACRED (activated)	100 ppm-days	1	1355±51	0.63±0.02
		2	1329±28	0.63±0.01
		3	1270±32	0.62±0.02
	200 ppm-days	4	1214±20	0.58±0.01

Figure 5.1 shows the XRD patterns of pristine ZIF-8, post-degradation ZIF-8 and post-SACRED ZIF-8 plotted without offsets. The ordinate axis of the plot is expressed in logarithmic coordinates for visual clarity and the peaks are normalized to the highest peak

(2θ = 7.33°). We had previously reported the change in XRD pattern of ZIF-8 upon exposure to humid SO_2 where the heightened background signal and the loss of peak intensities were attributed to the degradation and gradual amorphization of the crystals.[72] In contrast, the material after SACRED treatment has regained most of the peak intensity and the background signal is noticeably reduced. These measurements show that the loss of crystallinity induced by the acid-gas attack is almost completely regained as a result of the SACRED treatment.

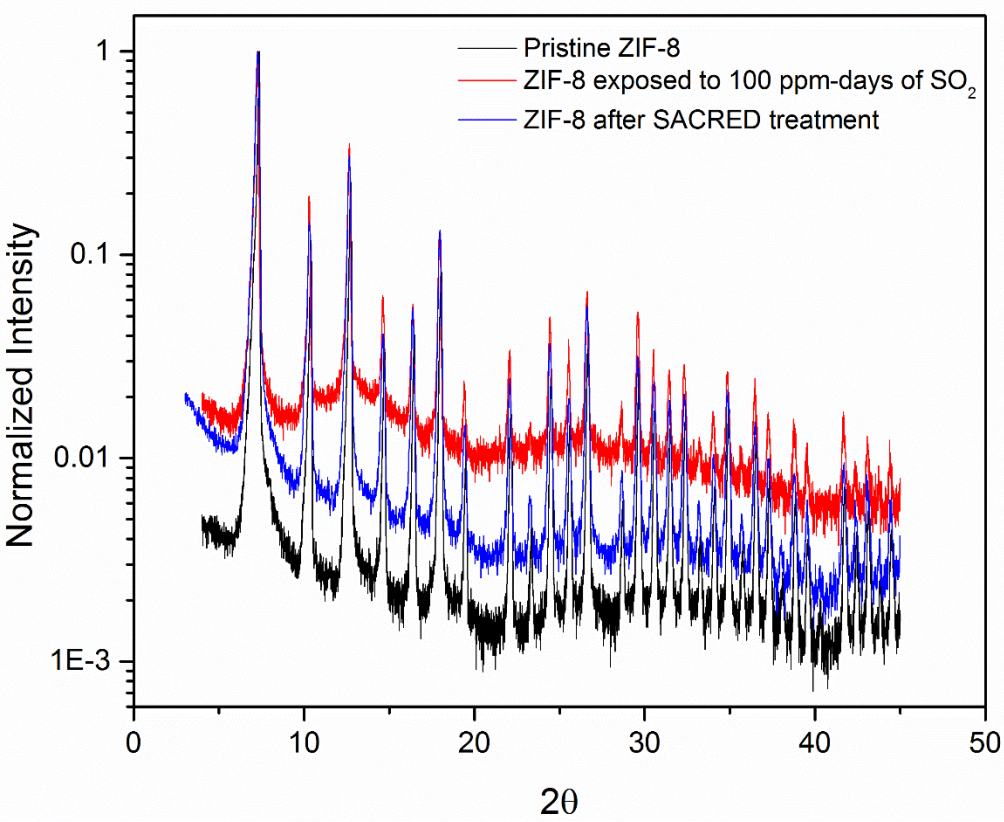

Figure 5.1. XRD patterns of pristine ZIF-8, ZIF-8 exposed to 100 ppm-days of humid SO_2, and ZIF-8 crystals after SACRED treatment. The ordinate axis is plotted in logarithmic scale without offsets. Peaks are normalized to the highest peak at 2θ = 7.33°.

Figure 5.2 shows photographs (a-c) of ZIF-8 at various stages during these experiments and corresponding SEM images (d-f). Pristine ZIF-8 is white in color with a

fine powdery texture, and individual crystals have a rhombic dodecahedron morphology. After exposure to SO_2 these crystals turn into an off-white to yellow shade with more agglomeration of particles. The SEM image of these crystals show that they appear to have undergone certain morphological changes, with a veneer of apparently amorphous features covering the particles. After the SACRED treatment, the crystal texture is restored but they have a very pale pink tint. The color fades with repeated washing of the crystals in fresh methanol. SEM images show some unidentified particles adhering to the surface of the crystals that could be contributing to the appearance of the pink color.

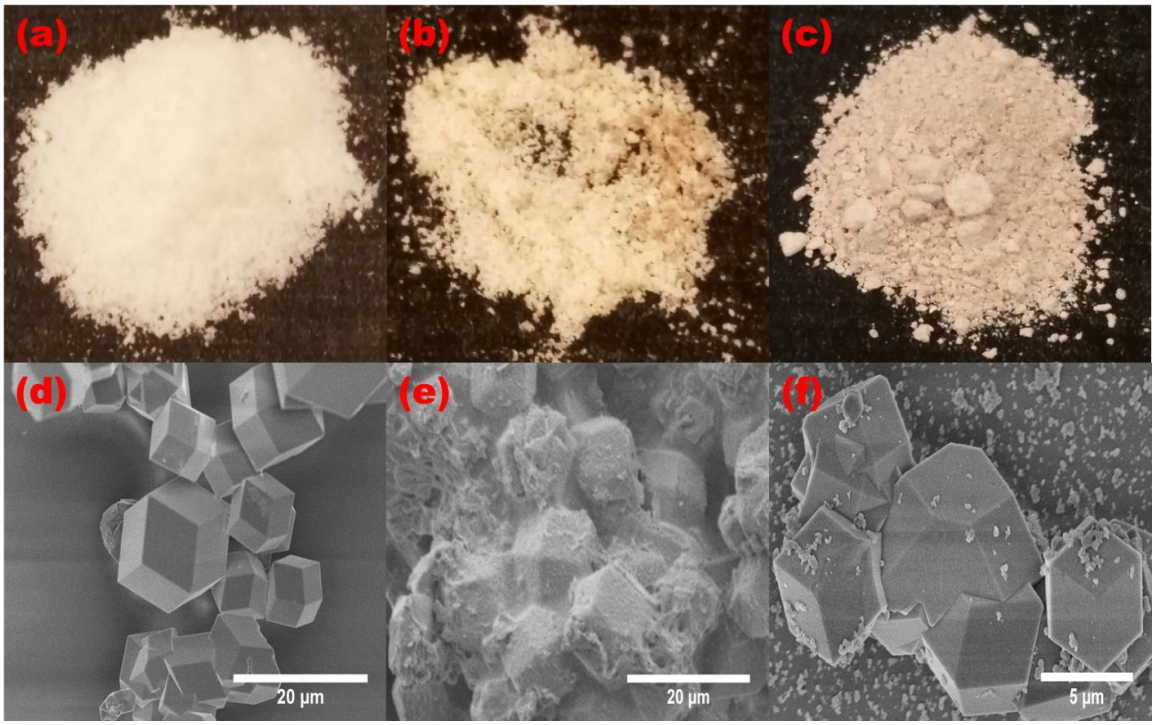

Figure 5.2. (a) Pristine ZIF-8 particles (b) ZIF-8 after exposure to 100 ppm-days of humid SO_2 (c) ZIF-8 after SACRED treatment (d) SEM image of pristine ZIF-8 (e) SEM image of ZIF-8 after exposure to 100 ppm-days of humid SO_2 and (f) SEM image of ZIF-8 after SACRED treatment. The images in (a)-(c) occupy approximately 2.5x2.5 cm^2 of area.

We tested the functional performance of recovered ZIF-8 by measuring 1-butanol adsorption at 30° C. Figure 5.3 shows the adsorption isotherms collected for pristine ZIF-

8 and ZIF-8 recovered via SACRED after humid SO_2 degradation. Both crystals showed similar adsorption profiles, with post-SACRED crystal exhibiting a slightly higher uptake than pristine ZIF-8. This can be attributed to the higher measured surface area of both samples (~ 1300 m^2/g for pristine ZIF-8 vs. ~ 1400 m^2/g for post-SACRED sample). Nevertheless, it is clear that there is no loss of adsorption sites in post-recovery ZIF-8 and that SACRED treatment can restore ZIF-8 to pre-acid-gas-exposure conditions.

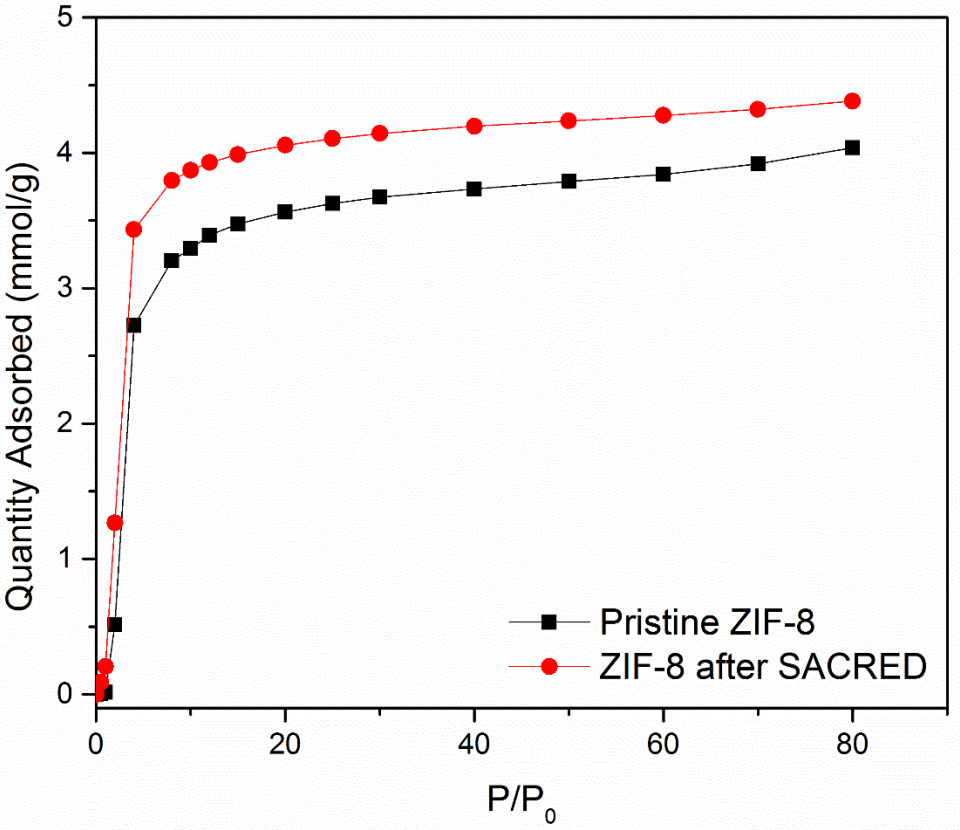

Figure 5.3. Butanol adsorption at 30° C in pristine ZIF-8 and ZIF-8 recovered via SACRED after humid SO_2 exposure.

In order to further understand the transformation that these crystals undergo during the SACRED process, we studied the chemical nature of the crystals at every stage of the cycle. FTIR spectroscopy analysis of the particles at different stages of the experiment are

shown in Figure 5.4a-b. The spectrum obtained from the ZIF-8 sample before exposure agrees well with literature.[159-161] Peaks in the range of 900-1350 cm^{-1} can be assigned to the in-plane bending of the imidazole ring, while peaks below 800 cm^{-1} can be assigned to out-of-plane bending of the ring.[159, 161] Specifically, the peak at 1146 cm^{-1} can be attributed to =C-H bending[160], the peak at 1582 cm^{-1} results from C=N stretching, and bands observed between 1350 and 1500 cm^{-1} are associated with the ring vibrations.[159, 161] The peak at 2930 cm^{-1} is due to the C-H symmetric stretch of the methyl group[160] whereas the asymmetric stretch peak is at 2980 cm^{-1}. The =C-H stretch for the aromatic ring can be observed at 3134 cm^{-1} as in previous literature reports.[160-161] The Zn–N stretch mode at ~420 cm^{-1} could not be observed due to the limitations of the instrument used.

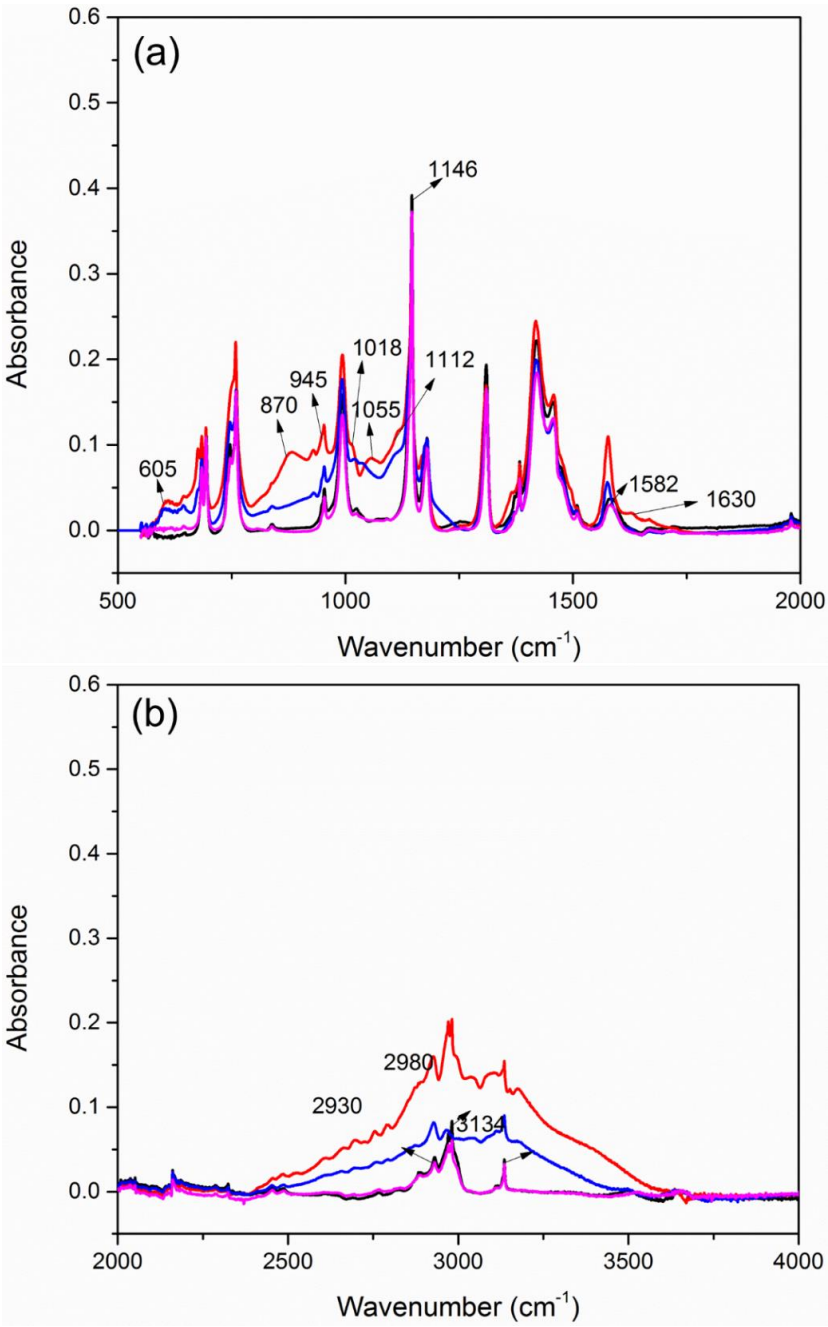

Figure 5.4. (a). FTIR spectra for pristine ZIF-8 (black), ZIF-8 exposed to 100-ppm days of SO2 before activation (red) and after activation (blue) and ZIF-8 after SACRED treatment (pink). (b) The same spectra as in (a) but at higher wavenumbers.

For ZIF-8 exposed to 100 ppm-days of humid SO_2 (before reactivation), several new peaks are observed. These peaks have been characterized in details in our previous

study and they can be attributed to the (bi)sulfite or (bi)sulfate groups along with adsorbed SO_2.[72] In general, the broad absorption region centered around 870 cm^{-1} and the peaks at 946 cm^{-1} and 1018 cm^{-1} are characteristic of the presence of (bi)sulfite groups.[162-164] The peaks at 605 cm^{-1}, 1055 cm^{-1} and 1112 cm^{-1} can be attributed to the vibrations of the (bi)sulfate group.[165-167] The broad absorption region from 2300-3600 cm^{-1} observed in ZIF-8 exposed to humid SO_2 is comprised of the hydrogen-bonded NH stretch region along with an OH stretch region from ~3200 cm^{-1} onwards indicating the protonation of the nitrogen of the 2-MeIm linker and resulting cleavage of the Zn-N coordination bond of ZIF-8 during humid SO_2 exposure.[168] In the reactivated humid SO_2 exposed sample, the peak intensities decrease substantially in the broad (bi)sulfite stretch region centered around 870 cm^{-1} while those corresponding to the (bi)sulfate groups and adsorbed SO_2 also decrease in intensity. The water bending peak at 1630 cm^{-1} disappears, whereas the intensities of the NH stretch and OH stretch region decrease. The overall FTIR spectrum of the reactivated ZIF-8 after humid SO_2 exposure is still significantly different from the pre-exposed ZIF-8 with incomplete removal of sulfur-containing species from the humid SO_2 exposed ZIF-8.

Inspection of the post humid SO_2 reactivated ZIF-8 sample after SACRED treatment reveals a close match with the pre-exposed ZIF-8 sample. The broad peak around 870 cm^{-1} along with the other peaks corresponding to the (bi)sulfite and (bi)sulfate groups disappear completely along with the broad stretch region from 2300-3600 cm^{-1}. A small decrease in the intensity of the peaks associated with ring vibrations (1350-1500 cm^{-1}) is observed while any other minute differences in peak intensities observed are a result of the manual baseline corrections. The FTIR results thus indicate removal of any residual

(bi)sulfite or (bi)sulfate groups from the reactivated humid SO_2 exposed ZIF-8 sample, and presence of NH or OH stretch regions are not observed. The sample after SACRED treatment appears chemically identical to the pre-exposed ZIF-8 sample.

The absence of sulfur species from the post-SACRED samples indicate that the removal of these acidic species is critical to the recovery process. In our previous work, the ZIF-8 degradation mechanism that we proposed involved an acid proton cleaving the Zn→N coordination bond.[72] This leads to the loss of surface area and porosity due to the blockage of pores by the dangling linker-acid complex. Therefore, restoration of crystallinity and porosity could be achieved by (a) removal of the acid molecule by reaction with a base (fresh 2-MeIm used in SACRED) and the dangling linker snapping back into place or (b) the replacement of the entire dangling linker-acid complex with a fresh linker from the SACRED solution. We attempted SACRED treatments with 3 alternative alkaline solutions – 2-MeIm in water, NaOH in water, and NaOH in methanol. We found that the crystals did not show any recovery in crystallinity or porosity in any of these experiments. The failure of aqueous solutions is attributed to the retention of hydrophobicity by the ZIF-8 crystals even after degradation by exposure to SO_2. The ineffectiveness of NaOH showed that the recovery process is not achieved through a simple removal of the acid molecules by a base.

For testing the second mechanism proposed above, we performed a SACRED treatment with deuterium-substituted 2-MeIm ($C_4D_6N_2$). We also treated a pristine sample of ZIF-8 with these linkers to see if there is any 'background exchange' even when there is no acid degradation. Samples of pristine ZIF-8 (no treatment), pristine ZIF-8 (SACRED with $C_4D_6N_2$), and post-SO_2-exposure ZIF-8 (SACRED with $C_4D_6N_2$) were digested in

acetic acid inside an NMR tube. Known amounts of deuterium-substituted acetic acid (CD_3COOD) were added to each tube to act as reference for quantification. Figure 5.5 shows the solution ^2H NMR spectra for all 3 samples. Pure ZIF-8 has no measurable ^2H peaks corresponding to the methyl functional group or the 4 and 5 positions on the imidazole ring due to the relatively low natural abundance (~ 0.01%) of deuterium. ZIF-8 treated with deuterium-enriched linker shows noticeable peaks at both positions. By comparing the integrated peak intensities to the molar amount of CD_3COOD added, we found that approximately 6-7% of linkers in pristine ZIF-8 were replaced by the isotopically labeled linkers from the SACRED solution. A similar analysis of the post-exposure sample showed that nearly 40% of linkers were replaced by $C_4D_6N_2$. This increased incorporation of the labeled linkers is clear evidence that the mechanism for crystallinity and porosity recovery proceeds via the replacement of the dangling linker-acid complex by a fresh linker from the SACRED solution. The linker-acid complexes expelled from the framework could be appearing as the amorphous features seen under SEM in Figure 5.2(f).

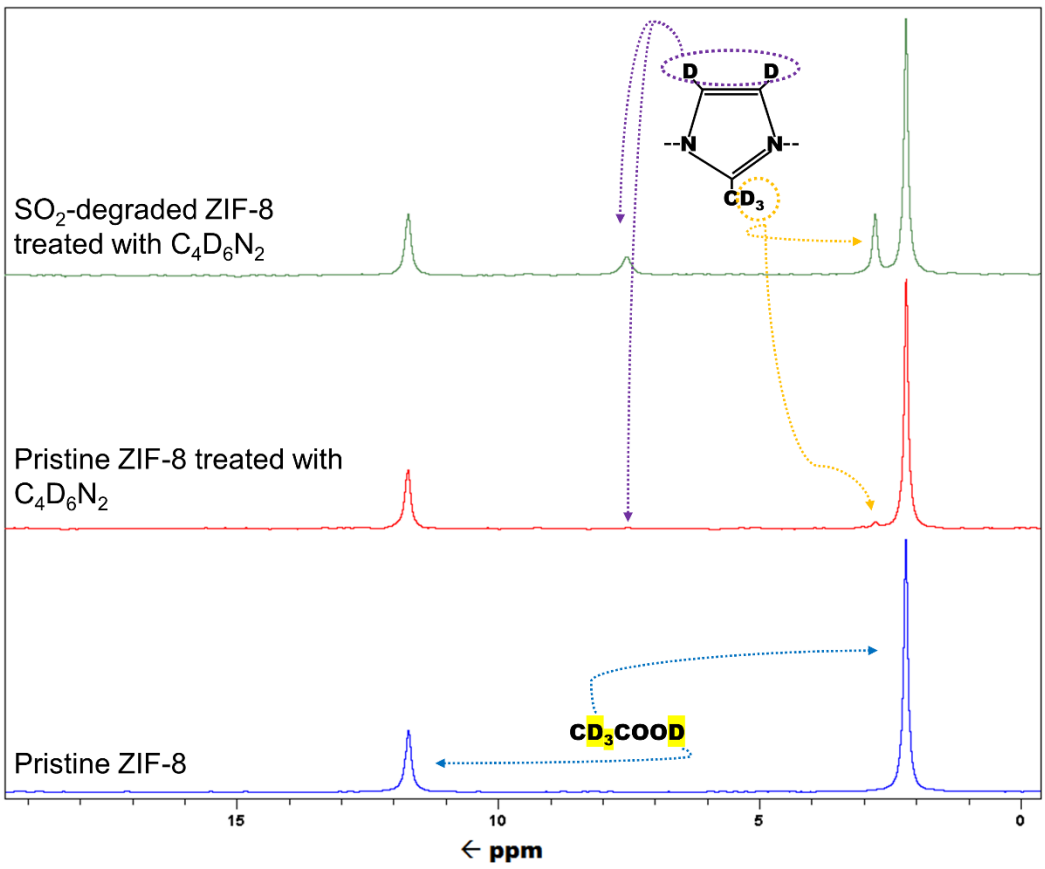

Figure 5.5. ^{2}H NMR spectra of pristine ZIF-8, pristine ZIF-8 treated with deuterium-substituted 2-MeIm and SO_2 degraded ZIF-8 treated with deuterium substituted 2-MeIm. Peaks are scaled for convenience of display.

To explore the applicability of our method to other ZIFs, we performed SACRED treatment on ZIF-14 (2-ethylimidazole linker) and ZIF-90 (imidazole-2-carboxaldehyde linker) crystals that were exposed to humid SO_2. ZIF-14 is chemically similar to ZIF-8 with the methyl functional group in ZIF-8 replaced by an ethyl group. These two materials have different crystal structure, since ZIF-14 crystallizes in an ANA topology.[84] ZIF-14 has very small pore apertures as compared to ZIF-8 and its relatively dense structure has low surface area and porosity. ZIF-90 shares the same crystal topology with ZIF-8 (SOD) and has very similar lattice parameters. Due to the presence of the aldehyde functional group and possible hydrogen bonding sites in ZIF-90, this material is very hydrophilic.[35] We were

unsuccessful in using SACRED to recover surface area lost during degradation of ZIF-90, including in experiments using methanol or DMF as solvents. In ZIF-90, the presence of the reactive carbonyl group may create a difference in the mechanism of degradation. If the acid gas molecule is chemisorbed at the functional group site, then there is no longer a dangling linker-acid complex that can be easily removed by a fresh linker molecule. In contrast, ZIF-14 showed almost 80% recovery in surface area on treatment (as shown in Table 5.2). The absence of complete recovery in ZIF-14 is attributed to the narrow pore structure of the material, which we hypothesize impedes the diffusion of fresh linker into the framework and the removal of existing linker-acid complexes from the matrix. For the ZIF-14 material that had been completely degraded by humid SO_2 (as characterized by surface area), only ~19% of the material's surface area was recovered after SACRED treatment.

Table 5.2. Summary of ZIF-14 humid SO_2 exposure and SACRED treatment

Surface area of pristine sample (m^2/g)	# of days of exposure to 20 ppm of humid SO_2	Surface area after exposure (m^2/g)	Surface area after SACRED treatment (m^2/g)
550	1	290	421
550	2	250	442
550	3	180	470
480	8	0	89

Recent studies have shown that treatment of ZIF membranes with linker solutions at elevated temperatures can improve the separation factor and stability of these membranes.[169-170] In those instances, the improved performance and durability of the membranes were attributed to the healing of defects at grain boundaries and interfaces of the membranes. We have demonstrated here that a similar treatment can be used to reverse large scale degradation of ZIF-8 and ZIF-14 particles by acid gas molecules. This

observation raises the possibility that the earlier membrane experiments may have shown performance improvement due to 'healing' of structural defects in the bulk crystals used in those experiments.

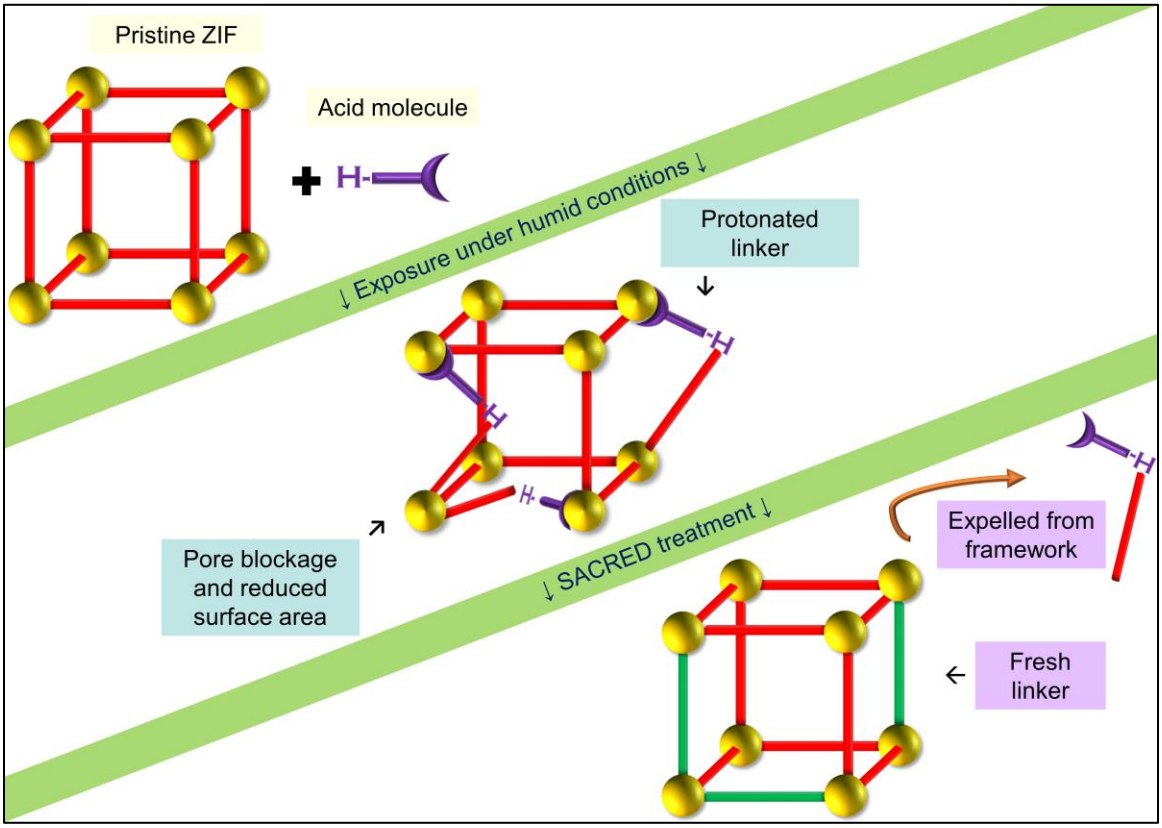

Figure 5.6. Summary of acid-gas degradation and SACRED recovery process in ZIFs

5.4 Conclusions

We have demonstrated a solution-based treatment for the reversal of damage caused to ZIF crystals by exposure to humid acid gas (SO_2). A graphical summary of the degradation process and the recovery treatment is given in Figure 5.6. The Solvent Assisted Crystal Redemption (SACRED) treatment is a quick and relatively inexpensive method to recover the lost surface area, porosity, and crystallinity of degraded ZIF materials. The results presented in this study also challenge the prevailing notion that acid gas induced

damage to ZIF materials are permanent in nature. In ZIF-8, crystals that had lost nearly 100% of surface area and porosity showed almost complete recovery after this treatment. Chemical analysis of the material using FTIR spectroscopy showed that all sulfur-based entities introduced by the acid gas are completely removed by the treatment and the resulting material is chemically identical to pristine ZIF-8. SACRED treatment using isotopically labeled linker molecules was used to elucidate the mechanism of recovery. Fresh linker in the SACRED solution replaces the dangling linker-acid complex and restores the material to its original state. SACRED experiments on ZIF-14 showed that this treatment is not exclusive to ZIF-8, but the narrow pore structure of ZIF-14 resulted in only partial (up to ~ 80%) recovery in surface area and porosity. Recovery was not achieved in ZIF-90 crystals due to possible chemisorption of acid molecules to the carbonyl group on the linker functional group. We propose that the method presented herein can be used to reinstate the properties of both membranes and powders (packed beds, columns) that use ZIF materials that have undergone degradation. The simplicity of this method presents an opportunity to extend it to other MOF systems that have undergone structural degradation. We believe that SACRED treatment can prove useful in reducing the overall material costs in processes involving ZIFs or other MOFs.

CHAPTER 6. CONCLUSIONS AND OUTLOOK

6.1 Conclusions

The overall objective of this thesis has been to investigate the structure and properties of mixed-linker zeolitic imidazolate frameworks. This large extended family of ZIFs offer unique opportunities to tailor materials for energy-efficient molecular separations. A mixed-linker synthesis strategy was adopted to tune the adsorption affinity and pore characteristics of ZIFs. To demonstrate this, mixed-linker ZIF-8-90 materials were synthesized at various linker ratios. Adsorption characterization was performed using gravimetric uptake measurements. These experiments showed that by introducing more ZIF-90 linkers (with aldehyde functional groups) into the matrix, the affinity for water and small alcohols can drastically increase due to hydrogen bonding effects. The introduction of the slightly larger ZIF-90 linker into the pores also contributed to the enlargement of the apertures that resulted in faster diffusion of guest molecules in ZIF-90-rich hybrids. Diffusion measurements were conducted using PFG-NMR and kinetic uptake curves from gravimetric experiments. The increase in diffusivity was more pronounced for larger molecules with sizes approaching the aperture size of the ZIFs. The diffusivities of butanol and isobutanol could be tuned over two orders of magnitude. The ideal diffusion selectivity for water/butanol, water/isobutanol, and butanol/isobutanol binary mixtures also were tunable by over two orders of magnitude. This approach will make it possible to identify the ZIF structure with the ideal pore characteristics for sharp separation of a given molecular pair. Macroscopic evidence for linker mixing in mixed-linker ZIFs was also presented using micro-Raman and powder Raman spectroscopy as well as contrasting the

water adsorption behavior between a true mixed-linker ZIF and physical mixtures of ZIF-8 and ZIF-90.

On the other hand, the microstructure of mixed-linker ZIFs were explored at a unit-cell-level using two-dimensional NMR spectroscopy. Nuclear spin transfer between protons on different functional groups was measured and correlated to the inter-nuclear distances using a simple Fickian model of spin diffusion. The measurements were done using ^{1}H CRAMPS NMR pulse sequence which is an established technique. A detailed model of magnetization transfer was used to quantify the local ordering of linkers. Experimental data was used to generate kinetic rate matrices for all proton-proton spin transfers within the system. These were then used to generate the spin transfer curves for computationally generated mixed-linker ZIF-8-90 structures with varying linker ratios and local ordering. The short-range order of linkers was parametrized using the Warren-Cowley parameter (α). By comparing the experimental and computational spin transfer curves, a 'best-fit' α value for each linker composition was determined. Using this knowledge, a probability distribution for possible pore aperture configurations at different compositions was generated. This method provides a pathway to experimentally characterize mixed-linker MOF structures as well as improve the accuracy of computational models of these materials.

Structural and mechanistic differences of mixed-linker ZIFs made via *de novo* route and solvent assisted linker exchange (SALE) were compared. SALE hybrids result in materials that resemble linear combinations of the parent ZIFs as evidenced from water and nitrogen adsorption experiments. Two dimensional NMR spectroscopy and native-fluorescence confocal microscopy showed that SALE hybrids exist in core-shell

configurations that preserve isolated domains of their parent materials. The mechanism for linker exchange in micro and macroparticles of ZIF-8-90 were seen to be diffusion limited. But SALE at higher temperatures and longer durations was shown to cause morphological defects in the macrocrystals that causes a deviation from the diffusion-limited process. We concluded that SALE can be used as a route for controlled synthesis of core-shell type particles that complement the mixed-linker structures accessible via *de novo* routes.

Our linker exchange studies led to the hypothesis that a similar strategy might be applied to repair ZIF crystals that had undergone degradation. Previous studies in our group had shown that acid-gas induced damage in ZIF crystals originate from the cleavage of the Zn→N coordination bond due to protonation of the linker. By treating the ZIF with a fresh solution of the constituent linker, the porosity, crystallinity, and surface area of acid-gas damaged ZIF materials were recovered. This method, termed solvent assisted crystal redemption (SACRED), introduced fresh linker molecules to replace the old linkers that have been protonated by the acid molecule and completely restores the properties of ZIF-8 to original levels and those of ZIF-14 to nearly 80 percent of the original levels. Using FTIR spectroscopy, it was shown that the chemical identity of the ZIF before degradation and after recovery was identical. Deuterium-substituted linkers and ^{2}H NMR spectroscopy was used to show that the mechanism of SACRED proceeds via full linker replacement and not merely by the removal of the acid molecule due to the basicity of the imidazole linkers. This procedure provides an easy method to salvage ZIF-based membranes and adsorbents after degradation via hazardous molecules and potentially reduce the material costs in ZIF-based separations.

6.2 Outlook and Future Work

Mixed-linker synthesis of MOFs has opened up pathways to achieve continuous tuning of properties like porosity and adsorption affinity. This approach is recommended for designing hybrid MOFs that can carry out separations that are either energy intensive or difficult to accomplish using traditional methods. For example, molecular size-based membrane processes can be used to separate ethanol and water azeotrope with a ZIF with pore size that falls between the kinetic diameters of the two components.

So far, only a very few combinations of mixed-linker ZIFs have been reported that include ZIF-8-90, ZIF-7-8, ZIF-7-90, and ZIF-8-*ambz*. However, there are a number of other ZIFs (e.g. ZIF-71, ZIF-11, ZIF-14, ZIF-65 etc.) that exist in a multitude of topologies (e.g. RHO, ANA, GME etc.) that have not been explored yet. Mixed-linker strategy can be extended to these ZIFs to access pore sizes that are outside of the 3-5 Å range that is possible with the existing combinations. Synthesis strategies that involve mixing two different parent topologies should also be investigated as this opens up new opportunities for pore size and pore environment control. This approach can possibly lead to non-monotonous trends in adsorption and diffusion properties due to the significant differences in the pore structure of the parent materials.

In addition to single component vapor adsorption and diffusion studies, it will be useful to evaluate the performance of mixed-linker ZIFs using multicomponent mixtures that are important from an industrial perspective. For example, ZIF-8-90 hybrids can be useful in butanol/water separations. In comparison to pure ZIF-8, mixed-linker ZIF-8-90 materials have higher pore sizes and hence higher diffusivities for butanol. Having aldehyde functional groups within the framework also improves the alcohol affinity of

these materials at low partial pressures. Therefore, by optimizing these properties, an ideal composition can be identified for concentrating butanol from a dilute mixture of butanol in water. The performance of this material can be evaluated using multicomponent breakthrough experiments in vapor or liquid phase. Multicomponent studies also highlight synergistic and competitive aspects of adsorption and diffusion that are not captured in single component experiments. For example, the water uptake in a hydrophobic material could be enhanced by co-adsorption alongside another guest molecule. Also, weakly binding molecules can be displaced by strongly binding components that will significantly affect the selectivity of the separation. Following up single component analysis with multicomponent studies is critical before recommendations can be made regarding the suitability of a MOF for any separation.

The ^{1}H CRAMPS NMR based technique for structure elucidation of mixed-linker materials offer a straightforward pathway to study the microscopic distribution of linkers within such materials. This approach should be feasible for all materials with different type of protons on each of the functional groups. If the proton spectrum of the MOF is not sufficiently resolved, higher MAS speeds can be implemented along with spin recoupling techniques to counteract the effect of MAS on dipolar coupling. If there are more than two proton species in the system, then selective isotopic labeling can be used to suppress the signal of the additional peaks to improve the resolution of the peaks that are being studied.

In addition to binary mixed-linker materials, this technique can also be extended to ternary and higher hybrids. With the addition of each component, the complexity of the system increases. For example, the ZIF-8-90 system discussed in chapter 3 had a 3x3 rate matrix to describe all the spin transfers happening within the system. If a ZIF-8-71-90

system were synthesized and tested, this would have a 4x4 rate matrix due to the additional proton signal from the 2-position of the imidazole in ZIF-71. But with sufficient signal resolution, such structures can also be fully described using two Warren-Cowley (α) parameters. The relative short range orders α_{AB} and α_{AC} could be independently obtained from the spin transfer curves (while the third pair correlation α_{BC} can be solved from α_{AB} and α_{AC}).

The above method can be used to obtain accurate structures of mixed-linker materials before they can be modeled for adsorption or diffusion studies. Without obtaining the microscopic linker distribution patterns in these materials, an accurate computational recreation of their structures is not possible. Linker clustering can cause effects like percolation pathways that can provide erroneous diffusivity values. There is not enough information available on how the short-range order of linkers affect diffusivities. As we demonstrated in contrasting SALE and *de novo* hybrids, a full kinetic rate based treatment is not required for distinguishing structures that have disorder at length scales significantly higher than unit-cell levels.

In addition to mixed-linker syntheses, this method can also be used to ascertain the distribution of new functional groups introduced by post-synthetic linker modification/functionalization. Usually, these modifications are performed to improve the stability or adsorption capacity of MOFs. In case of partial functionalization, it is not easy to determine if the newly introduced entities are distributed evenly across the framework or limited to segregated domains. Thus, this technique can be helpful to improve the effectiveness of this type of modifications. It can also be used to probe the spatial distribution of other proton-containing species like acid molecules that are introduced into

the crystal. By studying the distribution of acid molecules in the framework, deeper understanding of how acid-gas induced damage in ZIFs is initialized and propagated can be obtained. Solid-state NMR techniques can also be useful in measuring the acid proton concentration in ZIF crystals that cause their degradation due to the pH-dependence of the proton chemical shift.

The Solvent Assisted Linker Exchange (SALE) method can be used to synthesize mixed-linker materials with specific arrangement of linkers. This approach can be used to synthesize MOF membranes with two different MOFs along the thickness of the membrane. Since this method starts with an already synthesized MOF on the membrane whose linkers are partially exchanged, it reduced the chances of forming additional defects on the interface that may be caused by other methods such as epitaxial growth. By sequentially putting MOFs with decreasing pore size along the thickness of the membrane, it may be possible to separate more than one pair of molecules at each stage of the process. In cases where direct membrane synthesis using a MOF is difficult, this method can be used to form a membrane on a support with a facile MOF and then exchange it with the linkers of the difficult-to-attain MOF. Native confocal fluorescence microscopy has proven to be a useful technique to study the microstructure of ZIF materials. This method can be used to study how ZIF crystals undergo compositional or morphological transformations when subjected to physical or chemical treatments. The fluorescence response is triggered by the linker molecule itself and hence can be used to identify local regions where there are anomalies resulting from inhomogeneous distribution of linkers or removal of linkers by chemical reactions. It can also be used to map the distribution of non-linker species within the MOF such as metal nanoparticles, catalysts, or drug molecules encapsulated

within ZIFs. It could also be used to study defect formation and propagation within ZIF crystals as it can provide images from not just the surface but also the inside of the crystal. This method can be used in place of other imaging techniques like TEM that can damage the organic linkers within MOFs.

The Solvent Assisted Crystal Redemption (SACRED) technique provides an easy, inexpensive treatment to recover the properties of certain ZIFs that have been damaged by acid gases. This treatment can be extended towards other MOFs not including ZIFs. In certain cases like DMOFs (which are 2D sheets of metal and benzene-dicarboxylate linkers connected to each other by DABCO linkers), this approach may be useful to understand how the acid-gas attack is propagated. If SACRED treatment using only one type of linker is effective, it may point to only one type of metal-linker bond being affected by the acid-gas. This method can also be extended to membranes. Treatment of membranes and adsorbents using batch or continuous type processes can be explored. Since a large excess of linker is used in the preparation of the SACRED solution, the reusability of this solution for further recovery experiments is an interesting problem. For materials such as ZIF-8 that exhibit ~ 100% recovery, cycling studies can be conducted to learn how many times they can be degraded before the recovery is ineffective. It should also be studied if this process can be carried out in an aqueous solution so that the usage of organic solvents can be minimized.

Based on the observations from SACRED studies, we can hypothesize that the weakening of Zn→N coordination bond by the acid-gas can be exploited to modify otherwise stable ZIF structures. Certain linker exchanges are not feasible due to the higher metal→linker bond strength in the parent structure as compared to the target structures. In

those instances, exposure to acid-gases or other external factors can cleave a certain fraction of these bonds, thereby making them amenable to replacement by fresh linkers. These defective sites can then by repaired using the linker of a new type; effectively performing SALE and SACRED at the same time. This approach can be potentially used to modify MOFs that are otherwise thermodynamically or kinetically unfavorable towards modifications.

APPENDIX A

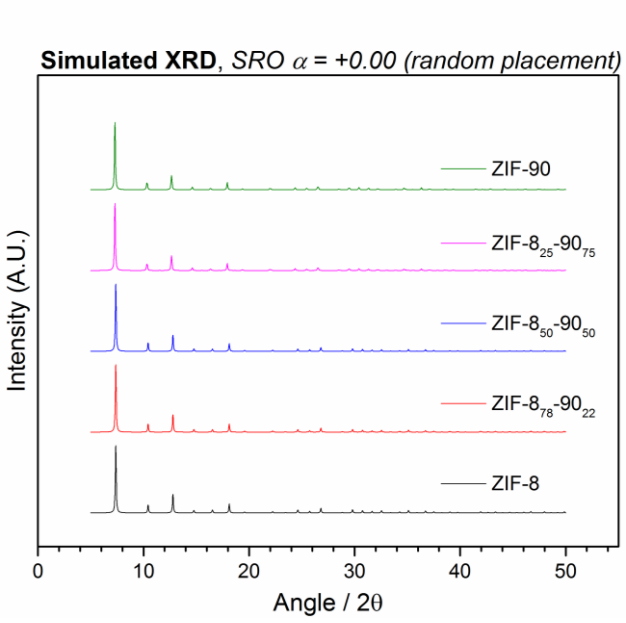

Figure A.1. Simulated XRD patterns for different compositions of ZIF-8-90 materials at short range order of $\alpha = 0$.

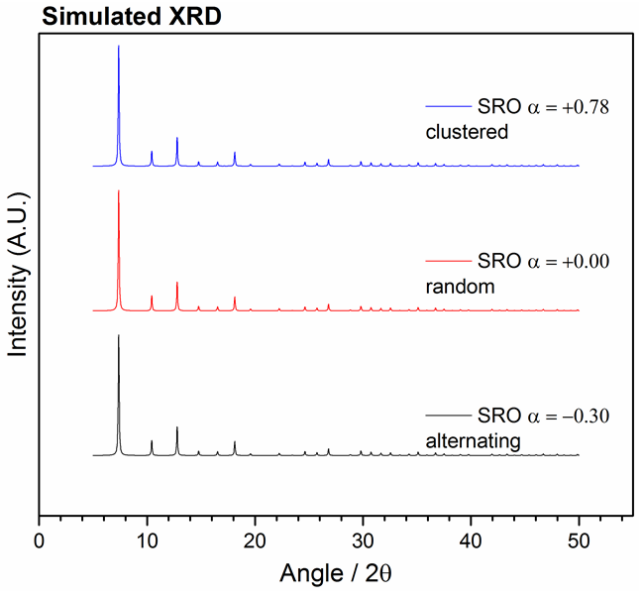

Figure A.2. Simulated XRD patterns of ZIF-8_{50}-90_{50} at different short range order values

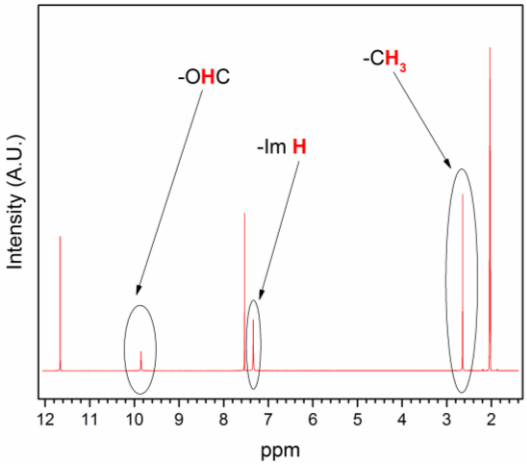

Figure A.3. Solution NMR spectrum for a hybrid ZIF-8_x-90_{100-x} material. Peaks are labelled according to each proton type. Other peaks are from the solvent.

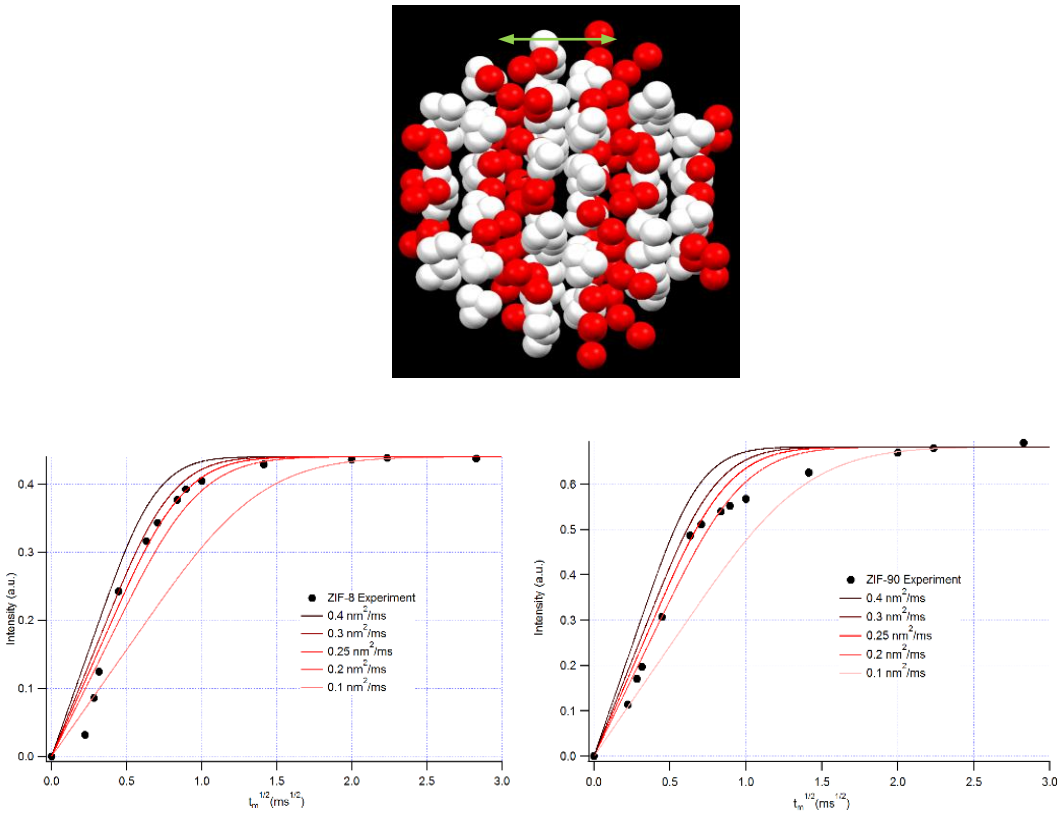

Figure A.4. Schematic of the positions of the protons in the ZIF-8 crystal structure (top). The methyl protons are shown in red, and the imidazole protons are shown in white. ^{1}H

spin diffusion NMR curve for ZIF-8 (bottom left) and ZIF-90 (bottom right) as well as predicted curves using the lamellar morphology for different spin diffusion coefficients.

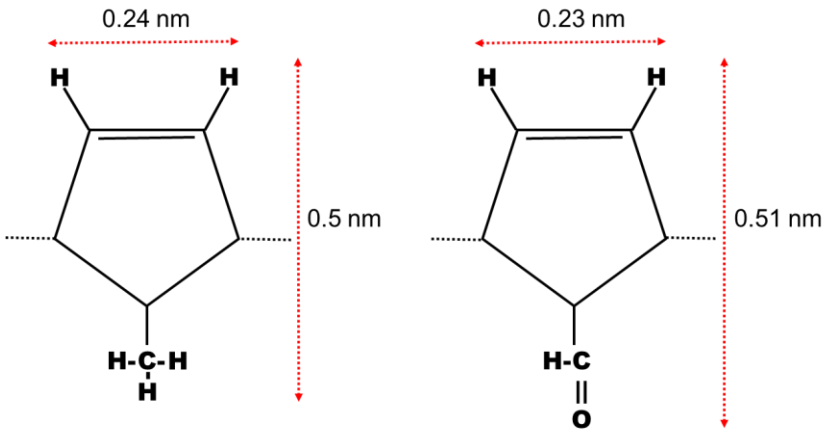

Figure A.5. Representative distances used for calculation of intramolecular spin diffusion domains in ZIF-8 and ZIF-90.

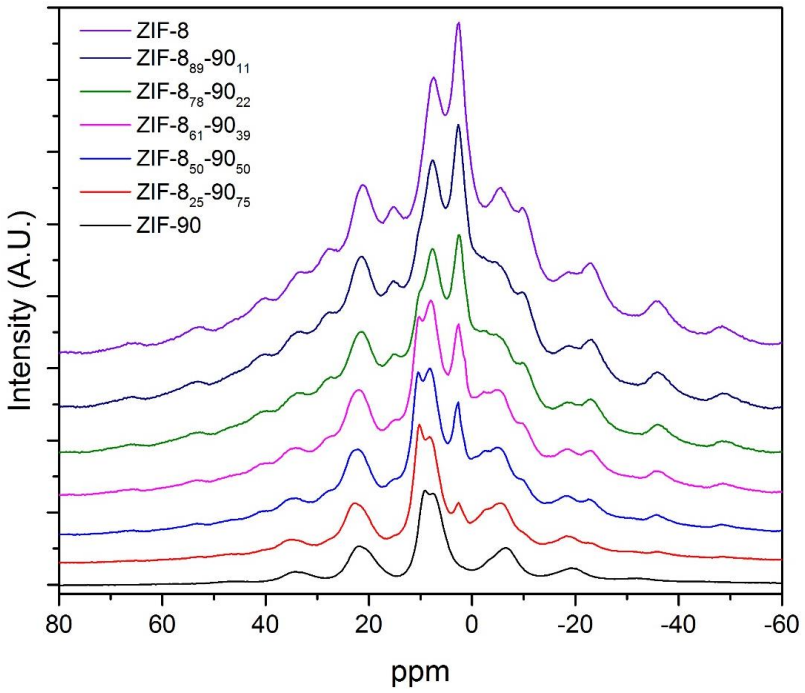

Figure A.6. Single pulse ^{1}H excitation NMR spectra for ZIF-8-90 materials

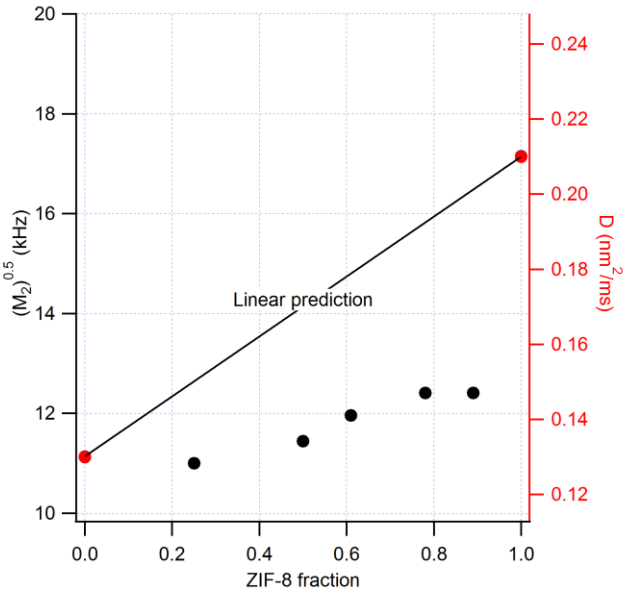

Figure A.7. Second moment of the NMR spectra calculated as a function of linker composition (left) and predicted spin diffusion coefficient as a geometric average of pure components.

Second moment calculation

The second moments of the NMR spectra in Figure A.7 were calculated using the following equations:

$$\sigma^2 = \frac{\left[\Sigma(x-\mu)^2 \times y\right]}{\Sigma(y)}$$
$$\mu = \frac{\Sigma(x \times y)}{\Sigma(y)} \qquad \text{(A.1)}$$

where x and y are the abscissa and ordinate of the NMR spectra.

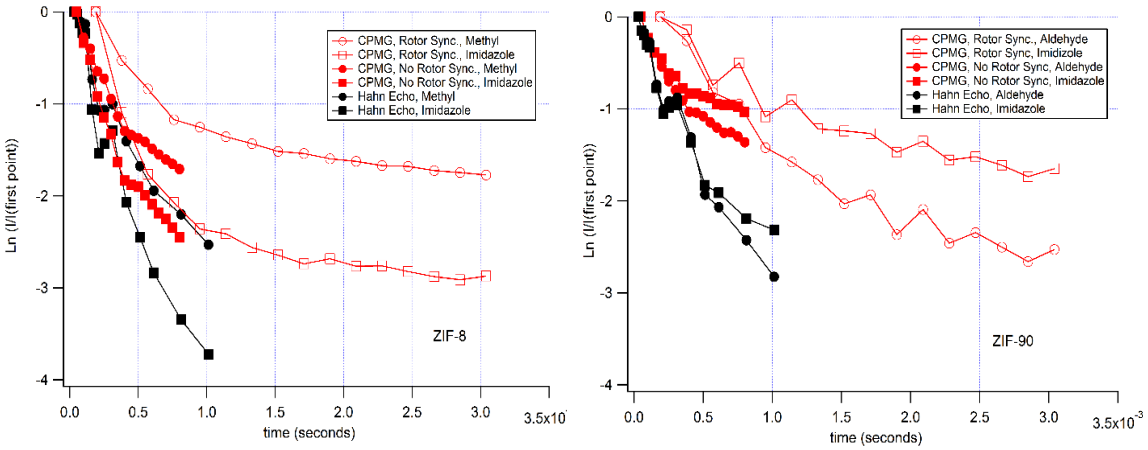

Figure A.8. T_2 curves of ZIF-8 (left) and ZIF-90 (right) using Hahn Echo and CPMG (with rotor synchronization and without rotor synchronization).

Note that the T_2 curves shown in Figure A.8 are calculated from the center peaks only. These are the longest possible T_2 values. A more robust approximation of T_2 can be obtained from the second moment calculation in Figure A.7 since it takes into account all the side-band peaks as well.

Modeling of ^{1}H CRAMPS NMR Intensity Curves

Here we summarize the derivation as given by Perrin and Dwyer[129] as well as Elena and Emsley[60] for modeling the relaxation of z (longitudinal)-magnetization back to its equilibrium value during the mixing time period of an NMR experiment. The following system of coupled differential equations can be used to model the relaxation:

$$\begin{aligned}
\frac{dm_1}{dt} &= -(\mathrm{T}_{1,1}^{-1} + \sum_l k_{1l})\,\mathrm{m}_1 + k_{21}m_2 + \ldots + k_{N2}m_N \\
\frac{dm_2}{dt} &= k_{12}m_1 - (\mathrm{T}_{1,2}^{-1} + \sum_l k_{2l})\,\mathrm{m}_2 + \ldots + k_{N2}m_N \\
\frac{dm_N}{dt} &= k_{1N}m_1 + \ldots + k_{2N}m_2 + \ldots - (\mathrm{T}_{1,N}^{-1} + \sum_l k_{Nl})\,\mathrm{m}_N
\end{aligned} \qquad \text{(A.2)}$$

where N is the total number of spin types (e.g. N=2 for ZIF-8), m_N is the deviation of the z-magnetization away from its equilibrium value, $T_{1,N}$ is the spin lattice relation and k_{ij} is the rate constant for exhchange from spin site i to spin site j. We assume that spin lattice relaxation happens on time scales much greater than mixing times for this analysis. The coupled first order differential equations are then reduced into the following form:

$$\frac{dm}{dt} = -Rm \tag{A.3}$$

where *m* is an Nx1 vector of z-magnetizations and *R* is an NxN matrix of rate constants of spin transfer. The solution to this first order differential equation through a matrix exponential is given by:

$$\boldsymbol{m(t_m) = e^{-Rt_m} m(0)} \tag{A.4}$$

where t_m is the mixing time. By including the initial condition of the deviation of magnetization from its equilibrium value and assuming conservation of magnetization, the cross and diagonal peak intensities follow as:

$$I_{ij}(t_m) = M_z^{j,0}(\mathrm{e}^{-Rt_m})_{ij} \tag{A.5}$$

where $M_z^{j,0}$ are the intial z-magnetization values and I_{ij} are the intensity values corresponding to the NMR diagonal and cross peak volumes. Cross-terms are calculated using the following formulation:

$$k_{ij} = A\frac{1}{N_i}\left\langle \sum_{l=1}^{N_j} \frac{1}{r_{kl}^n} \right\rangle_{k=1,2...,N_i} \tag{A.6}$$

where A is a fitting parameter with units of m^6/s, N_i, N_j are the number of hydrogens with spin type i,j, r_{kl} is the distance between hydrogen k (source: spin type i) and hydrogen l (sink: spin type j), n is the power scaling of the distance (n=6), and the average is taken over all hydrogen k's with spin type i in an effort to include thermal fluctuations. This averaging can be ingored if a crystal cell with uniform spacing of hydrogens is observed. The Levenberg-Marquardt least squares fitting routine as implemented in the LMFIT Python model was used to determine the A parameter for the pure materials. Diagonal rate constants are calculated as:

$$k_{ii} = -\sum_{\substack{j\neq i}}^{\substack{\#\ j\\ spins}} k_{ij} \tag{A.7}$$

As a self-consistency check, the forward and reverse rates must satisfy detailed balance:

$$k_{ij}\, p_i = k_{ji}\, p_j \tag{A.8}$$

where p_i and p_j are relative populations of spin type i,j.

Pure ZIF-90 Spin Exchange Fitting Results

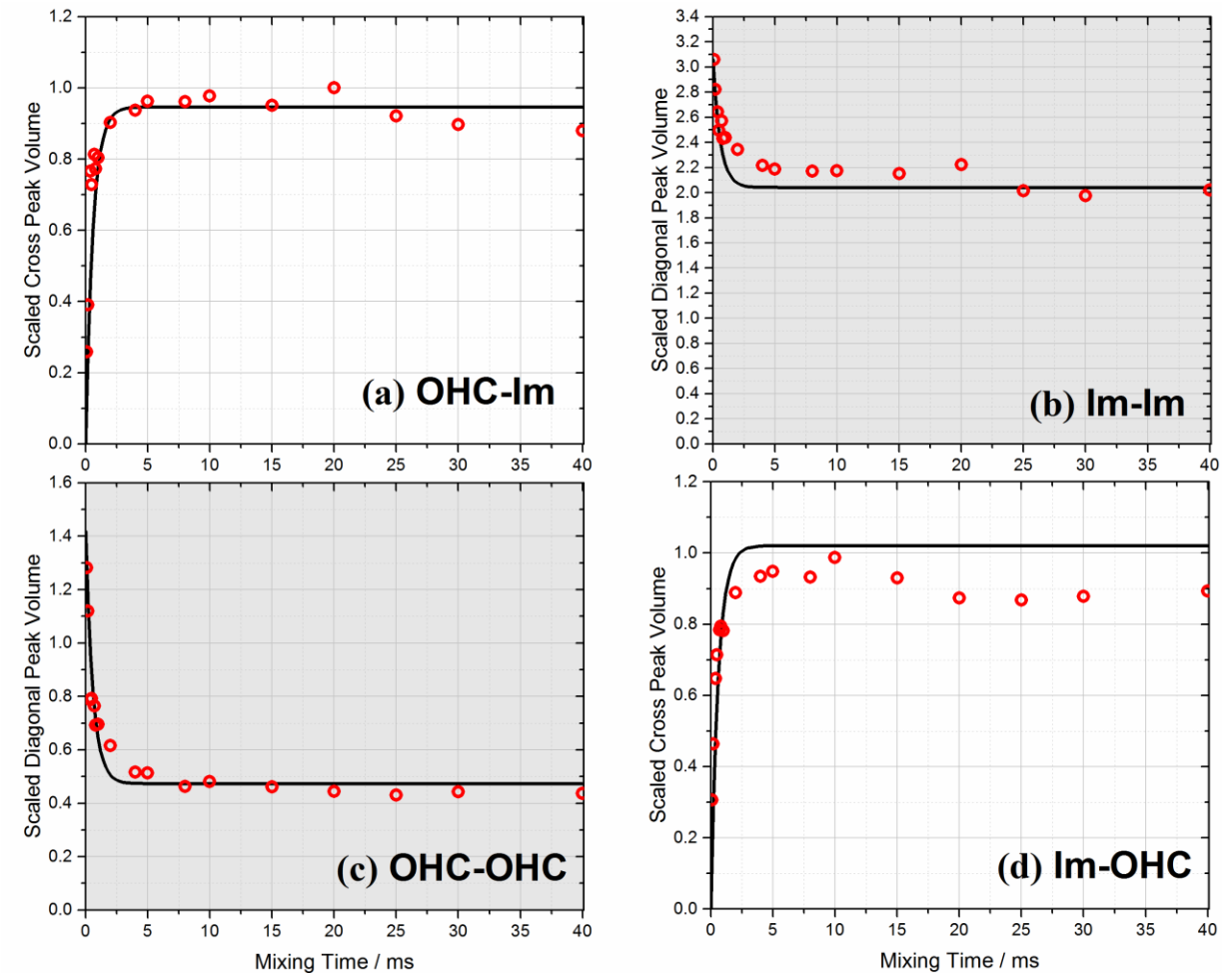

Figure A.9. Pure ZIF-90 fitting results, with model fits given by the solid black lines and experimental NMR data in the open red circles.

Figure A.8 shows the mean absolute error as a function of SRO. Three experiments of ZIF-8_{50}-90_{50} (label A, B, C) were done, each yielding the same minimum SRO value/range. Table S4 gives a complete summary of all the fitting parameters and results of the pure and hybrid ZIF materials.

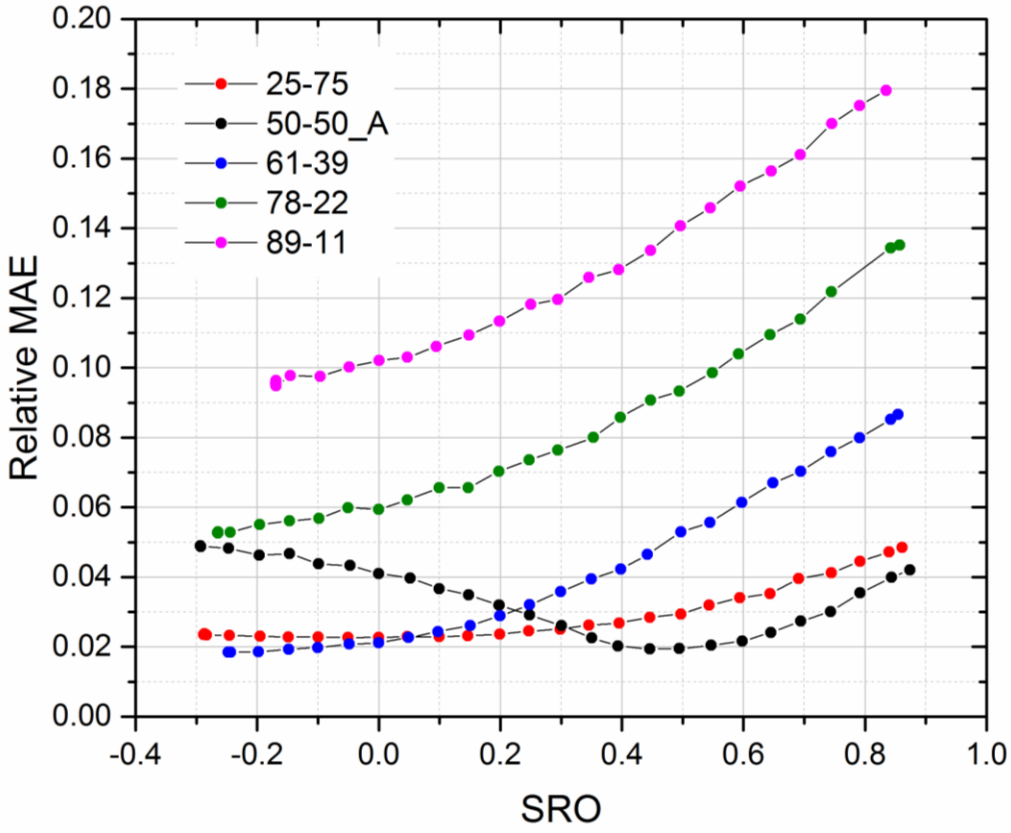

Figure A.10. Relative mean absolute error (MAE) as a function of SRO for five ZIF-8-90 hybrid materials.

Table A.1. Summary of fitting results detailing starting unit cell, *A* value, scaled initial z-magnetization values, and final short range orders for different ZIF-8-90 hybrids.

Sample	**Starting Unit Cell**	**A**	$M_z^{\mathrm{Im},0}$	$M_z^{\mathrm{OHC},0}$	$M_z^{\mathrm{CH3},0}$	**SRO α [range]**
ZIF-8$_{100}$-90$_0$	ZIF-8	(101.8±5.7)*	1.875	-	2.212	-
ZIF-8$_0$-90$_{100}$	ZIF-90	(120.7±8.1)*	3.061	1.420	-	-
ZIF-8$_{25}$-90$_{75}$	ZIF-90	115.6	0.660	0.205	0.085	**0.00, [-0.29,+0.20]**
ZIF-8$_{50}$-90$_{50}^{A}$	ZIF-8	110.8	0.665	0.104	0.311	**+0.45, [+0.40,+0.55]**
ZIF-8$_{50}$-90$_{50}^{B}$	ZIF-8	110.8	0.660	0.103	0.304	**+0.45, [+0.40,+0.50]**
ZIF-8$_{50}$-90$_{50}^{C}$	ZIF-8	110.8	0.651	0.103	0.302	**+0.45, [+0.40,+0.55]**
ZIF-8$_{61}$-90$_{39}$	ZIF-8	108.8	0.644	0.063	0.451	**-0.25, [-0.25,-0.15]**

ZIF-8_{78}-90_{22}	ZIF-8	105.7	0.558	0.001	0.569	**-0.26, [-0.26,-0.20]**
ZIF-8_{89}-90_{11}	ZIF-8	103.7	0.604	0.000	0.696	**-0.17, [-0.17,-0.05]**

*These *A* parameter values were determined through the fitting procedure of the pure ZIF data and used to calculate the A parameter values for the hybrid ZIF materials; [A,B,C]Three different ZIF-8_{50}-90_{50} experiments, each yielding the same SRO.

APPENDIX B

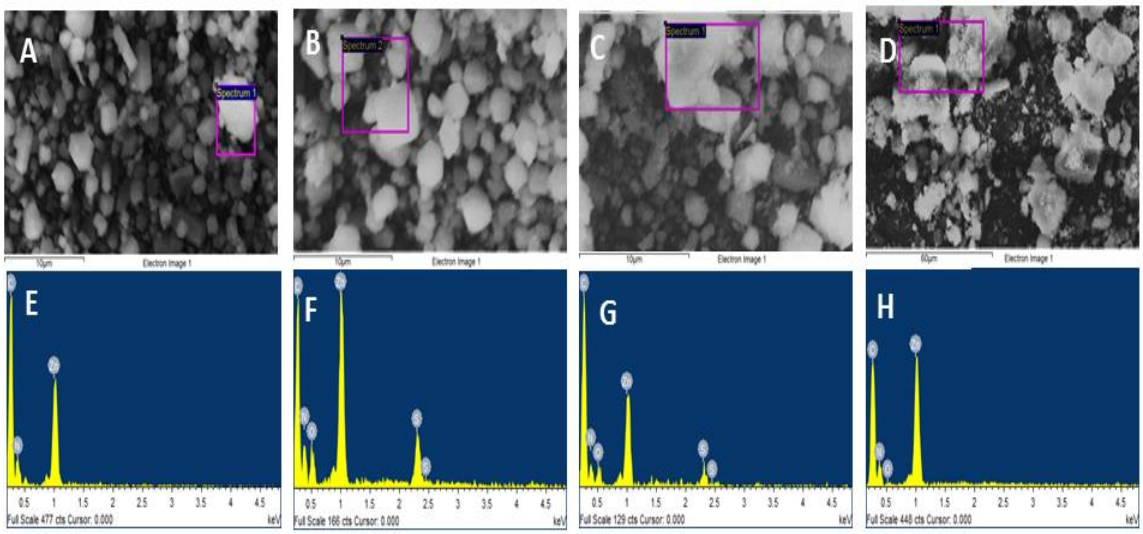

Figure B.1. EDX micrographs (A-D) and elemental analysis plots (E-H) of pristine ZIF-8, ZIF-8 before and after reactivation following humid SO_2 exposure and ZIF-8 recovery via SACRED treatment.

REFERENCES

1. Energy consumption estimates by sector. www.eia.gov (accessed 2017).

2. Sholl, D. S.; Lively, R., *Nature* **2016,** *532*.

3. *Materials for Separation Technologies: Energy and Emission Reduction Opportunities*; Oak Ridge National Laboratory: 2005.

4. Bozell, J. J.; Petersen, G. R., *Green Chem.* **2010,** *12*.

5. Long, J. R.; Yaghi, O. K., *Chem. Soc. Rev.* **2009,** *38*.

6. Zhou, H.-C.; Kitagawa, S., *Chem. Soc. Rev.* **2014,** *43*.

7. Farha, O. K.; Eryazici, I.; Jeong, N. C.; Hauser, B. G.; Wilmer, C. E.; Sarjeant, A. A.; Snurr, R. Q.; Nguyen, S. T.; Yazaydın, A. Ö.; Hupp, J. T., *J. Am. Chem. Soc.* **2012,** *134*.

8. Zhang, C.; Koros, W. J., *J. Phys. Chem. Lett.* **2015,** *6*, 3841.

9. Liu, S.; Liu, G.; Zhao, X.; Jin, W., *J. Membr. Sci.* **2013,** *446*.

10. Krishna, R., *RSC Adv.* **2015,** *5*.

11. Zhang, K.; Lively, R. P.; Dose, M. E.; Brown, A. J.; Zhang, C.; Chung, J.; Nair, S.; Koros, W. J.; Chance, R. R., *Chem. Commun.* **2013,** *49*.

12. Deria, P.; Mondloch, J. E.; Karagiaridi, O.; Bury, W.; Hupp, J. T.; Farha, O. K., *Chem. Soc. Rev.* **2014,** *43*.

13. Qiu, S.; Xue, M.; Zhu, G., *Chem. Soc. Rev.* **2014,** *43*.

14. Tanh Jeazet, H. B.; Staudt, C.; Janiak, C., *Dalton Trans.* **2012,** *41*.

15. Brown, A. J.; Johnson, J. R.; Lydon, M. E.; Koros, W. J.; Jones, C. W.; Nair, S., *Angew. Chem.* **2012,** *124*.

16. Brown, A. J.; Brunelli, N. A.; Eum, K.; Rashidi, F.; Johnson, J. R.; Koros, W. J.; Jones, C. W.; Nair, S., *Science* **2014,** *345*, 72.

17. Park, K. S.; Ni, Z.; Cote, A. P.; Choi, J. Y.; Huang, R.; Uribe-Romo, F. J.; Chae, H. K.; O'Keeffe, M.; Yaghi, O. M., *Proc. Natl. Acad. Sci. U. S. A.* **2006,** *103*, 10186.

18. Bux, H.; Liang, F.-Y.; Li, Y.-S.; Cravillon, J.; Wiebcke, M.; Caro, J., *J. Am. Chem. Soc.* **2009,** *131*.

19. Phan, A.; Doonan, C. J.; Uribe-Romo, F. J.; Knobler, C. B.; O'Keeffe, M.; Yaghi, O. M., *Acc. Chem. Res.* **2009,** *43,* 58.

20. Hara, N.; Yoshimune, M.; Negishi, H.; Haraya, K.; Hara, S.; Yamaguchi, T., *J. Membr. Sci.* **2014,** *450,* 215.

21. Pan, Y.; Li, T.; Lestari, G.; Lai, Z., *J. Membr. Sci.* **2012,** *390–391*.

22. Bux, H.; Chmelik, C.; Krishna, R.; Caro, J., *J. Membr. Sci.* **2011,** *369*.

23. Bux, H.; Feldhoff, A.; Cravillon, J.; Wiebcke, M.; Li, Y.-S.; Caro, J., *Chem. Mater.* **2011,** *23*.

24. Zhang, C.; Dai, Y.; Johnson, J. R.; Karvan, O.; Koros, W. J., *Journal of Membrane Science* **2012,** *389*.

25. Pan, Y.; Lai, Z., *Chemical Communications* **2011,** *47*.

26. Wu, T.; Feng, X.; Elsaidi, S. K.; Thallapally, P. K.; Carreon, M. A., *Ind. Eng. Chem. Res.* **2017**.

27. Remi, J. C. S.; Remy, T.; Hunskerken, V. V.; Perre, S. v. d.; Duerinck, T.; Maes, M.; Vos, D. D.; Gobechiya, E.; Kirschhock, C. E. A.; Baron, G. V.; Denayer, J. F. M., *ChemSusChem* **2011,** *4*.

28. Bai, Y.; Dong, L.; Zhang, C.; Gu, J.; Sun, Y.; Zhang, L.; Chen, H., *Sep. Sci. Technol.* **2013,** *48*.

29. Li, Y.; Liang, F.; Bux, H.; Yang, W.; Caro, J., *J. Membr. Sci.* **2010,** *354*.

30. Dong, X.; Lin, Y. S., *Chem. Commun.* **2013,** *49,* 1196.

31. Eum, K.; Rownaghi, A.; Choi, D.; Bhave, R. R.; Jones, C. W.; Nair, S., *Adv. Funct. Mater.* **2016,** *26,* 5011.

32. Zhang, C.; Lively, R. P.; Zhang, K.; Johnson, J. R.; Karvan, O.; Koros, W. J., *J. Phys. Chem. Lett.* **2012,** *3,* 2130.

33. Peralta, D.; Chaplais, G.; Paillaud, J.-L.; Simon-Masseron, A.; Barthelet, K.; Pirngruber, G. D., *Microporous Mesoporous Mater.* **2013,** *172*.

34. Zhang, K.; Lively, R. P.; Zhang, C.; Chance, R. R.; Koros, W. J.; Sholl, D. S.; Nair, S., *J. Phys. Chem. Lett.* **2013,** *4*.

35. Gee, J. A.; Chung, J.; Nair, S.; Sholl, D. S., *J. Phys. Chem. C* **2013,** *117*.

36. Zhang, K.; Zhang, L.; Jiang, J., *Journal of Physical Chemistry C* **2013,** *117*.

37. Lively, R. P.; Dose, M. E.; Thompson, J. A.; McCool, B. A.; Chance, R. R.; Koros, W. J., *Chem. Commun.* **2011,** *47*.

38. Deng, H.; Doonan, C. J.; Furukawa, H.; Ferreira, R. B.; Towne, J.; Knobler, C. B.; Wang, B.; Yaghi, O. M., *Science* **2010,** *327*, 846.

39. Zhang, Y.-B.; Furukawa, H.; Ko, N.; Nie, W.; Park, H. J.; Okajima, S.; Cordova, K. E.; Deng, H.; Kim, J.; Yaghi, O. M., *J. Am. Chem. Soc.* **2015,** *137*.

40. Thompson, J. A.; Blad, C. R.; Brunelli, N. A.; Lydon, M. E.; Lively, R. P.; Jones, C. W.; Nair, S., *Chem. Mater.* **2012,** *24*, 1930.

41. Wang, Z.; Cohen, S. M., *Chem. Soc. Rev.* **2009,** *38*, 1315.

42. Thompson, J. A.; Brunelli, N. A.; Lively, R. P.; Johnson, J. R.; Jones, C. W.; Nair, S., *J. Phys. Chem. C* **2013,** *117*.

43. Thompson, J. A.; Vaughn, J. T.; Brunelli, N. A.; Koros, W. J.; Jones, C. W.; Nair, S., *Microporous Mesoporous Mater.* **2014,** *192*, 43.

44. Rashidi, F.; Blad, C. R.; Jones, C. W.; Nair, S., *AIChE J.* **2016,** *62*, 525.

45. Kärger, J.; Ruthven, D. M.; Theodorou, D. N., *Diffusion in Nanoporous Materials*. Wiley: 2012.

46. Sholl, D. S., *Acc. Chem. Res.* **2006,** *39*.

47. Karger, J.; Caro, J., *J. Chem. Soc., Faraday Trans.* **1977**.

48. Pampel, A.; Fernandez, M.; Freude, D.; Karger, J., *Chem. Phys. Lett.* **2005,** *407*.

49. Karger, J.; Ruthven, D. M., *New J. Chem.* **2016**.

50. Tanner, J. E.; Stejskal, E. O., *J. Chem. Phys.* **1968,** *49*.

51. Stallmach, F.; Karger, J.; Pfeifer, H., *J. Magn. Reson.* **1993,** *102*.

52. McDaniel, P. L.; Coe, C. G.; Karger, J.; Moyer, J. D., *J. Phys. Chem.* **1996,** *100*.

53. Karger, J.; Stallmach, F.; Feoktistova, N. N.; Zhdanov, S. P., *Zeolites* **1993,** *13*.

54. Chmelik, C.; Bux, H.; Caro, J.; Heinke, L.; Hibbe, F.; Titze, T.; Kärger, J., *Phys. Rev. Lett.* **2010,** *104*.

55. Koh, K.; Wong-Foy, A. G.; Matzger, A. J., *Chem. Commun.* **2009,** *41*.

56. Clauss, J.; Schmidt-Rohr, K.; Spiess, H. W., *Acta Polymer.* **1993,** *44*, 1.

57. Jia, X.; Wolak, J.; Wang, X.; White, J. L., *Macromolecules* **2003,** *36,* 712.

58. Nieuwendaal, R. C.; Snyder, C. R.; Kline, R. J.; Lin, E. K.; VanderHart, D. L.; DeLongchamp, D. M., *Chem. Mater.* **2010,** *22,* 2930.

59. Nieuwendaal, R. C.; Ro, H. W.; Germack, D. S.; Kline, R. J.; Toney, M. F.; Chan, C. K.; Agrawal, A.; Gundlach, D.; VanderHart, D. L.; Delongchamp, D. M., *Adv. Funct. Mater.* **2012,** *22,* 1255.

60. Elena, B.; Emsley, L., *J. Am. Chem. Soc.* **2005,** *127*.

61. Elena, B.; Pintacuda, G.; Mifsud, N.; Emsley, L., *J. Am. Chem. Soc.* **2006,** *128*.

62. Kong, X.; Deng, H.; Yan, F.; Kim, J.; Swisher, J. A.; Smith, B.; Yaghi, O. M.; Reimer, J. A., *Science* **2013,** *341,* 882.

63. Krajnc, A.; Kos, T.; Zabukovec Logar, N.; Mali, G., *Angew. Chem. Int. Ed* **2015,** *54,* 10535.

64. Baias, M.; Lesage, A.; Aguado, S.; Canivet, J.; Moizan-Basle, V.; Audebrand, N.; Farrusseng, D.; Emsley, L., *Angew. Chem. Int. Ed* **2015,** *54*.

65. Burnett, B. J.; Barron, P. M.; Hu, C.; Choe, W., *J. Am. Chem. Soc.* **2011,** *133,* 9984.

66. Kim, M.; Cahill, J. F.; Fei, H.; Prather, K. A.; Cohen, S. M., *J. Am. Chem. Soc.* **2012,** *134,* 18082.

67. Kim, M.; Cahill, J. F.; Su, Y.; Prather, K. A.; Cohen, S. M., *Chem.Sci* **2012,** *3*.

68. Karagiaridi, O.; Bury, W.; Sarjeant, A. A.; Stern, C. L.; Farha, O. K.; Hupp, J. T., *Chem. Sci.* **2012,** *3,* 3256.

69. Li, T.; Kozlowski, M. T.; Doud, E. A.; Blakely, M. N.; Rosi, N. L., *J. Am. Chem. Soc.* **2013,** *135,* 11688.

70. Karagiaridi, O.; Bury, W.; Mondloch, J. E.; Hupp, J. T.; Farha, O. K., *Angew. Chem. Int. Ed* **2014,** *53,* 4530.

71. Burtch, N. C.; Jasuja, H.; Walton, K. S., *Chem. Rev.* **2014,** *114*.

72. Bhattacharyya, S.; Pang, S. H.; Dutzer, M. R.; Lively, R. P.; Walton, K. S.; Sholl, D. S.; Nair, S., *J. Phys. Chem. C* **2016**.

73. Kang, I. J.; Khan, N. A.; Haque, E.; Jhung, S. H., *Chem. - Eur. J.* **2011,** *17*.

74. Wu, T.; Shen, L.; Luebbers, M.; Hu, C.; Chen, Q.; Ni, Z.; Masel, R. I., *Chem. Commun.* **2010,** *46*.

75. Ma, D.; Li, Y.; Li, Z., *Chem. Commun.* **2011,** *47*.

76. Bux, H.; Feldhoff, A.; Cravillon, J.; Wiebcke, M.; Li, Y.-S.; Caro, J., *Chemistry of Materials* **2011,** *23*.

77. Farha, O. K.; Özgür Yazaydın, A.; Eryazici, I.; Malliakas, C. D.; Hauser, B. G.; Kanatzidis, M. G.; Nguyen, S. T.; Snurr, R. Q.; Hupp, J. T., *Nat Chem* **2010,** *2*.

78. Demessence, A.; D'Alessandro, D. M.; Foo, M. L.; Long, J. R., *Journal of the American Chemical Society* **2009,** *131*.

79. Cohen, S. M., *Chemical Reviews* **2011,** *112*.

80. Pan, L.; Olson, D. H.; Ciemnolonski, L. R.; Heddy, R.; Li, J., *Angewandte Chemie* **2006,** *118*.

81. Getman, R. B.; Bae, Y.-S.; Wilmer, C. E.; Snurr, R. Q., *Chemical reviews* **2011,** *112*.

82. Kwon, H. T.; Jeong, H.-K., *J. Am. Chem. Soc.* **2013,** *135*, 10763.

83. Liu, D.; Ma, X.; Xi, H.; Lin, Y. S., *Journal of Membrane Science* **2014,** *451*.

84. Banerjee, R.; Phan, A.; Wang, B.; Knobler, C. B.; Furukawa, H.; O'Keeffe, M.; Yaghi, O. M., *Science* **2008,** *319*.

85. Li, J.-R.; Kuppler, R. J.; Zhou, H.-C., *Chem. Soc. Rev.* **2009,** *38*.

86. Li, J.-R.; Ma, Y.; McCarthy, M. C.; Sculley, J.; Yu, J.; Jeong, H.-K.; Balbuena, P. B.; Zhou, H.-C., *Coord. Chem. Rev.* **2011,** *255*, 1791.

87. Thompson, J. A.; Blad, C. R.; Brunelli, N. A.; Lydon, M. E.; Lively, R. P.; Jones, C. W.; Nair, S., *Chemistry of Materials* **2012,** *24*.

88. Qiu, S.; Xue, M.; Zhu, G., *Chemical Society Reviews* **2014**.

89. Pan, Y.; Li, T.; Lestari, G.; Lai, Z., *Journal of Membrane Science* **2012,** *390–391*.

90. Shah, M.; McCarthy, M. C.; Sachdeva, S.; Lee, A. K.; Jeong, H.-K., *Industrial & Engineering Chemistry Research* **2011,** *51*.

91. Krishna, R., *Chemical Society Reviews* **2012,** *41*.

92. Zhang, K.; Lively, R. P.; Zhang, C.; Koros, W. J.; Chance, R. R., *J. Phys. Chem. C* **2013,** *117*.

93. Thompson, J. A.; Brunelli, N. A.; Lively, R. P.; Johnson, J. R.; Jones, C. W.; Nair, S., *The Journal of Physical Chemistry C* **2013,** *117*.

94. Cravillon, J.; Schroder, C. A.; Bux, H.; Rothkirch, A.; Caro, J.; Wiebcke, M., *CrystEngComm* **2012,** *14*.

95. Hill, A. E.; Malisoff, W. M., *Journal of the American Chemical Society* **1926,** *48*.

96. Kumar, M.; Gayen, K., *Applied Energy* **2011,** *88*.

97. Qin, F.; Li, S.; Qin, P.; Karim, M. N.; Tan, T., *Green Chemistry* **2014**.

98. Fairen-Jimenez, D.; Moggach, S. A.; Wharmby, M. T.; Wright, P. A.; Parsons, S.; Duren, T., *Journal of the American Chemical Society* **2011,** *133*.

99. Pera-Titus, M.; Farrusseng, D., *Journal of Physical Chemistry C* **2012,** *116*.

100. Nalaparaju, A.; Zhao, X. S.; Jiang, J. W., *Journal of Physical Chemistry C* **2010,** *114*.

101. Callaghan, P. T., *Translational dynamics and magnetic resonance: Principles of pulsed gradient spin echo NMR*. Oxford University Press: Oxford, UK, 2011.

102. Karger, J.; Ruthven, D. M.; Theodorou, D., Metal Organic Frameworks. In *Diffusion in Nanoporous Materials*, Wiley VCH: 2012; Vol. 2, pp 739-744.

103. Stallmach, F.; Gröger, S.; Künzel, V.; Kärger, J.; Yaghi, O. M.; Hesse, M.; Müller, U., *Angewandte Chemie International Edition* **2006,** *45*.

104. Eum, K.; Jayachandrababu, K. C.; Rashidi, F.; Zhang, K.; Leisen, J.; Graham, S.; Lively, R. P.; Chance, R. R.; Sholl, D. S.; Jones, C. W.; Nair, S., *J. Am. Chem. Soc.* **2015,** *137*, 4191.

105. Wu, Y.; Chen, H.; Liu, D.; Qian, Y.; Xi, H., *Chem. Eng. Sci.* **2015,** *124*.

106. Thornton, A. W.; Dubbeldam, D.; Liu, M. S.; Ladewig, B. P.; Hill, A. J.; Hill, M. R., *Energy Environ. Sci.* **2012,** *5*, 7637.

107. Liu, B.; Smit, B., *J. Phys. Chem. C* **2010,** *114*.

108. Liu, J.; Keskin, S.; Sholl, D. S.; Johnson, J. K., *J. Phys. Chem. C* **2011,** *115*.

109. Haldoupis, E.; Watanabe, T.; Nair, S.; Sholl, D. S., *ChemPhysChem* **2012,** *13*.

110. Mellinger, F.; Wilhelm, M.; Spiess, H. W., *Macromolecules* **1999,** *32*.

111. Schmidt-Rohr, K.; Spiess, H. W., *Multidimensional solid-state NMR and polymers*. Academic Press: 1994.

112. Rossini, A. J.; Zagdoun, A.; Lelli, M.; Canivet, J.; Aguado, S.; Ouari, O.; Tordo, P.; Rosay, M.; Maas, W. E.; Copéret, C.; Farrusseng, D.; Emsley, L.; Lesage, A., *Angew. Chem.* **2012,** *124*.

113. Kamakoti, P.; Sholl, D. S., *Phys. Rev. B* **2005,** *71*, 014301 1.

114. Lee, M.; Goldburg, W. I., *Phys. Rev.* **1965,** *140*, A1261.

115. Leskes, M.; Madhu, P. K.; Vega, S., *Chem. Phys. Lett.* **2007,** *447*, 370.

116. Coelho, C.; Rocha, J.; Madhu, P. K.; Mafra, L., *J. Magn. Reson.* **2008,** *194*.

117. Nieuwendaal, R. C., *Solid State Nucl. Magn. Reson.* **2016,** *76–77*.

118. Morris, W.; Doonan, C. J.; Furukawa, H.; Banerjee, R.; Yaghi, O. M., *J. Am. Chem. Soc.* **2008,** *130*.

119. Allen, F., *Acta Crystallogr. Sect. B: Struct. Sci.* **2002,** *58*.

120. Kresse, G.; Furthmüller, J., *Phys. Rev. B* **1996,** *54*.

121. Sholl, D. S.; Steckel, J. A., *Density Functional Theory: A Practical Introduction*. John Wiley & Sons, Inc.: Hoboken, NJ, 2009.

122. Perdew, J. P.; Burke, K.; Ernzerhof, M., *Phys. Rev. Lett.* **1996,** *77*.

123. Grimme, S., *J. Comput. Chem.* **2006,** *27*.

124. Newman, M. E. J.; Ziff, R. M., *Phys. Rev. E.* **2001,** *64*.

125. Macrae, C. F.; Bruno, I. J.; Chisholm, J. A.; Edgington, P. R.; McCabe, P.; Pidcock, E.; Rodriguez-Monge, L.; Taylor, R.; van de Streek, J.; Wood, P. A., *J. Appl. Crystallogr.* **2008,** *41*.

126. Macrae, C. F.; Edgington, P. R.; McCabe, P.; Pidcock, E.; Shields, G. P.; Taylor, R.; Towler, M.; van de Streek, J., *J. Appl. Crystallogr.* **2006,** *39*.

127. Bruno, I. J.; Cole, J. C.; Edgington, P. R.; Kessler, M.; Macrae, C. F.; McCabe, P.; Pearson, J.; Taylor, R., *Acta Crystallographica Section B: Structural Science* **2002,** *58*.

128. Taylor, R.; Macrae, C. F., *Acta Crystallographica Section B: Structural Science* **2001,** *57*.

129. Perrin, C. L.; Dwyer, T. J., *Chem. Rev.* **1990,** *90*.

130. Suter, D.; Ernst, R. R., *Phys. Rev. B* **1985,** *32*.

131. Henrichs, P. M.; Linder, M.; Hewitt, J. M., *J. Chem. Phys.* **1986,** *85*.

132. Kubo, A.; McDowell, C. A., *J. Chem. Soc., Faraday Trans. 1* **1988,** *84*.

133. VanderHart, D. L.; McFadden, G. B., *Solid State Nucl. Magn. Reson.* **1996,** *7*.

134. Spiegel, S.; Schmidt-Rohr, K.; Boeffel, C.; Spiess, H. W., *Polymer* **1993,** *34*.

135. Willems, T. F.; Rycroft, C. H.; Kazi, M.; Meza, J. C.; Haranczyk, M., *Microporous Mesoporous Mater.* **2012,** *149*.

136. Chen, Q.; Schmidt-Rohr, K., *Solid State Nucl. Magn. Reson.* **2006,** *29*.

137. Kidron, A., *Phys. Lett.* **1967,** *25A*.

138. Tanabe, K. K.; Cohen, S. M., *Chem. Soc. Rev.* **2011,** *40*, 498.

139. Cohen, S. M., *Chem. Rev.* **2011,** *112*, 970.

140. Ni, Z.; Afeworki, M.; Weston, S. C.; Zengel, J.; Stern, D. L. Linker exchange in zeolitic imidazolate frameworks. US 8,920,541 B2, Dec. 30, 2014.

141. Deria, P.; Mondloch, J. E.; Tylianakis, E.; Ghosh, P.; Bury, W.; Snurr, R. Q.; Hupp, J. T.; Farha, O. K., *J. Am. Chem. Soc.* **2013,** *135*, 16801.

142. Deria, P.; Bury, W.; Hupp, J. T.; Farha, O. K., *Chem. Commun.* **2014,** *50*, 1965.

143. Cravillon, J.; Munzer, S.; Lohmeier, S.-J.; Feldhoff, A.; Huber, K.; Wiebcke, M., *Chem. Mater.* **2009,** *21*, 1410.

144. Zhang, C.; Gee, J. A.; Sholl, D. S.; Lively, R. P., *J. Phys. Chem. C* **2014,** *118*, 20727.

145. Jayachandrababu, K. C.; Verploegh, R. J.; Leisen, J.; Nieuwendaal, R. C.; Sholl, D. S.; Nair, S., *J. Am. Chem. Soc.* **2016,** *138*, 7325.

146. Song, Y.; Hu, D.; Liu, F.; Chen, S.; Wang, L., *Analyst* **2015,** *140*, 623.

147. Liu, C.; Yan, B., *Photochem. Photobiol. Sci.* **2015,** *14*, 1644.

148. Tang, J.; Salunkhe, R. R.; Liu, J.; Torad, N. L.; Imura, M.; Furukawa, S.; Yamauchi, Y., *J. Am. Chem. Soc.* **2015,** *137*.

149. Tran, U. P. N.; Le, K. K. A.; Phan, N. T. S., *ACS Catal.* **2011,** *1*.

150. Lu, G.; Hupp, J. T., *J. Am. Chem. Soc.* **2010,** *132*.

151. Sun, C.-Y.; Qin, C.; Wang, X.-L.; Yang, G.-S.; Shao, K.-Z.; Lan, Y.-Q.; Su, Z.-M.; Huang, P.; Wang, C.-G.; Wang, E.-B., *Dalton Trans.* **2012,** *41*.

152. Zhuang, J.; Kuo, C.-H.; Chou, L.-Y.; Liu, D.-Y.; Weerapana, E.; Tsung, C.-K., *ACS Nano* **2014,** *8*.

153. Jiang, J.-Q.; Yang, C.-X.; Yan, X.-P., *ACS Applied Materials & Interfaces* **2013,** *5*.

154. Yang, X.-Q.; Yang, C.-X.; Yan, X.-P., *Journal of Chromatography A* **2013,** *1304*.

155. Pang, S. H.; Han, C.; Sholl, D. S.; Jones, C. W.; Lively, R. P., *Chem. Mater.* **2016,** *28*.

156. Tan, Y.-X.; He, Y.-P.; Zhang, J., *Inorg. Chem.* **2012,** *51*.

157. Jiao, Y.; Morelock, C. R.; Burtch, N. C.; Mounfield, W. P.; Hungerford, J. T.; Walton, K. S., *Ind. Eng. Chem. Res.* **2015,** *54*.

158. Han, S.; Huang, Y.; Watanabe, T.; Nair, S.; Walton, K. S.; Sholl, D. S.; Carson Meredith, J., *Microporous Mesoporous Mater.* **2013,** *173*.

159. Barbosa, P.; Rosero-Navarro, N. C.; Shi, F.-N.; Figueiredo, F. M. L., *Electrochim. Acta* **2015,** *153*.

160. Cheng, P.; Hu, Y. H., *J. Phys. Chem. C* **2014,** *118*.

161. Hu, Y.; Kazemian, H.; Rohani, S.; Huang, Y.; Song, Y., *Chem. Commun.* **2011,** *47*.

162. Miller, F. A.; Wilkins, C. H., *Analytical Chemistry* **1952,** *24*.

163. Siriwardane, R. V.; Woodruff, S., *Ind. Eng. Chem. Res.* **1995,** *34*.

164. Siriwardane, R. V.; Woodruff, S., *Ind. Eng. Chem. Res.* **1997,** *36*.

165. J.K.Saha, J. P., *Journal of Bangladesh Academy of Sciences,* **2011,** *35*.

166. Sivanesan, G.; Kolandaivel, P.; Pandian, S. S., *Mater. Chem. Phys.* **1993,** *34*.

167. N. Tugrul, A. S. K., E. Moroydor Derun, S. Piskin, *International Journal of Chemical, Molecular, Nuclear, Materials and Metallurgical Engineering* **2014,** *8*.

168. Rajamanickam, N.; Rajashabala, S.; Ramachandran, K., *J. Lumin.* **2014,** *146*.

169. Kwon, H. T.; Jeong, H.-K.; Lee, A. S.; An, H. S.; Lee, J. S., *J. Am. Chem. Soc.* **2015,** *137*.

170. Lee, M. J.; Kwon, H. T.; Jeong, H.-K., *J. Membr. Sci.* **2017,** *529*.